Synthetic High Density Lipoprotein Nanodiscs for Cancer Immunotherapy and Chemoimmunotherapy

by

Rui Kuai

A dissertation submitted in partial fulfillment
of the requirements for the degree of
Doctor of Philosophy
(Pharmaceutical Sciences)
in the University of Michigan
2018

Doctoral Committee:

Assistant Professor James J. Moon, Co-Chair
Assistant Professor Anna Schwendeman, Co-Chair
Professor Maria Castro
Professor Steven P. Schwendeman
Professor Duxin Sun

Rui Kuai

ruikuai@umich.edu

ORCID iD 0000-0003-2324-1272

DEDICATION

To my parents Shiquan Kuai, Xianqiong Yi, parents-in-law Dewen Yuan, Xueming Zheng

To my wife Wenmin Yuan

ACKNOWLEDGEMENTS

Graduate study is a long journey. Fortunately, I am not alone. I met many nice and friendly people along this journey and they provided me with generous help, without which I can not finish this long, but wonderful journey.

First and foremost, I would like to thank my two great advisors Dr. James Moon and Dr. Anna Schwendeman. I am very lucky to be one of their first students and have the chance to learn from two knowledgeable professors at the same time. Their rigorous approach to addressing scientific questions and zest for translational research has been inspiring me throughout my graduate study and will continue to have a profound impact on my future career. I am also grateful for their strong support and help along this journey, and the opportunities/freedom they provided in the lab to work on different projects. I really appreciate their systematic training on writing scientific papers, research proposals, and delivering good oral presentations. In addition to the help and support on my research, they also gave me a lot of useful suggestions for my career in the future, and I really appreciate the useful suggestions.

I also have great gratitude for other committee members: Dr. Steve Schwendeman, Dr. Duxin Sun, and Dr. Maria Castro. I am really grateful for their comments and suggestions, which helped me better understand and improve my research. My dissertation would have been impossible without their valuable feedback.

I want to thank lab members from Dr. James Moon's lab and Dr. Anna Schwendeman's lab. Lukasz Ochyl helped with the tetramer staining for animal studies. He was always glad to discuss scientific questions and gave me a lot of valuable input for my research. Yao Xu generously helped with the large scale cell culture, establishment of orthotopic tumor models, and ELISPOT, which dramatically improved the efficiency of my research. Yuchen Fan helped with the measurement of immunogenic cell death markers. Xiaoqi Sun helped with the in vivo immunization study. I would like to thank our lab manager Rose Ackermann for discussion and her generous help on HPLC. I want to thank another lab manager Karl Olsen for good maintainence of equipment needed for lab research. I also want to thank many other lab members… I am sorry that I can not list all the names here, but please know that I am really grateful for being able to work with you in the same lab and I really benefit from the work you have done to the lab and myself.

I would like to thank Robert H. Lyons (DNA sequencing core), Luis Villa Diaz, Jin Koo Kim, and Paul H. Krebsbach for their contributions on cDNA sequencing. I also want to thank Joel Whitfield (Immunology core) for his help on ELISPOT.

I would like to thank Chitra Subramanian and Peter White for their contribution on the nanodisc-based chemotherapy. It's been a great pleasure to work with them on some collaborative projects and diversify my research background.

I want to give my special thanks for my wife Wenmin Yuan. Thank you for giving me great support for my graduate study. Thank you for your hard great work on preparing nanodisc

samples, charactering them with LC-MS, and contributing to the in vitro and in vivo study for the chemoimmunotherapy part.

I want to thank my family. To my parents and parents-in-law, thank you for your help on taking care of my two kids and your unconditional support for my graduate study. To my wife Wenmin Yuan, I must thank you for the second time here, for your love, encouragement, and hard work for the family.

Finally, I would like to thank various financial supports from the College of Pharmacy, the American Heart Association Pre-doctoral Fellowship, Broomfield International Student Fellowship, and Norman Weiner Graduate Fellowship that help me finish my Ph.D. study.

Table of Contents

List of Figures

List of Tables

List of Abbreviations

Ag	Antigen
Ab	Antibody
APC	Antigen-presenting cell
BMDC	Bone marrow derived dendritic cells
CRT	Calreticulin
CTL	Cytotoxic T lymphocyte
DAMP	Damage-associated molecular pattern
DC	Dendritic cell
DOX	Doxorubicin
ELISA	Enzyme-linked immunosorbent assay
ELISPOT	Enzyme-Linked ImmunoSpot
FBS	Fetal bovine serum
GM-CSF	Granulocyte-macrophage colony -stimulating factor
GPC	Gel permeation chromatography
HDL	High density lipoprotein
HMGB1	High mobility group box 1
HPLC	High performance liquid chromatography
ICB	Immune checkpoint blocker
ICS	Intracellular cytokine staining
LNs	Lymph nodes
LPS	Lipopolysaccharide
MHC	Major histocompatibility complex
PAMP	Pathogen-associated molecular pattern
PBMC	Peripheral blood mononuclear cell

PRR	Pattern recognition receptor
sHDL	Synthetic high density lipoprotein
TAAs	Tumor associated antigens
TCR	T cell receptor
TEM	Transmission electron microscopy
TLR	Toll-like receptor
TME	Tumor microenvironment

Abstract

Despite the tremendous potential of peptide-based cancer vaccines, their efficacy has been limited in humans. Recent innovations in tumor exome sequencing have signaled the new era of personalized immunotherapy with patient-specific neo-antigens, but a general methodology for stimulating strong CD8α+ cytotoxic T-lymphocyte (CTL) responses remains lacking. Here we demonstrate that synthetic high density lipoprotein-mimicking nanodiscs (sHDL) coupled with antigen (Ag) peptides and adjuvants can markedly improve Ag/adjuvant co-delivery to lymphoid organs and sustain Ag presentation on dendritic cells. Strikingly, nanodiscs elicited up to 47-fold greater frequencies of neoantigen-specific CTLs than soluble vaccines and even 31-fold greater than perhaps the strongest adjuvant in clinical trials (i.e. CpG in Montanide). Moreover, multi-epitope vaccination generated broad-spectrum T-cell responses that potently inhibited tumor growth. Nanodiscs eliminated established MC-38 and B16F10 tumors when combined with anti-PD-1 and anti-CTLA-4 therapy. These findings represent a new powerful approach for cancer immunotherapy and suggest a general strategy for personalized nanomedicine. We also sought to develop alternative approaches for cancer therapy. For example, we demonstrated that by simply incorporating a hydrophobic anticancer drug withalongolide A-4,19,27-triacetate (WGA-TA) in sHDL nanodiscs, we could enhance the therapeutic outcome of WGA-TA and reduce the side effects due to the improved tumor targeted delivery of nanodiscs. In addition to direct killing of tumor cells, some chemotherapeutic drugs can cause immunogenic cell death and induce antitumor T cell responses, which also contribute to the anticancer efficacy and prompt a number

of clinical trials on combination chemoimmunotherapy. However, it remains unclear how to achieve potent immune activation with traditional chemotherapeutics in a manner that is safe, effective, and compatible with immunotherapy. Here we show that high-density lipoprotein (HDL)-mimicking nanodiscs loaded with doxorubicin (DOX), a widely used chemotherapeutic agent, can potentiate immune checkpoint blockade in murine tumor models. Delivery of DOX via nanodiscs triggered immunogenic cell death of cancer cells and exerted antitumor efficacy without any overt off-target side effects. Importantly, "priming" tumors with DOX-carrying nanodiscs elicited robust antitumor CD8+ T cell responses while broadening their epitope recognition to tumor-associated antigens, neoantigens, as well as intact whole tumor cells. Combination chemoimmunotherapy with nanodiscs plus anti-PD-1 therapy induced complete regression of established CT26 and MC38 colon carcinoma tumors in 80-88% of animals and protected survivors against tumor recurrence. Our work provides a new, generalizable framework for utilizing nanoparticle based chemotherapy to initiate antitumor immunity and sensitize tumors to immune checkpoint blockade.

Chapter 1 Introduction

1.1 Overview of antitumor immune responses

1.1.1 Innate and adaptive antitumor immunity

Many different immune cell populations are involved in the antitumor immunity. Innate immune cells such as NK cells, NKT cells, and neutrophils have been reported to kill tumor cells in an antigen-independent manner.[1] In contrast, adaptive immune cells such as T cells and B cells can kill tumor cells in an antigen-specific manner. Among these cells, it's well accepted that T cells are the major effector cells that determine the therapeutic outcome.[2] There are two major types of T cells, CD8+ cytotoxic T lymphocytes (CTL) and CD4+ T lymphocytes. Many studies have confirmed CD8+ T lymphocytes can lead to the specific lysis of tumor cells and higher levels of circulating or tumor-infiltrating CD8+ T lymphocytes are correlated with better prognosis. Recently, the importance of CD4+ T lymphocytes for cancer immunotherapy has also been revealed, as depletion of CD4+ T lymphocytes can compromise or even abrogate the therapeutic efficacy of certain cancer vaccines. [3]

1.1.2 Activation of antigen-specific T cells

The initial activation of naïve CD8+ or CD4+ T cells is mainly mediated by dendritic cells **(Figure 1.1**), which present the antigen peptides (epitopes) in the context of MHC class I or MHC class II on the surface of dendritic cells for activation of CD8+ and CD4+ T cells, respectively.[2] Dendritic cells (DCs) are the most important antigen presenting cells (APCs) for T

cell activation. Exogenous extracellular antigens can be taken up by DCs and processed in acidified endocytic vesicles, where the generated short peptides can bind to MHC class II molecules, and the complex of peptide-MHC class II molecules can be recognized by CD4+ T cells. Some endocytosed exogenous antigens can be directed into the MHC class I pathway for recognition by CD8+ T cells. This phenomenon is called cross-presentation, which can lead to the activation of antigen-specific CD8+ T cells. Cross-presentation is very important for the tumor immunotherapy.[4] Development of immunotherapy that can achieve higher cross-presentation will induce more cytotoxic T cell response and lead to better anti-tumor efficacy. Even though the mechanism is still poorly understood,[4] the following two possible mechanisms for cross-presentation have been proposed. Cytosolic pathway: Endocytosed exogenous antigens can escape from the endosome and be released into the cytosol, where they are degraded by the proteasome to generate short peptides. Some of these peptides can bind to MHC class I molecules and be cross-presented to the cell surface for recognition by CD8+ T cells. Vacuolar pathway: Endocytosed exogenous antigens are localized in acidified endocytic vesicles containing active cathepsin S, which can degrade the antigen into small peptide fragments. These peptide fragments can bind to MHC class I molecules in the endosome, which probably originated from the phagosome-ER fusion, and the peptide-MHC class I molecules are transported to the cell surface for recognition by CD8+ T cells.

In addition to the above antigen-MHC class I/II complexes on the surface of DCs, two other signals, including co-stimulatory molecules and cytokines are required for efficient priming of naïve T cells. For immunotherapy, the co-stimulatory molecules and cytokines are usually resulted from the adjuvants, which upon uptake by DCs, can upregulate co-stimulatory molecules including CD40 and CD80/CD86 for interaction with CD40L and CD28 on T cell

surface, respectively. Adjuvants can also induce DCs to secrete cytokines such as IL-12, which can provide the third signal required for activation and differenciation of T cells.[5]

1.2 Tumor antigens

1.2.2 Tumor associated antigens

Tumor associated antigens (TAAs) are overexpressed by tumor cells, but these antigens are also expressed by normal cells, although at much lower levels.[6] Previous cancer vaccines in preclinical and clinical studies mainly use TAAs for cancer immunotherapy. There are two major challegnes for the use of TAAs in cancer immunotherapy. The first challenge is that TAAs are self-antigens, and the immune system is normally tolerant to self-antigens and therefore it's difficult to induce strong T cell responses against these antigens.[7] However, sometimes, the immune tolerance can be broken with the use of strong adjuvant or efficient vaccine delivery systems and TAA-specific T cell responses can be induced. The second challenge is that TAAs are not only expressed by tumor cells but present in normal cells, so TAA-specific T cells can kill both tumor cells and normal cells. The toxicity is dependent on the strength of the T cell responses and the expression level of these antigens by normal cells.

1.2.1 Tumor neoantigens

When normal cells become cancerous, they have many nonsynonymous mutations, leading to the expression of mutant proteins that are not expressed by normal cells. These mutated protein sequences can be processed into short peptides (epitopes) and some of them can be presented in the context of major histocompatibility complex (MHC). These MHC/epitope complexes can be recognized by T cells, which can lead to the specific lysis of tumor cells.[8] Because these tumor neoantigens are "changed-self antigens" (similar to foreign antigens), the immune system is

normally not tolerant to these antigens. Importantly, because neoantigens are missing in normal cells, neoantigen-specific T cells can selectively kill tumor cells without harming normal cells, thereby providing a safe and effective method for cancer immunotherapy. Other exogenous antigens such as viral epitopes expressed in cancer cells can be considered as neoantigens as well.[8]

1.3 Adjuvants

In addition to antigens, adjuvants are commonly included in the vaccine to help induce adaptive immune responses.[9] Based on their origin, adjuvants can be classified into damage-associated molecular patterns (DAMPs) and pathogen-associated molecular patterns (PAMPs).[10] These adjuvants can act on pattern recognition receptors (PRRs) and lead to the upregulation of costimulatory signals and secretion of cytokines required for activation of T cells. Different types of adjuvants have been extensively reviewed elsewhere and several commonly used adjuvants relevant to the dissertation are summarized below.

1.3.1 TLR agonists

TLRs such as TLR1-2, TLR3, TLR4, TLR7, and TLR9 are widely expressed in innate immune cells including dendritic cells. TLRs recognize PAMPs present in a variety of pathogens and initiate inflammatory responses.[11] In the context of cancer immunotherapy, TLR agonists are used in the vaccine to induce upregulation of costimulatory signals and secretion of cytokines needed for T cell activation. Some TLR agonists can induce secretion of type I interferon, which have been reported to contribute to the anti-tumor immunity. [12]

In addition to PAMPs, DAMPs can also activate TLRs and lead to the activation of T cells. For example, tumor cells treated with certain chemo drugs can undergo immunogenic cell death and

secrete High mobility group box 1 protein (HMGB1), which is a TLR4 agonist and can help elicitation of antitumor T cell responses.[13]

1.3.2 STING ligands

Stimulator of interferon gene (STING) is an adaptor molecule capable of activating the TBK1-IRF3 axis to induce type I interferon production and eliciting antigen-specific CTL responses in the presence of antigens. Several STING agonists themselves haven been shown to exert antitumor efficacy.[14,15] For example, cyclic dinucleoties such as cyclic guanosine monophosphate (cGAMP), and cyclic diguanylate and cyclic diadenylate are known to activate the STING pathway and enhance the antitumor immune responses. Recently, more and more synthetic STING agonists with different chemical structures have been developed, and their ability to induce type I interferon and boost the antitumor immunity has been well confirmed.

1.3.3 Montanide

Montanide-based adjuvants can form water-in-oil emulsion after simple mixing and homogenization in aqueous phase. They are prepared by using the surfactants from the mannide monooleate family. After injection, they can form depot at the injection site, allowing for gradual release of antigens and induction of prolonged immune responses. Montanides have been used in peptide vaccines for the treatment of melanoma and Non-Small Cell Lung Cancer (NSCLC) in clinical trials.[16-18]

1.4 Cancer vaccine delivery

1.4.1 Soluble vaccine

Cancer vaccines are typically composed of antigens and adjuvants. Most cancer vaccines are administered through subcutaneous or intramuscular injection so that they can drain to local

lymph nodes, where high concentrations of resident dendritic cells are available to take up antigens and adjuvants for activation of T cells. The simplest version of cancer vaccine is the physical mixture of tumor antigen peptides and adjuvants in the soluble form.[19] However, antigen peptides have very low molecular weights and can be quickly absorbed into systemic circulation upon subcutaneous injection, with a small amount of antigen peptides delivered in the lymph nodes and dendritic cells. In addition, certain antigen peptides can potentially bind to non-dendritic cells directly, leading to T cell anergy or apoptosis of T cells.[19] As a result, the overall T cell responses induced by soluble vaccines are very weak.

1.4.2 Water-in-oil emulsions

Another form of cancer vaccine that has been widely used in preclinical and clinical studies are Water-in-oil emulsions.[20] For example, antigen peptides in aqueous phase are mixed with montanide. The mixture is then homogenized to form water-in-oil emulsion. After injection, they can form depot at the injection site, allowing for gradual release of antigens and induction of prolonged immune responses.[20] Recent studies showed depot formation and persistent antigen induced by Montanide at the injection site can impair antigen-specific T cell responses through induction of IFN-γ-mediated and Fas ligand-dependent apoptosis. [20]

1.4.3 Nanoparticle-based vaccine delivery

The rapid development of nanotechnology has provided powerful tools for cancer vaccine delivery.[21] Unlike soluble antigen peptides that have limited lymph nodes draining, various nanoparticles have shown increased lymph nodes draining after subcutaneous injection. For example, relatively large nanoparticles can be taken up by dendritic cells underneath the skin, which then migrate to the lymph nodes, while small nanoparticles can directly drain to the lymph nodes. The latter pathway is preferred because the concentration of resident dendritic cells in the

lymph nodes is much higher than that underneath the skin and the vaccines have more chance to interact with dendritic cells for T cell activation. In addition, nanoparticles also enable the codelivery of both antigens and adjuvants to the same dendritic cells, which is required for elicitation of strong T cell responses.

1.5 High density lipoprotein - HDL

1.5.1 Endogenous HDL

The discovery of high-density lipoprotein (HDL) is dated back to 1929 when a protein-rich, lipid-poor complex was isolated from equine serum at Institute Pasteur by Macheboeuf.[22] Later in the 1950s, Eder and colleagues isolated HDL from human serum as a chemical entity by ultracentrifugation,[23] but it was not until the 1960s that the biological roles of serum lipoproteins and their impact on the cardiovascular system were suggested.[24] Today, it is well known that HDL plays critical roles in the transport and metabolism of lipids, such as cholesterol and triglycerides.[25] Other lipoproteins involved in lipid metabolism include low-density lipoprotein (LDL), very low-density lipoprotein (VLDL), and chylomicrons. Endogenous HDL is heterogeneous—possessing varying compositions and characteristics depending on its maturation stage.[26] Based on electrophoretic migration behaviors, HDL can be generally classified into three subtypes; α-migrating species, which include spherical HDL2 and HDL3; β-migrating species, which include pre-β discoidal HDL, lipid-poor ApoA1, and free ApoA1; and γ-migrating species.[27]

1.5.2 Biosynthesis of endogenous HDL

The biosynthesis of endogenous HDL begins with the production of ApoA1 in the liver or intestine.[28] Nascent, discoidal HDL is then formed through lipidation of ApoA1, which is achieved through the efflux of free phospholipid and cholesterol mediated by the ATP-binding

cassette transporter A1 (ABCA1) receptor. Nascent HDL is cholesterol poor, but some cholesterol can still be found interspersed among the phospholipid molecules. Lecithin cholesterol acyltransferase (LCAT) can convert free cholesterol into cholesterol ester (CE), which can then be internalized into the core of the HDL particle, initiating its transformation from discoidal to spherical HDL. The esterification of free cholesterol is thought to form a cholesterol gradient that enables more cholesterol to bind onto the HDL surface in the subsequent steps of reverse cholesterol transport.[29] Spherical HDL can further internalize cholesterol effluxed by ATP-binding cassette transporter G1 (ABCG1) and scavenger receptor type B-I (SR-BI) to become more mature, larger spherical HDL. Mature HDL can also exchange cholesterol ester for triglycerides from LDL—a process that is mediated by cholesteryl ester transfer protein (CETP). Mature HDL, which is typically composed of a hydrophobic core with cholesterol ester and triglycerides and a hydrophilic surface containing lipids and ApoA1,[29] delivers its cargo molecules to hepatocytes where they are metabolized through an SR-BI-mediated process.[22]

HDL removes excess cholesterol from lipid-laden macrophages, called "foam cells," in atherosclerotic lesions *via* a process known as reverse cholesterol transport (RCT). HDL also possesses anti-inflammatory and anti-oxidative properties.[30] These functions allow HDL to exert a protective effect on the cardiovascular system, and therefore, HDL is known as "good cholesterol". Moreover, endogenous HDL is reported to transport signaling lipids, proteins, and endogenous microRNAs to recipient cells, suggesting that HDL plays multi-faceted roles in complex intercellular communication.[31] These features have inspired numerous academic laboratories and pharmaceutical industries to develop HDL as delivery vehicles for various therapeutic agents. However, isolation and purification of endogenous HDL from human plasma

under current good manufacturing practice (cGMP) is costly and laborious. Additionally, there are safety concerns and manufacturing challenges associated with reformulating endogenous HDL into drug-loaded therapeutics. To address these issues, various recombinant ApoA proteins and ApoA mimetic peptides have been developed within the past few years for *ex vivo* reconstitution of HDL. These synthetic HDL systems, recapitulating the *in vivo* properties of endogenous HDL, can be produced at a large scale, thus highlighting their great potential to facilitate clinical development of HDL-based therapeutics. Importantly, safety of HDL-based on ApoA proteins and ApoA mimetic peptides has also been well documented in several clinical trials at relatively high doses.[32,33]

1.6 Synthesis of HDL in vitro

In order to synthesize HDL in vitro, full-length Apo A1 purified from plasma,[34] Apo A1 produced recombinantly,[35] or Apo A1 mimetic short peptides (18-22 amino acids) have been used.[36,37] Compared to endogenous or recombinant full-length Apo A1, short peptides have special advantages in that they are not only cheaper but also easier to scale up and control the quality. Listed below are several different methods for the preparation of HDL in vitro.

1.6.1 Direct Isolation from Plasma

HDL can be isolated from plasma by ultracentrifugation.[38] Briefly, a one-half volume of solution with a density of approximately 1 g/mL is mixed with one volume of serum and centrifuged for 2-3 hours at 340,000 x g at 16 °C. One volume of the lower solution is mixed with a one-half volume of a solution with a density of ~1.2 g/mL and centrifuged for 3-4 h at the same speed and temperature. Then one volume of the lower solution is mixed with a one-half volume of a solution with a density of ~1.5 g/mL and centrifuged again for 7-8 hours at 266,000 x g at 16 °C. The HDL fraction is located in the upper solution after the third centrifugation. Fast protein

liquid chromatography (FPLC) has also been used to isolate HDL from the plasma.[39] Although these methods allow for the preparation of relatively pure HDL, they are very costly, time consuming, and therefore, suboptimal for the large-scale production of HDL.

1.6.2 Sodium Cholate Dialysis Method

In addition to the direct isolation of an HDL fraction from plasma, HDL can be reconstituted *in vitro* using lipids together with either ApoA1 proteins, ApoE proteins, or their mimetic peptides. Briefly, lipid mixture (typically composed of phospholipid, cholesterol, and cholesteryl oleate) is dried under nitrogen flow to a thin film. Lipids are hydrated in buffer using sodium cholate, and appropriate amount of Apo-A1 or mimetic peptide is added. The mixture is incubated for 12 hours at 4 ℃, followed by dialysis against PBS for 2 days with three buffer changes to remove sodium cholate. A previous report has shown that less than 2% of the sodium cholate remains in the final synthetic HDL formulation based on the ^{3}H cholate analysis.[40] Reconstituted HDL has the size, shape, and targeting properties similar to endogenous HDL. Cholate dialysis method has been used to prepare clinical supplies for CSL-111 and CSL-112.[41]

1.6.3 Sonication Method

Lipid mixture (typically composed of phospholipid and cholesteryl oleate) in chloroform is dried under nitrogen flow and then placed in a vacuum oven for 1 h. PBS buffer is added to the film and the mixture is vortexed for 5 min, followed by sonication for 60 min at 48 ^{0}C under nitrogen. ApoA1 or the mimetic peptide in PBS buffer is added to the mixture, which becomes transparent immediately. The resulting heterogeneous HDL needs to be filtered by 0.2 □m membrane and then purified by gel filtration chromatography to obtain homogeneous HDL.[37] Reconstituted HDL also has the size, shape, and targeting properties similar to endogenous HDL.

1.6.4 Single Step Reconstitution of HDL Using Microfluidics

Even though the sodium cholate dialysis method and sonication method allow for reconstitution of HDL possessing properties similar to endogenous HDL isolated from plasma, the preparation process is lengthy and difficult to scale up. To address these issues, microfluidics has been recently used for the preparation of HDL.[42] Briefly, phospholipids dissolved in organic solution were injected into an inlet channel of a microfluidic device with a programmable syringe pump. ApoA1, dissolved in aqueous solution, was injected in the outer channels. The microfluidic device allows for rapid and effective mixing of the solution by generating tunable dual microvortices and a focusing pattern at Reynolds number (Re) ~150. Self-assembly of HDL was initiated with the transition of lipids from an organic solution to an aqueous solution, permitting incorporation of ApoA1 to the nascent lipid aggregates and formation of small HDL nanoparticles. HDL prepared using this method has the similar properties as endogenous HDL.[42]

1.6.5 Thermal Cycling Method

Large-scale production of HDL under cGMP condition is crucial for translation of HDL to clinical trials. Dasseux *et al.* reported a thermal cycling-based method which can be easily used to produce HDL under cGMP conditions.[43] Briefly, lipids were weighed and added to the buffer and then dispersed at 50 ^{0}C using a high-performance disperser. The lipid suspension was then combined with ApoA1 protein or ApoA1 mimetic peptide solution and heated to 57 ^{0}C under nitrogen, followed by cooling to room temperature to form homogeneous HDL. HDL nanoparticles prepared with this method have also been shown to exhibit properties similar to endogenous HDL.[44] In addition, the thermal cycling method does not require costly preparation processes or organic solvent, and therefore can be easily adapted for large-scale production of HDL.

1.7 HDL as delivery carriers

HDL itself has many important functions such as protective role (also known as good cholesterol) on cardiovascular system, anti-inflammation and anti-oxidation etc. In addition, HDL is inherently biocompatible, and the receptors for HDL are very well known. These features make HDL suitable to be used as delivery vehicles. By using HDL as delivery vehicles, many problems such as low drug solubility, severe side effects, and low efficacy can be overcome to some extent. Although endogenous HDL is mainly designed to transport lipophilic cargoes such as lipids in vivo, it is not limited to the delivery of these molecules. Hydrophilic molecules such as peptides, proteins, siRNA and oligodeoxynucleotide (ODN) have been successfully delivered by HDL using different strategies.

1.7.1 Delivery of small molecules

Both nascent discoidal and mature spherical HDL have a hydrophobic core, which is an ideal site for the loading of lipophilic small molecules. The encapsulation of lipophilic drugs into the hydrophobic core can greatly increase the solubility, decrease the side effects and increase the efficacy of the drug. For example, amphotericin B is a lipophilic antifungal drug with dose-limiting side effects, which include nephrotoxicity and hematologic abnormalities. When the drug was formulated into HDL, it exhibited less toxicity to the red blood cells and good efficacy in preventing a fungal infection in a mouse model.[45] Similarly, all-trans retinoic acid (ATRA) is a lipophilic drug used for the treatment of acute promyelocytic leukemia, but its use is limited by the low solubility and severe side effects such as neurotoxicity and cytokine storm-mediated toxic syndrome. After the drug was formulated into HDL, it exhibited better efficacy in a mantle cell lymphoma model compared to the conventional formulation.[46]

Other examples include the encapsulation of curcumin,[47,48] paclitaxel,[49] 10-HCPT and doxorubicin into HDL,[50,51]and in all cases the HDL formulation greatly reduced the IC50 of these anticancer drugs, improved the circulation time and decreased the side effects.

1.7.2 Delivery of peptides/proteins

Many proteins/peptides have good biological activities and are very promising to be used for the treatment of different diseases, but proteins/peptides tend to undergo proteolysis, denaturation and aggregation, limiting their efficacy in vivo, therefore appropriate delivery systems are needed to both protect and increase the efficacy of the peptides/proteins.[52] HDL is a nanocarrier with many good properties and can potentially solve these problems, but it's hard to encapsulate peptides/proteins into HDL if they are not highly lipophilic. However, efforts have been made to achieve the incorporation of hydrophilic proteins/peptides into HDL, and the incorporation greatly improved the efficacy of these proteins/peptides.

In order to load peptide/protein antigens hemagglutinin 5 (H5) and Yersinia pestis LcrV onto HDL, Nicholas O. Fischer etc. prepared some Nickel-lipid modified HDL containing recombinant apolipoprotein using sodium cholate dialysis method.[35 53 54]After peptides/proteins were modified with polyhistidine, they could be easily conjugated to the Nickel-lipids. They also loaded either MPLA or CpG into the same HDL nanoparticle, and the antibody titer achieved by the antigen-conjugated HDL/MPLA or antigen-conjugated HDL/CpG was much higher than free antigen, but the cellular response was not tested in their study.

Cytolytic peptide melittin is a promising candidate to overcome tumor drug resistance due to its cytolytic property. However, the severe side effect, hemolysis, limited its wide use.[55] Chuan Huang etc. fused the N-terminus of melittin to the C-terminus of an Apo A1 mimetic peptide via a GSG linker.[56] The fusion enabled melittin to interact with phospholipids and self-assemble into

HDL nanoparticles with diameter about 20nm. The interaction between melittin and phospholipids could mask the positive charge of melittin, reducing the side effect of hemolysis and increasing the safe dosage range. Melittin could be released inside the B16F10 tumor cells after it was taken up and exert the cytotoxic effect. When the fusion peptide-HDL was used for the treatment of B16F10 tumor-bearing mice, it led to the much better tumor growth inhibition compared to the PBS group and blank HDL group.

1.7.3 Delivery of nucleic acids

RNAi (RNA interference) is a promising gene therapy in that it has better specificity and has potential to down-regulate any protein involved in the formation and metastasis of tumor, even for those undruggable target proteins.[57] Actually, there have been some clinical trials using RNAi to fight against cancer recently.[58] However, siRNA has unfavorable PK, low cellular uptake and low biological stability, which prevent its wide application on cancer treatment. A delivery system that can protect siRNA, target the tumor region and achieve efficient intracellular delivery in tumor cells is greatly needed for the successful RNAi application. HDL is a delivery system that can meet the above requirements and several methods have been developed for the incorporation of hydrophilic siRNA into HDL. Such strategies can also be used for the incorporation of single stranded DNA (ODN) or double stranded DNA into HDL.

In order to incorporate bcl-2 siRNA into HDL composed of lipids and Apo A1 mimetic peptide, Mi Yang et al. modified the bcl-2 siRNA with cholesterol (chol-si-bcl-2).[59] [60]After the chol-si-bcl-2 was incubated with the pre-formed HDL at room temperature for 30 min, it was successfully inserted into the lipid layers of HDL. The chol-si-bcl-2-HDL had sizes about 25.3 ± 1.2 nm and was stable in 10% fetal bovine serum (FBS) or 10% human plasma at 4 or 37 ° C for 3 h. When FITC-chol-si-bcl-2-HDL was incubated with SRBI high-expressing KB cells, more

than 90% of the total intracellular FITC-chol-si-bcl-2 signal was in the cytosol. Western blot showed chol-si-bcl-2-HDL at a dose of 400 nM could reduce the Bcl-2 expression to 35 ± 9% of the untreated control, while equivalent dose of chol-si-bcl-2 alone could only reduce the Bcl-2 expression to 84 ± 8% of the untreated control. In addition, chol-si-bcl-2-HDL was also more efficient in inducing the apoptosis of the tumor cells compared to the free chol-si-bcl-2.

Other examples include the systemic delivery of cholesterol conjugated siRNA (Chol-siOAT3) into brain capillary endothelial cells (BCECs) using HDL. The OAT3 mRNA levels in BCECs were significantly reduced when Chol-siOAT3 in HDL was intravenously injected.[61]

Instead of modifying the siRNA with cholesterol, Mian M.K. Shahzad etc. used polylysine to complex with siRNA to neutralize the negative charges of phosphate groups in siRNA and successfully encapsulated the siRNA-polylysine complex into HDL composed of lipids and Apo A1 with encapsulation efficiency over 90%.[62] TEM showed after incorporation of siRNA-loaded HDL had a diameter of 10 nm. STAT3 siRNA/HDL could result in over 80% knockdown of STAT3 in vitro. After a single intravenous injection of STAT3 siRNA/HDL into a SKOV3 tumor-bearing model, STAT3 protein levels were reduced by 88%. The injection of STAT3 siRNA/HDL alone could result in some therapeutic effect on several different tumor models, but better therapeutic effects were observed when chemotherapeutic drugs were co-administered.

1.8 Conclusions

Overall, it remains to be seen how the exciting progress made in the field of HDL-based therapy can evolve to reprogram HDL as a platform technology for cancer immunotherapy and chemoimmunotherapy. Clinical translation of HDL-based therapeutics may offer innovative solutions to treat and diagnose various human pathologies. [63]

1.9 Figures

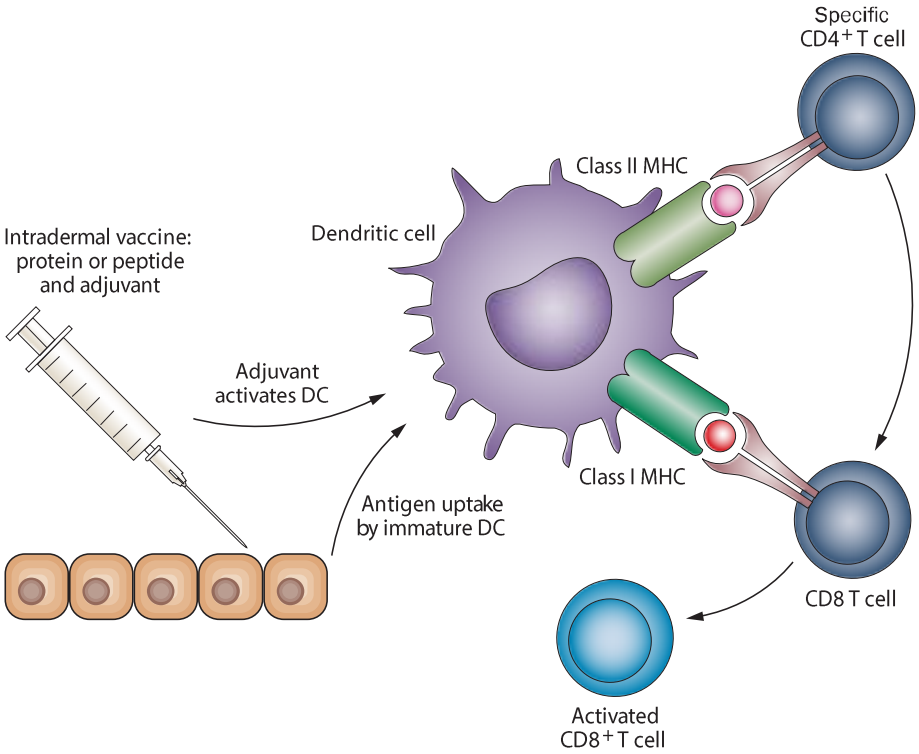

Figure 1.1 Schematic of T cell activation by cancer vaccines. Adapted from Nat Rev Clin Oncol. 2014;11(1):24-37.

1.10 References

1. Corrales L, Matson V, Flood B, Spranger S, Gajewski TF. Innate immune signaling and regulation in cancer immunotherapy. *Cell Res.* Jan 2017;27(1):96-108.

2. Drake CG, Lipson EJ, Brahmer JR. Breathing new life into immunotherapy: review of melanoma, lung and kidney cancer. *Nat Rev Clin Oncol.* Jan 2014;11(1):24-37.

3. Kreiter S, Vormehr M, van de Roemer N, et al. Mutant MHC class II epitopes drive therapeutic immune responses to cancer (vol 520, pg 692, 2015). *Nature.* Jul 16 2015;523(7560).

4. Joffre OP, Segura E, Savina A, Amigorena S. Cross-presentation by dendritic cells. *Nat Rev Immunol.* Aug 2012;12(8):557-569.

5. Kalinski P, Hilkens CMU, Wierenga EA, Kapsenberg ML. T-cell priming by type-1 and type-2 polarized dendritic cells: the concept of a third signal. *Immunol Today.* Dec 1999;20(12):561-567.

6. Ward JP, Gubin MM, Schreiber RD. The role of neoantigens in naturally occurring and therapeutically induced immune responses to cancer. *Adv Immunol.* 2016;130:25-74.

7. Coulie PG, Van den Eynde BJ, van der Bruggen P, Boon T. Tumour antigens recognized by T lymphocytes: at the core of cancer immunotherapy. *Nat Rev Cancer.* Feb 2014;14(2):135-146.

8. Yarchoan M, Johnson BA, Lutz ER, Laheru DA, Jaffee EM. Targeting neoantigens to augment antitumour immunity. *Nat Rev Cancer.* Apr 2017;17(4):209-222.

9. Reed SG, Orr MT, Fox CB. Key roles of adjuvants in modern vaccines. *Nat Med.* Dec 2013;19(12):1597-1608.

10. Temizoz B, Kuroda E, Ishii KJ. Vaccine adjuvants as potential cancer immunotherapeutics. *Int Immunol.* Jul 2016;28(7):329-338.

11. Kawai T, Akira S. The role of pattern-recognition receptors in innate immunity: update on Toll-like receptors. *Nat Immunol.* May 2010;11(5):373-384.

12. Klinman DM. Immunotherapeutic uses of CpG oligodeoxynucleotides. *Nat Rev Immunol.* Apr 2004;4(4):248-257.

13. Krysko DV, Garg AD, Kaczmarek A, Krysko O, Agostinis P, Vandenabeele P. Immunogenic cell death and DAMPs in cancer therapy. *Nat Rev Cancer.* Dec 2012;12(12):860-875.

14. Ishikawa H, Barber GN. STING is an endoplasmic reticulum adaptor that facilitates innate immune signalling (vol 455, pg 674, 2008). *Nature.* Nov 13 2008;456(7219):274-274.

15. Li XD, Wu JX, Gao DX, Wang H, Sun LJ, Chen ZJJ. Pivotal Roles of cGAS-cGAMP Signaling in Antiviral Defense and Immune Adjuvant Effects. *Science.* Sep 20 2013;341(6152):1390-1394.

16. Guy B. The perfect mix: recent progress in adjuvant research. *Nat Rev Microbiol.* Jul 2007;5(7):505-517.

17. Neninger Vinageras E, de la Torre A, Osorio Rodriguez M, et al. Phase II randomized controlled trial of an epidermal growth factor vaccine in advanced non-small-cell lung cancer. *J Clin Oncol.* Mar 20 2008;26(9):1452-1458.

18. Chianese-Bullock KA, Pressley J, Garbee C, et al. MAGE-A1-, MAGE-A10-, and gp100-derived peptides are immunogenic when combined with granulocyte-macrophage colony-stimulating factor and montanide ISA-51 adjuvant and administered as part of a multipeptide vaccine for melanoma. *J Immunol.* Mar 01 2005;174(5):3080-3086.

19. Melief CJM, van der Burg SH. Immunotherapy of established (pre) malignant disease by synthetic long peptide vaccines. *Nat Rev Cancer.* May 2008;8(5):351-360.

20. Hailemichael Y, Dai ZM, Jaffarzad N, et al. Persistent antigen at vaccination sites induces tumor-specific CD8(+) T cell sequestration, dysfunction and deletion. *Nat Med.* Apr 2013;19(4):465-472.

21. Smith DM, Simon JK, Baker JR. Applications of nanotechnology for immunology (vol 13, pg 592, 2013). *Nat Rev Immunol.* Sep 2013;13(9).

22. Kingwell BA, Chapman MJ, Kontush A, Miller NE. HDL-Targeted Therapies: Progress, Failures and Future. *Nat Rev Drug Discov.* Jun 2014;13(6):445-464.

23. Barr DP, Russ EM, Eder HA. Protein-Lipid Relationships in Human Plasma. II. In Atherosclerosis and Related Conditions. *Am J Med.* Oct 1951;11(4):480-493.

24. Gofman JW. Serum Lipoproteins and The Evaluation of Atherosclerosis. *Ann N Y Acad Sci.* Nov 16 1956;64(4):590-595.

25. Wang M, Briggs MR. HDL: The Metabolism, Function, and Therapeutic Importance. *Chem Rev.* Jan 2004;104(1):119-137.

26. Movva R, Rader DJ. Laboratory Assessment of HDL Heterogeneity and Function. *Clin Chem.* May 2008;54(5):788-800.

27. Damiano MG, Mutharasan RK, Tripathy S, McMahon KM, Thaxton CS. Templated High Density Lipoprotein Nanoparticles as Potential Therapies and for Molecular Delivery. *Adv Drug Del Rev.* May 2013;65(5):649-662.

28. Nofer JR, Kehrel B, Fobker M, Levkau B, Assmann G, von Eckardstein A. HDL and Arteriosclerosis: Beyond Reverse Cholesterol Transport. *Atherosclerosis.* Mar 2002;161(1):1-16.

29. Vance DEVaJE. *Biochemistry of Lipids, Lipoproteins and Membranes (Fifth Edition).* 2008.

30. Kontush A, Chapman MJ. Antiatherogenic Function of HDL Particle Subpopulations: Focus on Antioxidative Activities. *Curr Opin Lipidol.* Aug 2010;21(4):312-318.

31. Vickers KC, Palmisano BT, Shoucri BM, Shamburek RD, Remaley AT. MicroRNAs are Transported in Plasma and Delivered to Recipient Cells by High-Density Lipoproteins. *Nat Cell Biol.* Apr 2011;13(4):423-433.

32. Khan ML, N. D.; Drake, S. L.; Crockatt, J. G.; Dasseux, J. L. H. Single-Dose Intravenous Infusion of ETC-642, a 22-mer ApoA-I Analogue and Phospholipids Complex, Elevates HDL-C in Atherosclerosis Patients. *Circulation.* 2003;108:563-564.

33. Navab M, Anantharamaiah GM, Reddy ST, et al. Human Apolipoprotein A-I and A-I Mimetic Peptides: Potential for Atherosclerosis Reversal. *Curr Opin Lipidol.* Dec 2004;15(6):645-649.

34. Zhang WL, He HL, Liu JP, et al. Pharmacokinetics and atherosclerotic lesions targeting effects of tanshinone IIA discoidal and spherical biomimetic high density lipoproteins. *Biomaterials.* Jan 2013;34(1):306-319.

35. Fischer NO, Rasley A, Corzett M, Hwang MH, Hoeprich PD, Blanchette CD. Colocalized Delivery of Adjuvant and Antigen Using Nanolipoprotein Particles Enhances the Immune Response to Recombinant Antigens. *J Am Chem Soc.* Feb 2013;135(6):2044-2047.

36. Zhang ZH, Cao WG, Jin HL, et al. Biomimetic Nanocarrier for Direct Cytosolic Drug Delivery. *Angew Chem Int Ed.* 2009;48(48):9171-9175.

37. Zhang ZH, Chen J, Ding LL, et al. HDL-Mimicking Peptide-Lipid Nanoparticles with Improved Tumor Targeting. *Small.* Feb 2010;6(3):430-437.

38. Hatch FT. Practical Methods for Plasma Lipoprotein Analysis. *Adv Lipid Res.* 1968;6:1-68.

39. van den Elzen P, Garg S, Leon L, et al. Apolipoprotein-Mediated Pathways of Lipid Antigen Presentation. *Nature.* Oct 6 2005;437(7060):906-910.

40. McConathy WJ, Nair MP, Paranjape S, Mooberry L, Lacko AG. Evaluation of Synthetic/Reconstituted High-Density Lipoproteins as Delivery Vehicles for Paclitaxel. *Anticancer Drugs.* Feb 2008;19(2):183-188.

41. Lerch PG, Fortsch V, Hodler G, Bolli R. Production and Characterization of a Reconstituted High Density Lipoprotein for Therapeutic Applications. *Vox Sang.* 1996;71(3):155-164.

42. Kim Y, Fay F, Cormode DP, et al. Single Step Reconstitution of Multifunctional High-Density Lipoprotein-Derived Nanomaterials Using Microfluidics. *ACS Nano.* Nov 2013;7(11):9975-9983.

43. Dasseux J-LO, D. C.; Ackermann, R, Inventor. Lipoprotein Complexes and Manufacturing and Uses Thereof. US patent US 20120232005 A12012.

44. Schwendeman A, Sviridov DO, Yuan WM, et al. The Effect of Phospholipid Composition of Reconstituted HDL on Its Cholesterol Efflux and Anti-Inflammatory Properties. *J Lipid Res.* Sep 2015;56(9):1727-1737.

45. Oda MN, Hargreaves PL, Beckstead JA, Redmond KA, van Antwerpen R, Ryan RO. Reconstituted high density lipoprotein enriched with the polyene antibiotic amphotericin B. *J Lipid Res.* Feb 2006;47(2):260-267.

46. Singh ATK, Evens AM, Anderson RJ, et al. All trans retinoic acid nanodisks enhance retinoic acid receptor mediated apoptosis and cell cycle arrest in mantle cell lymphoma. *Br J Haematol.*. Jul 2010;150(2):158-169.

47. Ghosh M, Singh ATK, Xu WW, Sulchek T, Gordon LI, Ryan RO. Curcumin nanodisks: formulation and characterization. *Nanomedicine.* Apr 2011;7(2):162-167.

48. Singh ATK, Ghosh M, Forte TM, Ryan RO, Gordon LI. Curcumin nanodisk-induced apoptosis in mantle cell lymphoma. *Leuk Lymphoma.* Aug 2011;52(8):1537-1543.

49. Mooberry LK, Nair M, Paranjape S, McConathy WJ, Lacko AG. Receptor mediated uptake of paclitaxel from a synthetic high density lipoprotein nanocarrier. *J Drug Target* . Jan 2010;18(1):53-58.

50. Zhang XB, Chen BS. Recombinant high density lipoprotein reconstituted with apolipoprotein AI cysteine mutants as delivery vehicles for 10-hydroxycamptothecin. *Cancer Lett.* Dec 2010;298(1):26-33.

51. Yuan Y, Wang WN, Wang BL, Zhu HY, Zhang BH, Feng MQ. Delivery of hydrophilic drug doxorubicin hydrochloride-targeted liver using apoAI as carrier. *J Drug Target.* May 2013;21(4):367-374.

52. Manning MC, Chou DK, Murphy BM, Payne RW, Katayama DS. Stability of Protein Pharmaceuticals: An Update. *Pharm Res.* Apr 2010;27(4):544-575.

53. Fischer NO, Blanchette CD, Chromy BA, et al. Immobilization of His-Tagged Proteins on Nickel-Chelating Nanolipoprotein Particles. *Bioconjugate Chem.* Mar 2009;20(3):460-465.

54. Blanchette CD, Fischer NO, Corzett M, Bench G, Hoeprich PD. Kinetic Analysis of His-Tagged Protein Binding to Nickel-Chelating Nanolipoprotein Particles. *Bioconjugate Chem.* Jul 2010;21(7):1321-1330.

55. Papo N, Shai Y. Host defense peptides as new weapons in cancer treatment. *Cell Mol Life Sci.* Apr 2005;62(7-8):784-790.

56. Huang C, Jin HL, Qian Y, et al. Hybrid Melittin Cytolytic Peptide-Driven Ultrasmall Lipid Nanoparticles Block Melanoma Growth in Vivo. *ACS Nano.* Jul 2013;7(7):5791-5800.

57. Gomes-da-Silva LC, Fonseca NA, Moura V, de Lima MCP, Simoes S, Moreira JN. Lipid-Based Nanoparticles for siRNA Delivery in Cancer Therapy: Paradigms and Challenges. *Acc Chem Res.* Jul 2012;45(7):1163-1171.

58. Tabernero J, Shapiro GI, LoRusso PM, et al. First-in-Humans Trial of an RNA Interference Therapeutic Targeting VEGF and KSP in Cancer Patients with Liver Involvement. *Cancer Discov.* Apr 2013;3(4):406-417.

59. Yang M, Jin HL, Chen JA, et al. Efficient Cytosolic Delivery of siRNA Using HDL-Mimicking Nanoparticles. *Small.* Mar 2011;7(5):568-573.

60. Nakayama T, Butler JS, Sehgal A, et al. Harnessing a Physiologic Mechanism for siRNA Delivery With Mimetic Lipoprotein Particles. *Mol Ther.*. Aug 2012;20(8):1582-1589.

61. Kuwahara H, Nishina K, Yoshida K, et al. Efficient In Vivo Delivery of siRNA Into Brain Capillary Endothelial Cells Along With Endogenous Lipoprotein. *Mol Ther.* Dec 2011;19(12):2213-2221.

62. Shahzad MMK, Mangala LS, Han HD, et al. Targeted Delivery of Small Interfering RNA Using Reconstituted High-Density Lipoprotein Nanoparticles. *Neoplasia.* Apr 2011;13(4):309-U142.

63. Kuai R, Li D, Chen YE, Moon JJ, Schwendeman A. High-Density Lipoproteins: Nature's Multifunctional Nanoparticles. *ACS nano.* Mar 22 2016;10(3):3015-3041.

Chapter 2 Designer Vaccine Nanodiscs for Personalized Cancer Immunotherapy

2.1 Abstract

Despite the tremendous potential of peptide-based cancer vaccines, their efficacy has been limited in humans. Recent innovations in tumor exome sequencing have signaled the new era of personalized immunotherapy with patient-specific neo-antigens, but a general methodology for stimulating strong CD8α+ cytotoxic T-lymphocyte (CTL) responses remains lacking. Here we demonstrate that high density lipoprotein-mimicking nanodiscs coupled with antigen (Ag) peptides and adjuvants can markedly improve Ag/adjuvant co-delivery to lymphoid organs and sustain Ag presentation on dendritic cells. Strikingly, nanodiscs elicited up to 47-fold greater frequencies of neoantigen-specific CTLs than soluble vaccines and even 31-fold greater than perhaps the strongest adjuvant in clinical trials (i.e. CpG in Montanide). Moreover, multi-epitope vaccination generated broad-spectrum T-cell responses that potently inhibited tumor growth. Nanodiscs eliminated established MC-38 and B16F10 tumors when combined with anti-PD-1 and anti-CTLA-4 therapy. Such vaccine nanodiscs also showed potent therapeutic efficacy for the treatment of various mucosal tumors, including lung tumors, oral tumors and intravaginal tumors. These findings represent a new powerful approach for cancer immunotherapy and suggest a general strategy for personalized nanomedicine.

2.2 Introduction

Peptide-based cancer vaccines have been extensively investigated due to their good safety profiles and ease of manufacturing and quality control. However, their anti-tumor efficacy in

clinical trials has been disappointing, a phenomenon that has been attributed to inefficient co-delivery of Ag peptides and adjuvants to draining lymph nodes (dLNs), and subsequent immunological tolerance and CTL fratricide[1]. Although depot-forming water-in-oil adjuvant systems can improve immunogenicity[2,3], booster immunizations can cause T-cell sequestration at the vaccine site, leading to T-cell exhaustion and deletion[4]. To address these issues, various nano-vaccine systems have been evaluated in animal models with varying degrees of success[5-15]. Despite the progress in the field, potential safety concerns and scale-up manufacturing of nanoparticles, especially in a manner suitable for personalized therapeutics with patient-specific neo-antigens, still remain as the major challenges.

Here we propose an alternative, simple strategy where preformed nanocarriers, with an established clinical manufacturing procedure and excellent safety profiles in humans, are mixed with adjuvants and Ag peptides, including tumor-specific mutant neo-epitopes[16-19], to produce personalized cancer vaccines (**Figure 2.1**). Our strategy is based on synthetic high density lipoprotein (sHDL) nanodiscs, composed of phospholipids and apolipoprotein A1 (ApoA1)-mimetic peptides. Compared with other HDLs containing 243-amino acid ApoA1 purified from human plasma or produced recombinantly[20-22], sHDL nanodiscs are synthesized with 22-mer peptides (22A), derived from the repeat α-helix domain of ApoA1[23], with no sequence homology to endogenous ApoA1, thus averting potential trigger of autoimmunity. Importantly, sHDL has been previously manufactured for clinical testing and proven to be safe in humans with the maximum tolerated dose at ~2.2 g/m^2,[24-26] a value one- to two-orders of magnitude greater than most polymeric or inorganic nanoparticles in clinical trials[27,28].

Here we set out to develop a nanodisc-based platform for neo-antigen vaccination (**Figure 2.1**). Exploiting the endogenous role of HDL as a nanocarrier for cholesterol, we modified a commonly used oligonucleotide containing 5'-C-phosphate-G-3' (CpG) motif, a potent Toll-like receptor-9 agonist, with cholesterol (Cho-CpG) to enhance its *in vivo* trafficking. We show that preformed sHDL nanodiscs can be simply mixed with cholesteryl-CpG and tumor Ag peptides, including neo-antigens identified via tumor DNA sequencing, to produce homogeneous, stable, and ultrasmall nanodiscs in less than two hours at room temperature (RT). The nanodiscs promote co-delivery of Ag/CpG to dLNs; prolong Ag presentation on antigen-presenting cells (APCs); elicit striking levels of broad-spectrum antitumor T-cell responses that significantly inhibit tumor growth; and eradicate established tumors when combined with immune checkpoint blockade. Based on the facile production process, robust therapeutic efficacy, and clinical safety demonstrated previously[24,25], our approach offers an attractive platform technology for patient-tailored cancer vaccines as well as other bioactive therapeutics.

2.3 Materials and Methods

2.3.1 Materials

1,2-dimyristoyl-*sn*-glycero-3-phosphocholine (DMPC), 1,2-dioleoyl-*sn*-glycero-3-phosphoethanolamine (DOPE), and rhodamine (Rhod)-labeled DOPE (DOPE-Rhod) were purchased from Avanti Polar Lipids (Alabaster, AL). ApoA1 mimetic peptide (22A), $OVA_{257-264}$ SIINFEKL, CSSSIINFEKL, CSSSIINFEK(FITC)L, $TRP2_{180-188}$ SVYDFFVWL, CSVYDFFVWL, M27 neo-epitope LCPGNKYEM, M30 neo-epitope CSSVDWENVSPELNSTDQ, and *Adpgk* mutant peptide ASMTNMELM were synthesized by GenScript Corp. (Piscataway, NJ). CSSASMTNMELM was synthesized by AnaSpec (Fremont, CA). The oligodeoxynucleotide TLR9 ligand CpG 1826 (5'-tccatgacgttcctgacgtt-3', lower case

letters represent phosphorothioate backbone), CpG 1826 modified with cholesterol at the 3' end (Cho-CpG), and Cy5 modified Cho-CpG were synthesized by Integrated DNA Technologies (Coralville, IA). HPLC grade methanol and acetonitrile were purchased from Fisher Scientific (Pittsburgh, PA). Fetal bovine serum (FBS), penicillin-streptomycin, β-mercaptoethanol and ACK lysis buffer were purchased from Life Technologies (Grand Island, NY). Granulocyte macrophage colony stimulating factor (GM-CSF) was from GenScript Corp. (Piscataway, NJ). Anti-mouse CD16/32, CD86-PE, CD40-APC, CD62L-PECy7, and 25-D1.16 mAb-PE against SIINFEKL/H-2K^b were from eBioscience (San Diego, CA). Anti-mouse CD8α-APC, CD44-FITC, TNF-α-FITC, IFN-γ-PE, and CD11c-PECy7 were from BD Bioscience (San Jose, CA). Anti-mouse PD-1-PECy7, PD-L1-PECy7, and isotype control antibodies were from Biolegend (San Diego, CA). Tetramer H-2K^b-SIINFEKL-PE was purchased from Beckman Coulter (Brea, CA). Tetramer/H-2D^b-ASMTNMELM-PE was kindly provided by the NIH Tetramer Core Facility (Atlanta, GA). Anti-mouse PD-1 (RMP1-14) and anti-mouse CTLA-4 (9D9) antibodies were purchased from BioXcell (West Lebanon, NH). We obtained B3Z CD8α+ T cell hybridoma from Dr. N. Shastri (University of California, Berkeley); B16OVA from Dr. Kenneth Rock (University of Massachusetts, Amherst, MA); MC-38 cells from Dr. Weiping Zou (University of Michigan, Ann Arbor, MI); and B16F10 (CRL-6475) cells from the American Type Culture Collection (ATCC).

2.3.2 Synthesis of DOPE-PDP

Dioleoyl-*sn*-glycero-3-phosphoethanolamine-N-[3-(2-pyridyldithio) propionate] (DOPE-PDP) was synthesized as reported previously with slight modifications[29]. Briefly, DOPE, SPDP (succinimidyl 3-(2-pyridyldithio) propionate) and triethylamine (1:1:1.5 molar ratio) were dissolved in chloroform. The mixture was reacted in the dark for 5 h. The reaction progress was

monitored by thin layer chromatography (TLC), using the following mixture as the developing solvent: chloroform/methanol/water = 65/25/4 (volume ratio). After TLC indicated disappearance of the starting materials and appearance of a faster-running spot, the reaction mixture was dried by rotary evaporation and purified on a silica gel column.

2.3.3 Preparation and characterization of vaccine nanodiscs

DMPC and DOPE-PDP (molar ratio = 96:4) were dissolved in chloroform. The mixture was dried with nitrogen flow and placed under vacuum for at least 1 h. The resulting lipid film was hydrated in 10 mM sodium phosphate buffer (0.3117 g/L $NaH_2PO_4.H_2O$ and 2.0747g/L $Na_2HPO_4.7H_2O$, pH 7.4) and sonicated in a bath sonicator for 10 min, followed by probe sonication for another 2.5 min. ApoA1 mimetic peptide 22A dissolved in endotoxin free water was added to the above mixture (22A:lipids = 1:7.5 molar ratio), which was then subjected to heating (50 ^{o}C) for 3 min and cooling (ice water) for 3 min, with 3 cycles in total, to obtain sHDL.

To conjugate tumor antigen peptides to sHDL, cysteine terminated tumor antigen peptides dissolved in endotoxin free water were added to the above sHDL (antigen peptide:DOPE-PDP = 2.5:1, molar ratio) and incubated at room temperature with gentle shaking on an orbital shaker. To construct sHDL nanodiscs with multi-antigens, each antigen peptide was reacted with DOPE-PDP (antigen peptide:DOPE-PDP = 1.5:1, molar ratio) for 1 h in dimethylformamide (DMF), which was removed by freeze-drying after dilution with endotoxin-free water. The lipid-peptide conjugates were added to pre-formed sHDL and incubated for 30 min at room temperature. Unreacted tumor antigen peptides were removed by using Zeba Spin Desalting columns (Pierce) following the manufacturer's instructions. The conjugation efficiency of tumor antigen peptides was calculated based on the decrease of absorbance signal associated with DOPE-PDP as

determined by HPLC. Briefly, 200 µl sHDL formulations were freeze-dried and reconstituted in 300 µl methanol. The mixture was filtered by a 0.22 µm PTFE filter and analyzed with a Shimadzu HPLC system using a Vydac 219TP Diphenyl column (4.6 mm × 250 mm ID). The two solvents used for the HPLC analysis consisted of water:trifluoroacetic acid =100:0.5 (mobile phase A) and methanol:acetonitrile:trifluoroacetic acid = 50:50:0.05 (mobile phase B) (0-75 min, 15-100%). The flow rate was 0.4 mL/min and the detection wavelength was 220 nm. The loading efficiency of tumor antigen peptides in sHDL was confirmed by using FITC-labeled peptides and measuring the fluorescence intensity of sHDL formulations at Ex = 490 nm and Em = 520 nm after dissolving the formulations in PBS containing 1% Triton X-100.

To load CpG in sHDL, different concentrations (0-200 µg/mL) of cholesterol modified CpG (Cho-CpG) were incubated with sHDL at room temperature with gentle shaking on an orbital shaker. The amount of CpG incorporated into sHDL and free CpG was analyzed by gel permeation chromatography (GPC). Briefly, the sHDL formulations were diluted in PBS to a concentration of 0.5 mg/mL 22A peptide. The formulations were filtered through a 0.22 □m filter and analyzed with a Shimadzu HPLC system equipped with a TSKgel G2000SWxl column (7.8 mm ID × 30 cm, Tosoh Bioscience LLC). The flow rate of mobile phase PBS (pH 7.4) was set at 0.7 mL/min, and the detection wavelength was set at 260 nm for CpG.

The sHDL formulations were diluted to 0.5 mg/mL 22A with PBS, and the particle sizes were measured by dynamic light scattering (DLS, Zetasizer Nano ZSP, Malvern, UK). The morphology of sHDL was observed by transmission electron microscopy (TEM) after proper dilution of the original samples. Briefly, 3 µL of the sample solution was deposited on a carbon film-coated 400 mesh copper grid (Electron Microscopy Sciences) and dried for 1 minute. The samples were then negatively-stained with 5 droplets of 1% uranyl acetate solution, excessive

solutions on the grid were blotted, and the grid was dried before TEM observation. All images were acquired on JEM 1200EX electron microscope (JEOL USA, Peabody, MA) equipped with an AMT XR-60 digital camera (Advanced Microscopy Techniques Corp. Woburn, MA).

2.3.4 Activation of BMDCs

BMDCs were prepared as described previously[30]. Briefly, femur and tibia were harvested aseptically from C57BL/6 mice, and the bone marrow was flushed into a petri dish using a 5 mL syringe (26 G needle) loaded with BMDC culture media (RPMI 1640 supplemented with 10% FBS, 100 U/mL penicillin, 100 μg/ml streptomycin, 50 μM β-mercaptoethanol, and 20 ng/ml GM-CSF). Cells were collected by passing the cell suspension through a cell strainer (mesh size = 40 μm), followed by centrifugation. Cells were seeded into non-tissue culture treated petri-dish at a density of 2×10^5 cells/ml, cultured at 37 ^{o}C with 5% CO_2. Culture media were refreshed on days 3, 6, 8, and 10, and BMDCs were used for the following assays on days 8-12.

Immature BMDCs were plated at 1×10^6 cells/well in 12-well plates. After 24 h, BMDCs were washed once with PBS and incubated with 75 nM of CpG in different formulations or 0.5 μg/mL LPS (positive control) for 24 h at 37 ^{o}C with 5% CO_2. BMDCs were harvested, washed with FACS buffer (1% BSA in PBS), incubated with anti-CD16/32 at room temperature for at least 10 min, and then stained with fluorophore-labeled antibodies against CD11c, CD40, CD80, and CD86 at room temperature for 30 min. Finally, cells were washed twice by FACS buffer, resuspended in 2 μg/ml DAPI solution, and analyzed by flow cytometry (Cyan 5, Beckman Coulter, USA).

2.3.5 Antigen presentation on BMDCs

Immature BMDCs were plated at 1×10^6 cells/well in 12-well plates 24 h prior to use. BMDCs were washed with PBS and incubated with 75 nM CpG and/or 500 nM antigen peptide in various formulations in complete media for different lengths of time (2, 6, 24, and 48 h). BMDCs were then harvested, washed with FACS buffer, incubated with anti-CD16/32 at room temperature for at least 10 min, and stained with PE-conjugated anti-mouse SIINFEKL/H-$2K^b$ mAb 25-D1.16 at room temperature for 30 min. Cells were then washed, resuspended in 2 μg/ml DAPI solution, and analyzed by flow cytometry (Cyan 5, Beckman Coulter, USA).

Alternatively, BMDCs were plated at 5×10^4 cells/well in a U-bottom 96-well plate. After overnight culture, BMDCs were washed with PBS and incubated with different formulations of SIINFEKL (20, 100 and 500 nM) and CpG (3, 15, and 75 nM) for 24 h or 48 h at 37 ^{o}C. Cells were then carefully washed 3 times with PBS, and 10^5 B3Z CD8+ T hybridoma cells/well were added in RPMI 1640 supplemented with 10% FBS, 2 mM L-glutamine, 55 μM β-mercaptoethanol, 1 mM pyruvate and 100 U/mL penicillin and 100 μg/mL streptomycin. After 24 hr of incubation, cells were pelleted via centrifugation (1500 rcf, 7 min), the media were carefully aspirated, and 150 μL CPRG/lysis buffer (0.15 mM chlorophenol red- β-D-galactopyranoside (CPRG), 0.1% Triton-X 100, 9 mM MgCl2, 100 μM mercaptoethanol in PBS) was added. The plates were incubated at 37 ^{o}C in the dark for 90 min, after which the absorbance of released chlorophenol red was measured at 570 nm using a microplate reader.

2.3.6 Confocal microscopy

JAWSII cells (ATCC, Manassas, VA) were seeded at 1×10^6 cells on 35 mm petri dishes (MatTek Corp., Ashland, MA) that have been pre-equilibrated with the complete cell culture media and cultured overnight. To investigate the intracellular delivery profiles of antigen

peptides, JAWSII cells were incubated with the physical mixture of free CSSSIINFEK(FITC)L and CpG, or sHDL-CSSSIINFEK(FITC)L/CpG for different lengths of time (6, 24, and 48 h). Cells were then washed 3 times with PBS and incubated for 30 min at 37 ^{o}C with 50 nM LysoTracker® Red DND-99 (Invitrogen) and 2 μg/mL Hoechst in phenol/serum-free media to stain lysosomes and nuclei, respectively. In parallel, to study the intracellular delivery profiles of structural components of sHDL, the lipid layers of sHDL were incorporated with DOPE-Rhod by adding 0.5 mol % DOPE-Rhod in the initial lipid film, while 22A peptide of sHDL was labeled by incubating pre-formed sHDL with Texas Red®-X succinimidyl ester (Life Technologies) and passing Texas Red-labeled sHDL through a desalting column to remove the unreacted dye. The resulting fluorophore-tagged sHDL formulations were incubated with JAWSII cells at 37 ^{o}C with 5% CO_2. After 24 h incubation, cells were washed 3 times with PBS and then incubated for 30 min at 37 ^{o}C with 500 nM LysoTracker® Green DND-26 (Invitrogen) and 2 μg/mL Hoechst in phenol/serum-free media to stain lysosomes and nuclei, respectively. JAWSII cells were then imaged using a confocal microscope (Nikon A1).

2.3.7 In vivo immunization studies

Animals were cared for following federal, state, and local guidelines. All work performed on animals was in accordance with and approved by University Committee on Use and Care of Animals (UCUCA) at University of Michigan, Ann Arbor. Female C57BL/6 mice of age 6–8 weeks (Harlan Laboratories) were immunized with different formulations containing antigen peptides (15.5 nmol/mouse) and CpG (2.3 nmol/mouse) in 100 μl volume by subcutaneous injection at the tail base on indicated time points. In some studies, antigen peptide and CpG emulsified in Montanide served as a positive control[2,3,31]. Briefly, antigen peptide (155 nmol)

and CpG (23 nmol) in 0.5 mL PBS were thoroughly emulsified in 0.5 mL Montanide until the mixture was homogeneous and administered subcutaneously in 100 µl injection volume.

For lymph node draining studies, C57BL/6 mice were injected with free CSSSIINFEK(FITC)L, sHDL-CSSSIINFEK(FITC)L, free Cho-CpG(Cy5), or sHDL-Cho-CpG(Cy5). After 24 h, inguinal lymph nodes were harvested, and FITC or Cy5 fluorescence signal was measured with IVIS optical imaging system (Caliper Life Sciences).

For prophylactic tumor challenge studies, vaccinated animals were challenged on day 8 after last immunization by subcutaneous injection of 2×10^5 B16OVA cells/mouse on the right flank. Tumor growth was monitored every other day, and the tumor volume throughout this study was calculated by the following equation[32]: tumor volume = length × width^2 × 0.52. Animals were euthanized when the tumor masses reached 1.5 cm in diameter or when animals became moribund with severe weight loss or ulceration. For the lung metastasis model, vaccinated animals were challenged two months after the third vaccination by intravenous injection of 5×10^4 B16OVA cells/mouse. The animals were euthanized after 20 days, and the lungs were put in Fekete's solution before B16OVA tumor nodules were counted.

For therapeutic tumor vaccination studies with MC-38 cells, C57BL/6 mice were inoculated with 1×10^5 MC38 cells per mouse on the right flank by subcutaneous injection on day 0 and vaccinated on days 10, 17, and 24 with 15.5 nmol of ASMTNMELM and 2.3 nmol of CpG in either sHDL or free soluble form. For the combinatorial immunotherapy against MC-38 tumor, mice were inoculated subcutaneously with 1×10^5 MC38 cells on day 0 and vaccinated on days 10, and 17 with 15.5 nmol of ASMTNMELM and 2.3 nmol of CpG in either sHDL or free soluble form. Anti-mouse PD-1 (100 µg/mouse) was administered intraperitoneally on days 1

and 4 after each vaccination. For B16F10 studies, mice were inoculated subcutaneously with 1×10^5 B16F10 cells on day 0 and vaccinated on days 4, 11, and 18 with indicated formulations (10 nmol of each antigen peptide and 2.3 nmol of CpG). For the combinatorial immunotherapy against B16F10 tumor, anti-mouse PD-1 and anti-mouse CTLA-4 (each 100 μg/mouse) antibodies were administered intraperitoneally on days 1 and 4 after each vaccination. Tumor growth was monitored as indicated above.

2.3.8 Tetramer staining assay

Immunized mice were analyzed for the percentages of tumor antigen-specific CD8α+ T cells among peripheral blood mononuclear cells (PBMCs) using the tetramer staining assay, as described previously[33]. In brief, 100 μl of blood was drawn from each mouse on indicated time points by submandibular bleeding, and red blood cells were lysed with ACK lysis buffer. PBMCs were then washed with FACS buffer and blocked by anti-CD16/32 antibody and incubated with peptide-MHC tetramer tagged with PE (e.g. H-2K^b-restricted SIINFEKL, or H-2D^b-restricted ASMTNMELM) for 30 min at room temperature. Samples were then incubated with anti-CD8α-APC for 20 min on ice. Cells were washed twice with FACS buffer and resuspended in 2 μg/ml DAPI solution for analysis by flow cytometry (Cyan 5, Beckman Coulter, USA).

2.3.9 ELISPOT

For ELISPOT assay, spleens from immunized mice were harvested aseptically, processed into single cell suspensions for each mouse, and seeded at 3×10^5 splenocytes per well in 96-well PVDF plates (EMD Millipore) pre-incubated overnight with IFN-γ coating Ab (R&D Systems). Splenocytes were co-incubated with antigen peptides (2.5 μg/ml) or controls for 24 hours. Assays were completed using sequential incubations with biotinylated-secondary Ab,

streptavidin-alkaline phosphatase (Sigma Chemical), and NBT/BCIP substrate (Surmodics). Developed spots were enumerated using an AID iSpot Reader (Autoimmun Diagnostika GmbH, Germany).

2.3.10 Intracellular cytokine staining

For intracellular cytokine staining (ICS) assay, 100-150 µL peripheral blood collected from vaccinated mice was lysed with ACK lysis buffer, washed with PBS, and plated at ~10 million cells/mL in 50 µL T cell media (RPMI 1640 supplemented with 10% FBS, 2 mM L-glutamine, 55 µM β-mercaptoethanol, 1 mM pyruvate and 100 U/mL penicillin and 100 µg/mL streptomycin, HEPES, and non-essential amino acids) in 96-well U bottom plates. Cells were pulsed with 10 µg/mL antigen peptides or ApoA-I mimetic 22A peptide for 6 hours with protein transport inhibitor, brefeldin A (BD Biosciences), added during the last 4 h of incubation. For multivalent peptide vaccine studies, 50,000 BMDCs were added in each well to ensure antigen presentation. Cells were then washed twice with ice-cold FACS buffer (1% BSA in PBS), followed by incubation with anti-CD16/32 for at least 10 minutes and anti-CD8α for 20 min on ice. Cells were then fix/permeabilized for 20 min on ice and then stained with anti-IFN-γ-PE and anti-TNF-α-FITC for 30 min on ice. After extensive washing, cells were analyzed by flow cytometry.

2.3.11 Analysis of intratumoral T cells

For some experiments, tumor tissues were excised at indicated time points and cut into small pieces of 2-4 mm and then placed in dissociation buffer (1 mg/mL of collagenase type IV and 0.1 mg/mL of DNase I in RPMI) for 30 min at 37 ^{0}C with gentle shaking. The cell suspension was passed through a 70-µm strainer, washed with FACS buffer, stained with indicated antibodies, followed by flow cytometry analysis.

2.3.12 Measurement of antibody titers against 22A peptide

ELISA plates were coated with 22A peptide in PBS (1 μg/mL) with 100 μL/well and incubated overnight at 4 ^{0}C. Plates were blocked with 1% BSA in PBS for 2 h, and 100 μL of 4-fold serial dilutions of serum was added to each 96-well and incubated for 1 hour at room temperature. Wells were incubated with rabbit anti-mouse IgG-HRP (1:5000 dilution) for 1 h at room temperature, followed by addition of the HRP substrate, TMB. The enzymatic reaction was stopped by adding 2N H_2SO_4, and the absorbance at 450 nm (OD450) was measured using a microplate reader. The highest dilution with twice the absorbance of background was considered as the end-point dilution titer.

2.3.13 cDNA sequencing of neo-epitope (Adpgk) in MC-38 cells

Total RNA was extracted from MC-38 cells by the RNeasy® mini Kit (QIAGEN) following the manufacturer's instructions. The first-strand cDNA was synthesized using 1 μg of total RNA with the SuperScript™ III First-Strand Synthesis SuperMix Kit (Invitrogen). Adpgk cDNA with lengths of 250 bp and 485 bp were selectively amplified by using the following two sets of sequence specific primers. Primer 1: TGCCAACCGCTTCATCTTCT (forward primer) and GGTAGACCAGCGTGTGGAAA (reverse primer); Primer 2: CTCCAACGGGGCCATGAATA (forward primer) and CGTGGGAAAGACCTGCTGAT (reverse primer). The amplification was performed using the SuperScript One Step RT-PCR System (Invitrogen). The final cDNA products were visualized in 1.5% agarose gels with ethidium bromide, and the Adpgk cDNA bands were cut and purified using the PureLink® Quick Gel Extraction and PCR Purification Combo Kit (Invitrogen). The purified cDNA was sequenced by the Sanger sequencing method[34] at the University of Michigan DNA Sequencing Core.

2.3.14 Statistical analysis

Sample sizes were chosen based on preliminary data from pilot experiments and previously published results in the literature. All animal studies were performed after randomization. Data were analyzed by one- or two-way analysis of variance (ANOVA), followed by Tukey's multiple comparisons post-test or log rank (Mantel-Cox) test with Prism 6.0 (GraphPad Software). Data were normally distributed and variance between groups was similar. *P* values less than 0.05 were considered statistically significant. All values are reported as means ± SD with the indicated sample size. No samples were excluded from analysis.

2.4 Results and Discussion

2.4.1 Preparation and Characterization of vaccine nanodiscs

We first identified lipids and peptides conducive to nanodisc formation. DMPC lipid films were hydrated and added with a series of ApoA1-mimetic peptides, followed by thermal cycling between 50 ºC and 4 ºC. We identified a subset of peptides, including 22A and D-amino acids of 22A, that produced clear sHDL suspensions, stable for one month when stored at 4ºC (**Table 2.1**, **Figure 2.2**). In addition, use of phospholipids with transition temperature (Tm) below RT (e.g. POPC and DOPC with Tm = -2°C and -17°C, respectively) produced murky liposomal suspension, whereas lipids with high Tm (e.g. DPPC and DMPC with Tm = 41°C and 24°C, respectively) formed clear sHDL suspensions in the presence of 22A (**Figure 2.2**), showing flexibility in the materials design. Based on their size, homogeneity, and long-term stability, we chose to further investigate 22A and DMPC as the key components of nanodisc vaccines.

To achieve intracellular release of Ag within APCs via reduction-sensitive conjugation of Ag on sHDL, we synthesized dioleoyl-sn-glycero-3-phosphoethanolamine-N-[3-(2-pyridyldithio)

propionate] (**Figure 2.3**) and incorporated PDP into sHDL (4 mol%). When incubated for 30 min at RT with Ag peptides modified with a cysteine-serine-serine (CSS) linker[35], sHDL nanodiscs were efficiently surface-decorated with various Ag peptides (e.g., OVA257-264, a model CD8α+ T-cell epitope Ag from ovalbumin; and Adgpk, neo-antigen in MC-38), and subsequent incubation with Cho-CpG for 30 min at RT led to almost complete (~98%) insertion of CpG into sHDL, producing nanodiscs co-loaded with Ag and CpG (termed sHDL-Ag/CpG, with ~6.5 Ag peptides and ~1 CpG molecule per nanodisc, Supplementary (**Figure 2.4, Table 2.2**). sHDL-Ag/CpG exhibited uniform disc-like morphology with an average diameter of 10.5 ± 0.5 nm and polydispersity index of 0.20 ± 0.02 (**Figure 2.5a,b**). Importantly, sHDL-Ag/CpG could be readily sterile-filtered and stored frozen at -20 ºC for at least 8 weeks before thawing at 37 °C, without negatively affecting its homogeneity (**Figure 2.5c**).

2.4.2 BMDC activation and antigen presentation

We next examined the impact of nanodiscs on Ag presentation. Bone marrow derived dendritic cells (BMDCs) pulsed for 24 h with sHDL-CSSSIINFEKL/CpG presented $OVA_{257-264}$ SIINFEKL with a greater efficiency than BMDCs treated with free Ag peptides admixed with CpG or sHDL-CSSSIINFEKL, as determined by staining DCs with the 25-D1.16 mAb directed against SIINFEKL-H-$2K^b$ complexes. Interestingly, DCs pulsed with free SIINFEKL+CpG efficiently presented Ag for the first 6 h of incubation, but Ag presentation decreased precipitously past 6 h (**Figure 2.5d-f**), suggesting initial direct Ag binding to MHC-I molecules, followed by rapid Ag degradation or disassociation. In contrast, Ag presentation with sHDL-Ag/CpG gradually increased over time, achieving ~9-fold greater levels at 24 h and maintaining ~4-fold higher levels even at 48 h, compared with free SIINFEKL+CpG.

Intrigued by prolonged Ag presentation, we investigated the process of nanodisc uptake and Ag localization using CSS-SIINFEK$_{(FITC)}$L; SIINFEKL modified with FITC at ε-amino group in the lysine residue is known to retain its binding capacity to H-2K^b molecules[36]. JAWSII cells (immortalized immature DCs) incubated with free Ag(FITC)+CpG displayed weak fluorescence signal on the plasma membrane at 6 h, and only dim fluorescence was observed by 24 h (**Figure 2.5g, Figure 2.6**). In stark contrast, sHDL-Ag(FITC)/CpG treatment led to strong FITC signal co-localized with endosomes/lysosomes by 6 h, and robust Ag(FITC) signal was detected on cell membranes by 24 h and sustained up to 48 h. In addition, nanodiscs containing Rh-PE or Texas Red-labeled-22A were predominantly found within endosomes/lysosomes, indicating cellular uptake of intact whole nanodiscs (**Figure 2.7**). To assess the impact of prolonged Ag presentation on T-cell cross-priming, we treated BMDCs with free Ag peptides+CpG or sHDL-Ag/CpG for 24 or 48 h, and then added SIINFEKL-specific, H-2K^b-restricted B3Z T-cell hybridomas. BMDCs pulsed with sHDL-Ag/CpG promoted strong B3Z T-cell activation even after 48 h incubation, whereas free Ag peptides+CpG induced minimal B3Z T-cell activation beyond the 24 h period (**Figure 2.8**). Moreover, sHDL-Ag/CpG potently stimulated DC maturation (**Figure 2.9**). Altogether, whereas free Ag peptide was rapidly loaded and dissociated from MHC-I molecules on cell membranes, nanodiscs facilitated intracellular delivery of Ag/CpG and mediated their sustained release within endosomes/lysosomes, thereby promoting durable Ag presentation, APC maturation, and cross-priming CD8α+ T-cells *in vitro*.

2.4.3 Elicitation of strong T cell responses in vivo

We next investigated the impact of nanodiscs on lymphatic delivery of Ag/CpG and induction of CD8α+ T-cell responses *in vivo*[5]. C57BL/6 mice injected subcutaneously at tail base with 31 nmol free CSS-SIINFEK$_{(FITC)}$L had minimal FITC signal in inguinal dLNs after 1 day (**Figure**

2.10), potentially due to systemic dissemination of small MW Ag peptide or direct Ag binding on non-APCs at the injection site[1]. In contrast, sHDL-Ag group exhibited markedly increased FITC signal in dLNs ($p < 0.01$, **Figure 2.1**), with Ag(FITC) and Cy5-tagged 22A co-localized within dLNs. Similarly, injection of 2.3 nmol Cy5-tagged Cho-CpG in sHDL increased its LN accumulation, compared with injection in free soluble form ($p < 0.01$). These results showed that sHDL nanodisc promoted co-delivery of Ag and CpG to dLNs. We next immunized C57BL/6 mice with 15.5 nmol Ag and 2.3 nmol CpG (non-fluorophore tagged), and peripheral blood was analyzed for the frequency of SIINFEKL–MHC-I tetramer+ CD8α+ T-cells. The mixture of free Ag peptides (SIINFEKL or CSS-SIINFEKL) and CpG induced 1-3% Ag-specific CTLs after the third immunization (**Figure 2.11 a,b**). As the benchmark, we also vaccinated animals with the equivalent doses of Ag and CpG emulsified in water-in-oil Montanide, which is arguably one of the strongest adjuvant systems in clinical trials for peptide-based cancer vaccines[2,3,37,38]. Ag+CpG+Montanide elicited ~2% Ag-specific CTLs after priming; however, no further T-cell expansion was observed even after the third immunization, consistent with a recent study reporting dysfunction and deletion of high-avidity T-cells after repeated immunizations with a depot-forming water-in-oil adjuvant[4]. In contrast, sHDL-Ag/CpG group elicited a peak frequency of ~21% Ag-specific CD8α+ T-cells after the third vaccination ($p < 0.0001$, **Figure 2.11 a,b**). When challenged with 2×10^5 B16OVA cells, mice immunized with sHDL-Ag/CpG had no detectable tumor masses up to 28 days, whereas mice immunized with free Ag peptides+CpG or Ag+CpG+Montanide all succumbed to tumors with marginal survival benefits (**Figure 2.11c,d**). We observed similar levels of peak Ag-specific CTL responses after sHDL-Ag/CpG vaccination with the dosing intervals of 1, 2, or 3 weeks (**Figure 2.12**). Importantly, throughout our studies, we did not observe any signs of toxicity, autoimmunity, nor immune

responses directed against the ApoA1-mimetic peptide 22A in animals immunized multiple times with sHDL-Ag/CpG (**Figure 2.13**).

We sought to rule out the possibility that CSS-modified peptides or Cho-CpG dissociated from sHDL-Ag/CpG *in vivo* were responsible for the strong CTL responses. Introducing the CSS linker to SIINFEKL and replacing free CpG with Cho-CpG in free soluble form resulted in minimal T-cell responses, and the physical mixture of Ag, CpG, and sHDL also elicited weak CTL responses (**Figure 2.14a-c**). In contrast, sHDL-Ag/CpG nanodiscs drastically improved CD8α+ T-cell responses, eliciting remarkable 41-fold greater frequency of Ag-specific CD8α+ T-cells than CSSSINFEKL+Cho-CpG group (day 35, $p < 0.0001$), with CTLs primarily exhibiting $CD44^{high}CD62L^{low}$ effector phenotype and robust IFN-γ^+ ELISPOT responses (**Figure 2.14a-c**). We also examined the durability of T-cell responses; after achieving their peak ~30% responses, animals still maintained 10% Ag-specific CD8α+ T-cells at 2 months post the last vaccination (20-fold greater than free Ag+CpG group, $p < 0.001$, **Figure 2.15a**), and efficiently eliminated B16OVA cells inoculated intravenously (**Figure 2.15b**), demonstrating long-lived protection against tumor challenge. In contrast, the soluble vaccine failed to protect animals against the intravenous B16OVA challenge.

2.4.4 Elicitation of strong T cell responses in vivo

To demonstrate the utility of our platform technology for vaccination against neo-antigens, we first employed the murine MC-38 colon carcinoma model recently reported to harbor a single-epitope mutation within Adpgk protein (ASMTN**R**ELM → ASMTN**M**ELM), with the neo-epitope presented in MHC-I H-$2D^b$ molecules[16]. We confirmed the Adpgk neo-antigen mutation in MC-38 cells by cDNA sequencing (**Figure 2.16a**) and synthesized sHDL-Adpgk/CpG by

mixing nanodiscs with the neo-epitope modified with the CSS-linker and Cho-CpG. C57BL/6 mice immunized with sHDL-Adpgk/CpG generated remarkable 47-fold and 31-fold greater frequencies of neoantigen-specific CTLs, compared with the soluble Adpgk+CpG and Adpgk+CpG+Montanide groups, respectively ($p < 0.0001$, **Figure 2.16b,c**), and long-lived T-cell responses, as in the case of sHDL-SIINFEKL/CpG vaccination (**Figure 2.16d**), with tumor-specific cytotoxicity against MC-38 target cells (**Figure 2.17**). To investigate the therapeutic efficacy of nanodisc vaccination, C57BL/6 mice were inoculated subcutaneously with 10^5 MC-38 cells and treated with 15.5 nmol Adpgk and 2.3 nmol CpG (**Figure 2.18a-e**). Therapeutic vaccination with sHDL-Adpgk/CpG induced polyfunctional IFN-γ^+ and IFN-γ^+TNF-α^+ Adpgk-specific CD8α+ T-cells and substantially slowed MC-38 tumor growth (**Figure 2.18a-e**), compared with the traditional soluble Adpgk+CpG vaccine. However, no tumor rejection was observed in either vaccine groups, potentially due to immunosuppression within tumor microenvironment, as we detected high expression levels of programmed cell death-1 (PD-1) and its ligand PD-L1 among tumor-infiltrating CD8α+ T-cells and tumor cells, respectively (**Figure 2.19**). In order to block the immunosuppressive PD-1/PD-L1 pathway[39,40], we combined the vaccines with anti-PD-1 antibodies (αPD-1). Combination immunotherapy with sHDL-Adpgk/CpG and αPD-1 treatment generated robust neoantigen-specific CTL responses and led to complete tumor regression in ~88% mice (**Figure 2.20-2.21)**, compared with ~25% rate of tumor regression in the soluble Adpgk+CpG+αPD-1 group. Notably, 100% of surviving mice rejected the subsequent re-challenge with MC-38 cells inoculated at the contralateral flank or rechallenge with intravenous injection of MC-38 cells on day 70, indicating immunological memory against tumor recurrence (**Figure 2.22**).

2.4.5 Multi-epitope T-cell responses with cocktail nanodiscs

Finally, we evaluated our nanodisc platform in a melanoma model with B16F10 cells, as they are highly aggressive, poorly immunogenic, and hence hard to treat with conventional cancer vaccines. To prevent tumor immune escape by loss of a single mutant allele[41], we sought to elicit broad-spectrum T-cell responses by employing multiple antigens (multiAgs), including recently reported B16F10 mutated neo-epitopes (MHC I-restricted M27 and MHC II-restricted M30) as well as MHC I-restricted epitope from tyrosinase-related protein 2 (TRP2, a melanoma-associated Ag), all loaded in the same nanodiscs. C57BL/6 mice inoculated subcutaneously with 10^5 B16F10 cells were vaccinated with sHDL-multiAgs/CpG, eliciting a total of ~30% Ag-specific, IFN-γ^+ CD8α+ and CD4+ T-cells in peripheral blood, compared with only 1-3% induced by the soluble multiAgs+CpG or multiAgs+CpG+Montanide groups ($p < 0.0001$, **Figure 2.23)**. Vaccination with sHDL-multiAgs/CpG significantly inhibited B16F10 tumor growth, compared with the soluble or Montanide vaccines ($p < 0.0001$, **Figure 2.24a**). Notably, removing either M27/M30 or TRP2 from sHDL-multiAgs/CpG compromised its therapeutic efficacy, suggesting the benefits of broad CTL responses against neo-antigens and tumor-associated antigens (**Fig. 2.24b**). Lastly, we evaluated sHDL-multiAgs/CpG combined with dual immune checkpoint inhibitors. Combination immunotherapy with sHDL-multiAgs/CpG and αPD-1/αCTLA-4 treatment led to an impressive rate of B16F10 tumor rejection with ~90% of mice free of tumor, whereas the soluble multiAgs+CpG+αPD-1/αCTLA-4 treatment mediated tumor regression in ~38% of animals (**Figure 2.25**). Notably, 100% of surviving mice rejected the subsequent re-challenge with B16F10 cells inoculated at the contralateral flank or rechallenge with intravenous injection of B16F10 cells on day 70, indicating immunological memory against tumor recurrence (**Figure 2.26**).

Overall, our results have significant clinical importance since these nanodiscs, with an established manufacturing procedure suited for neo-antigen vaccination and excellent safety profiles in humans, can drastically improve co-delivery of antigens and adjuvants to LNs; sustain antigen presentation on DCs and cross-priming of T-cells; drive multivalent CD8α+ and CD4+ T-cell immunity against neo-antigens and tumor-associated antigens with long-term T-cell response; and significantly delay tumor growth in the setting of therapeutic vaccination. However, despite strong anti-tumor T-cell responses, nanodiscs administered as a monotherapy failed to eliminate tumors, possibly due to the immunosuppressive PD-L1/PD-1 pathway within the tumor microenvironment. Aiming to unleash the full cytotoxic potential of T-cells[39,40], we combined nanodisc vaccination with immune checkpoint inhibitors, achieving potently amplified therapeutic efficacy and eradication of MC-38 and B16F10 tumors in > 85% of animals. Although other nanosystems in the literature[5-15] may be also applicable, this is, to the best of our knowledge, the first demonstration of antitumor efficacy with personalized nanomedicine tailored with tumor-specific neo-antigens.

While the work presented here provides the framework for future clinical translation, our strategy designed to generate neoantigen-specific cellular immunity requires tumor DNA/RNA exome sequencing, identification of neo-antigens, and production of nanodiscs, followed by a multi-dose vaccine regimen, which collectively may protract the time window required for control of malignancies for late-stage patients. These issues may be tackled in the future by multi-thronged strategies that exploit combined immunotherapy targeted to humoral and innate arms of immunity[42] or radiation therapy[43] and select chemotherapeutics[44] known to delay tumor growth and synergize with T-cell vaccines.

2.5 Conclusions

We have developed a new nano-vaccine system ideally suited for individualized neo-epitope vaccination and demonstrated their potency to generate broad-spectrum T-cell responses with striking therapeutic efficacy when combined with immune checkpoint inhibitors. As the majority of somatic mutations in cancer cells are unique to each patient, cancer vaccines would require a personalized approach[16-19]. Coupled with the recent biomedical breakthroughs in neo-antigen screening and immune checkpoint blockade[39,40,45-47], our approach may offer a powerful yet facile strategy for producing cancer vaccines designed for each patient. Furthermore, this platform technology may be generally applicable for personalized therapeutics with a wide range of bioactive molecules and imaging agents. [48]

2.6 Figures

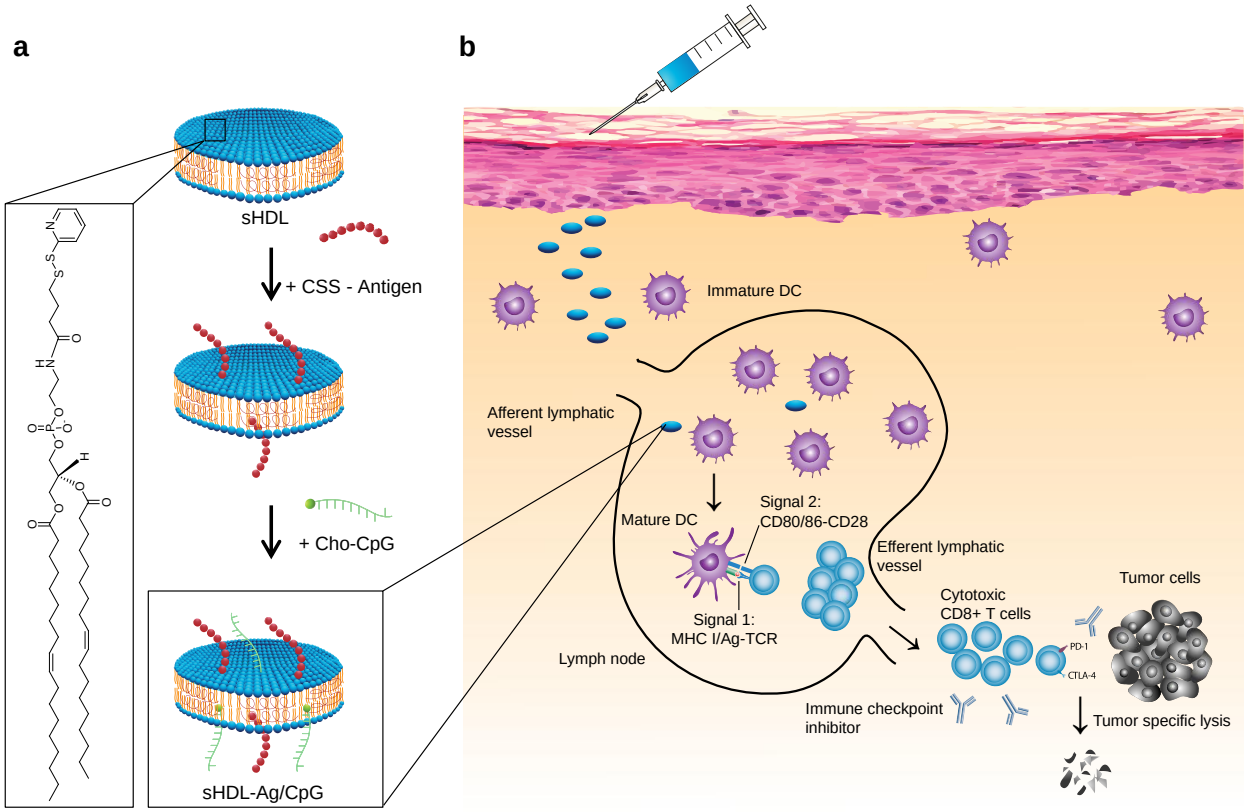

Figure 2.1. Design of sHDL nanodisc platform for personalized cancer vaccines. **a,** sHDL nanodiscs, composed of phospholipids and apolipoprotein-1 mimetic peptides (22A), are engineered for co-delivery of antigen (Ag) peptides and adjuvants. Pre-formed sHDL nanodiscs displaying 4 mol% DOPE-PDP are mixed with cysteine-modified Ag peptides, including tumor-specific mutated neo-antigens identified via tumor exome DNA sequencing, and subsequent incubation with cholesterol-modified immunostimulatory molecules (Cho-CpG) leads to formation of sHDL nanodiscs co-loaded with Ag and CpG (sHDL-Ag/CpG). **b,** Upon administration, sHDL nanodiscs efficiently co-deliver Ag and CpG to draining lymph nodes, promote strong and durable Ag presentation by dendritic cells (DCs) (Signal 1), and induce DC maturation (Signal 2), resulting in elicitation of robust Ag-specific CD8α+ cytotoxic T lymphocyte (CTL) responses. Activated CTLs recognize and kill their target cancer cells in peripheral tissues and exert strong anti-tumor efficacy. Combination immunotherapy with immune checkpoint blockade further amplifies the potency of nanodisc vaccination, leading to elimination of established tumors.

Table 2.1 Characterization of nanodiscs containing different 22A variants. Data represent mean ±SD (n=3)

Sample ID	Sequence	Size (d. nm)	PDI
22A	PVLDLFRELLNELLEALKQKLK	10.6 ± 0.2	0.18 ± 0.01
22A-1	PVLDEFREKLNEELEALKQKLK	N.D.	N.D.
22A-2	PVLDLFRELLNELLEZLKQKLK	25.6 ± 2.7	0.28 ± 0.10
22A-3	PVLDLFRELWNELLEALKQKLK	13.5 ± 0.5	0.25 ± 0.03
22A-4	PVLDLFRELLNELWEALKQKLK	14.3 ± 0.2	0.29 ± 0.01
22A-5	PVLDWFRELLNELLEALKQKLK	20.2 ± 2.2	0.27 ± 0.06
22A-6	PVLDLFRELLNEWLEALKQKLK	13.9 ± 0.2	0.29 ± 0.01
22A-7	PVLDEFRELLNELLEALKQKLK	13.6 ± 1.8	0.38 ± 0.10
22A-8	PVLDLFREKLNEELEALKQKLK	N.D.	N.D.
22A-9	KLKQKLAELLENLLERFLDLVP	N.D.	N.D.
22A-10	PVLDLFRELLNELLEALKQKLK (D-amino acids)	10.8 ± 0.3	0.19 ± 0.01

a

4^0C (stored for one month)

b

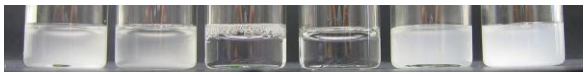

DOPC	+	-	-	-	-	-
POPC	-	+	-	-	-	-
DMPC	-	-	+	-	+	-
DPPC	-	-	-	+	-	+
22A	+	+	+	+	-	-

Figure 2.2. Effect of 22A variants and lipids on the formation of sHDL nanodisc. **a,** DMPC (containing 4% mol DOPE-PDP) and different 22A mutants were used to prepare sHDL. In addition to 22A that we have used throughout this study, several other 22A variants, including 22A composed of D-amino acids, formed homogeneous sHDL nanodiscs (as analyzed by dynamic light scattering) that remained stable up to one month at 4^0C. Data represent mean ± SD (n = 3). N.D., not determined due to aggregation. **b,** Synthesis of sHDL requires phospholipids with high transition temperature (T_m) and ApoA-mimetic peptides. DPPC and DMPC (T_m = 41°C and 24°C, respectively) but not POPC or DOPC (T_m = -2°C and -17°C, respectively), formed homogeneous sHDL in the presence of 22A and 4 mol% DOPE-PDP.

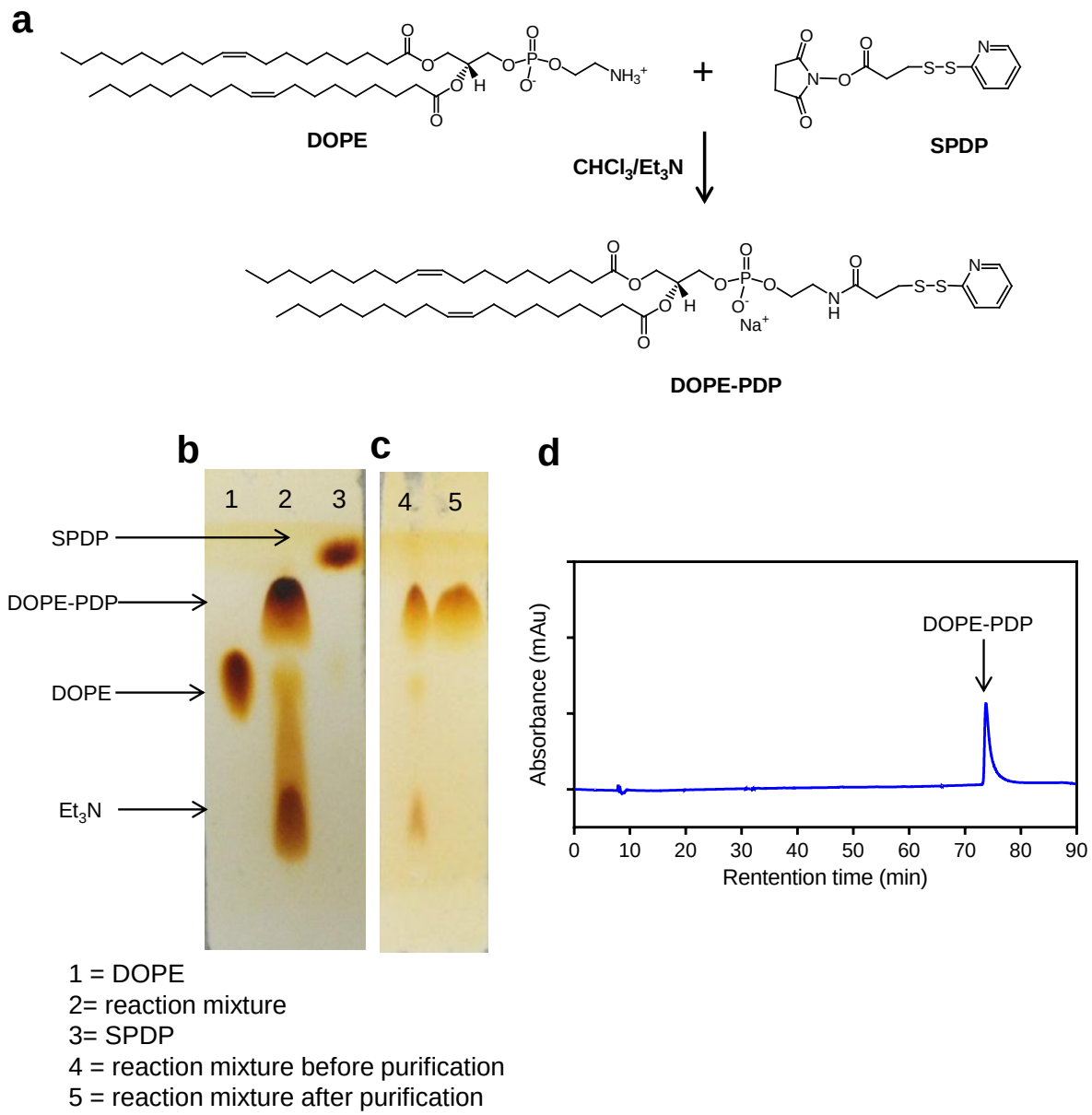

Figure 2.3. Synthesis of functional lipid DOPE-PDP. **a,** DOPE, SPDP (succinimidyl 3-(2-pyridyldithio) propionate) and triethylamine (1:1:1.5 molar ratio) were dissolved in chloroform and allowed to react in dark with stirring for 5 h. **b,** The reaction progress was monitored by thin layer chromatography (TLC), using the following mixture as the developing solvent: chloroform/methanol/water = 65/25/4 (volume ratio). **c-d,** The reaction mixture was purified using a silica gel column, and the purity was assessed by **c,** TLC and **d,** HPLC using the condition described in the Supplementary Materials and Methods section.

Table 2.2. Characterization of nanodiscs containing antigens and CpG. Data represent mean ±SD (n=3).

Formulations	% of PDP-lipid converted to Ag-lipid	% of Cho-CpG Inserted into sHDL	Size (d. nm)	PDI
sHDL-CSSSIINFEKL/CpG	92.0 ± 3.5%	98.5 ± 1.1%	10.5 ± 0.5	0.20 ± 0.02
sHDL-Adpgk/CpG	91.1 ± 3.1%	96.5 ± 1.8%	10.8 ± 0.3	0.22 ± 0.02
sHDL-multiAgs/CpG	92.8 ± 3.9%	95.3 ± 2.7%	10.9 ± 0.6	0.28 ± 0.13

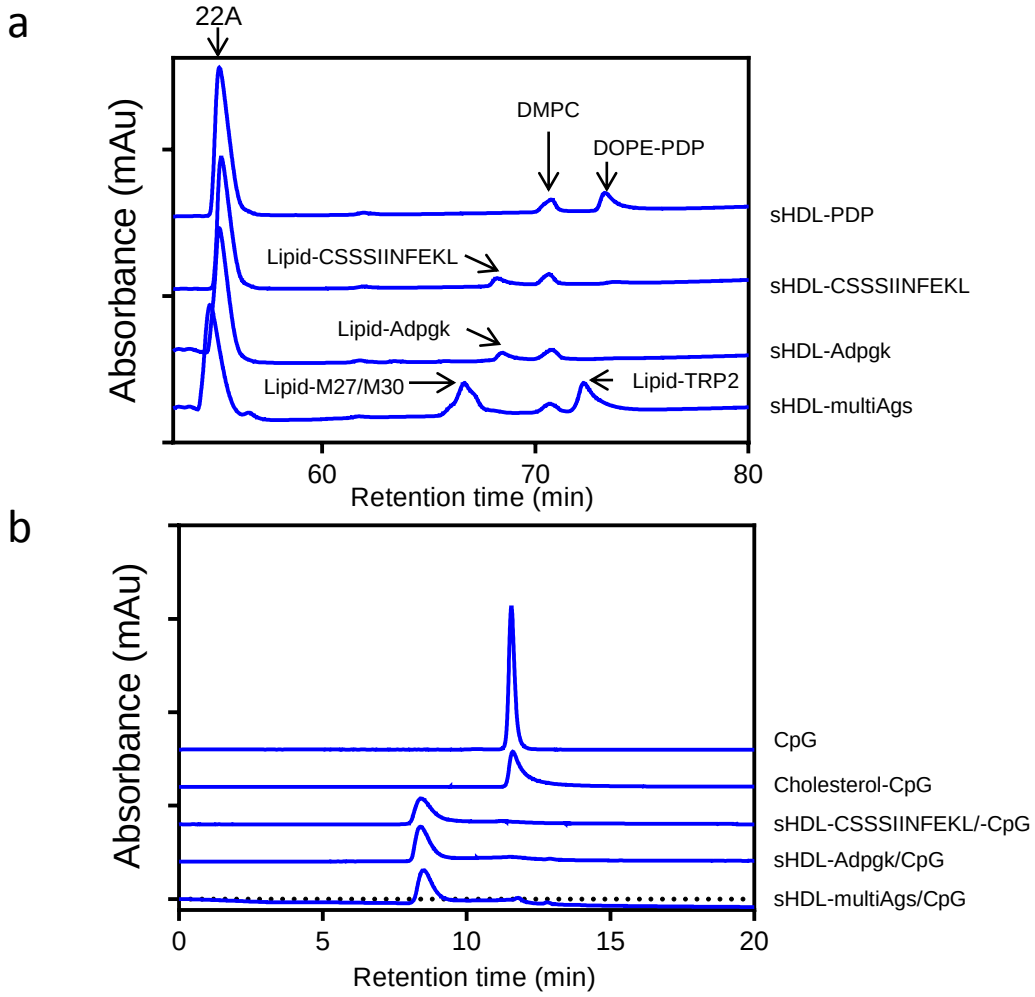

Figure 2.4. Preparation and characterization of sHDL-CSSSIINFEKL/CpG and sHDL-Adpgk/CpG. **a,** HPLC chromatograms confirming the conjugation of CSSSIINFEKL, Adpgk and multiple antigen peptides (TRP2, M27, and M30) to sHDL. **b,** GPC showed homogeneity of all formulations and efficient loading of Cho-CpG in sHDL nanodiscs.

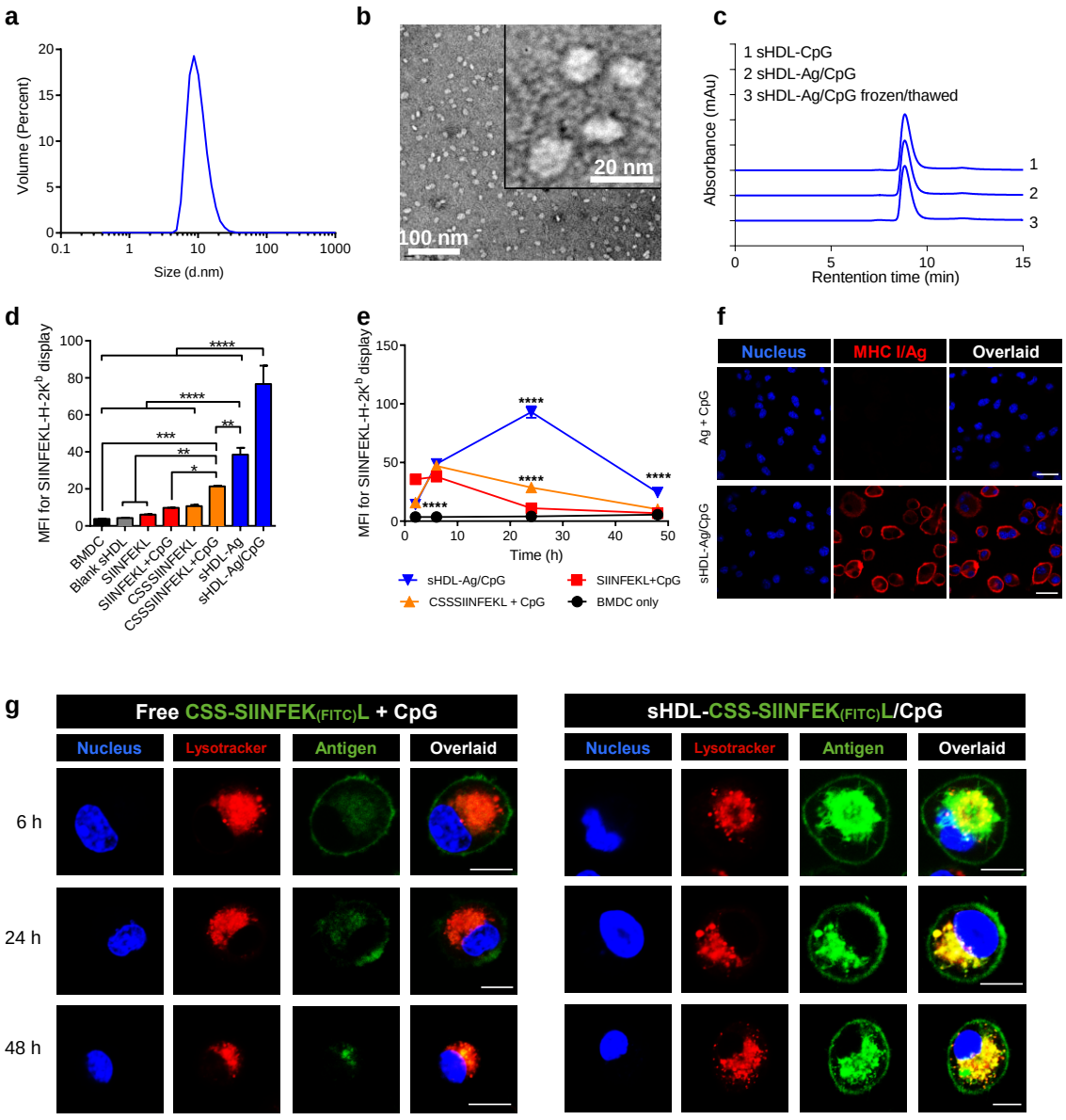

Figure 2.5. Strong and durable Ag presentation mediated by sHDL nanodiscs **a,** Dynamic light scattering analysis and **b,** transmission electron microscopy imaging showed uniform sHDL-Ag/CpG (10.5 nm ± 0.5 average diameter) with nanodisc-like morphology. Scale bar = 100 nm. Scale bar in the inset = 20 nm. **c,** Homogeneity of nanodiscs was maintained after sterile-filtration (0.22 μm), and long-term storage (8 weeks) at -20ºC, followed by thawing at 37ºC. **d-e,** BMDCs were incubated with vaccine formulations for **d,** 24 h or **e,** indicated lengths of time, and Ag presentation was quantified by flow-cytometry analysis of DCs stained with 25-D1.16 mAb that recognizes SIINFEKL-H-2K^b complex. **f-g,** Confocal microscopy images of JAWSII cells (immature DCs). **f,** JAWSII cells were incubated with free Ag+CpG or sHDL-Ag/CpG for 24 h and stained with 25-D1.16 mAb. Scale bars = 20 μm. **g,** JAWSII cells were incubated with free CSSSIINFEK$_{(FITC)}$L + CpG or sHDL-CSSSIINFEK$_{(FITC)}$L/CpG for 6, 24, or 48 h, followed by staining with Hochest and Lysotracker. Scale bars = 10 μm. The data show mean ± SD from a representative experiment (n = 3) from 2-4 independent experiments. * $p < 0.05$, ** $p < 0.01$, *** $p < 0.001$, and **** $p < 0.0001$, analyzed by (**d**) one-way or (**e**) two-way ANOVA with Bonferroni multiple comparisons post-test.

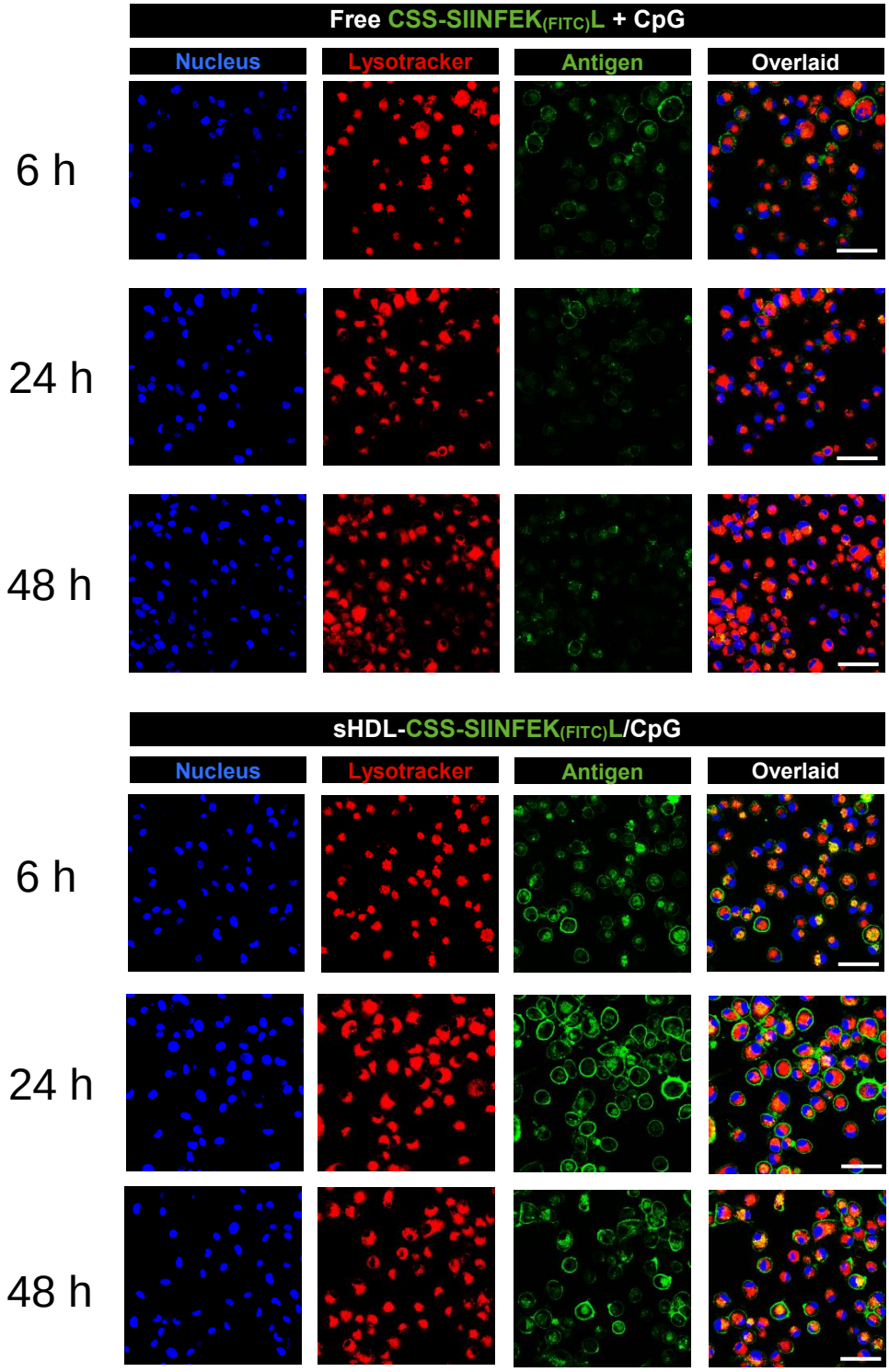

Figure 2.6. Ag delivery and presentation mediated by sHDL-Ag/CpG (broader view). JAWSII cells were incubated with free CSSSIINFEK$_{(FITC)}$L + CpG or sHDL-CSSSIINFEK$_{(FITC)}$L/CpG for 6, 24, or 48 h, and stained with Hochest and Lysotracker. Scale bar = 50 μm.

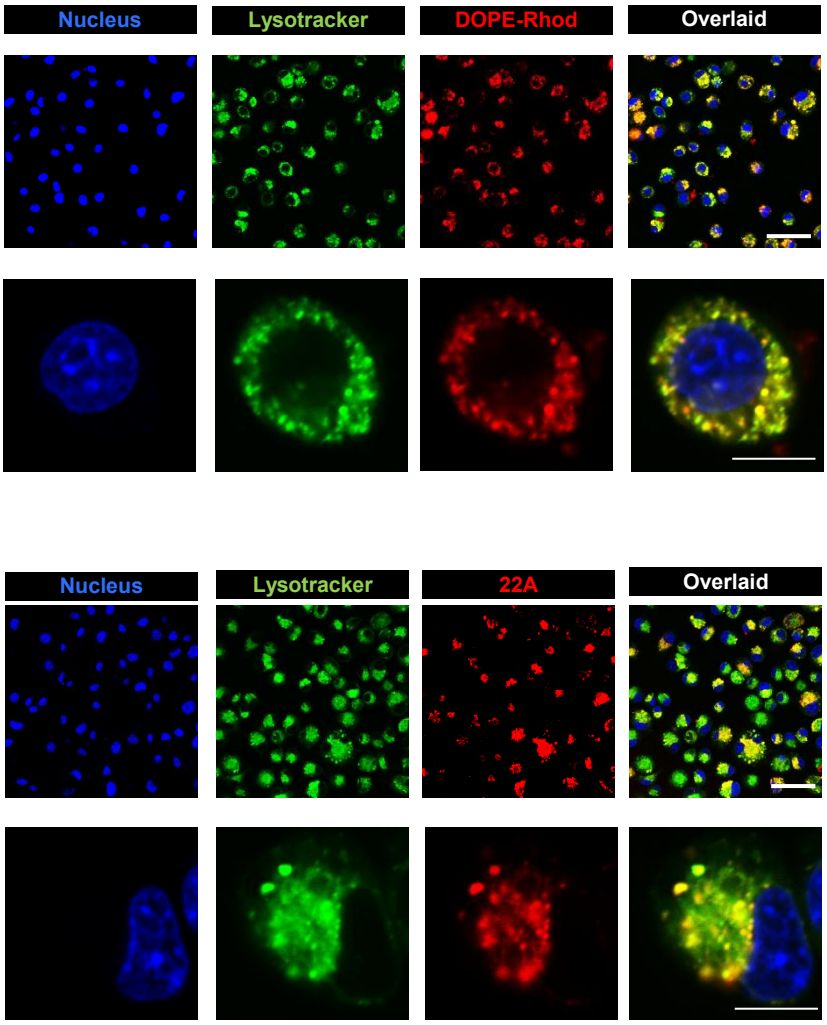

Figure 2.7. Intracellular delivery of sHDL. JAWSII cells were incubated for 24 h with sHDL containing either Rhodamine-labeled DOPE (DOPE-Rhod) or Texas Red-labeled 22A and stained with Hochest and Lysotracker. Scale bar = 50 μm for broader view and 20 μm for single cell imaging .

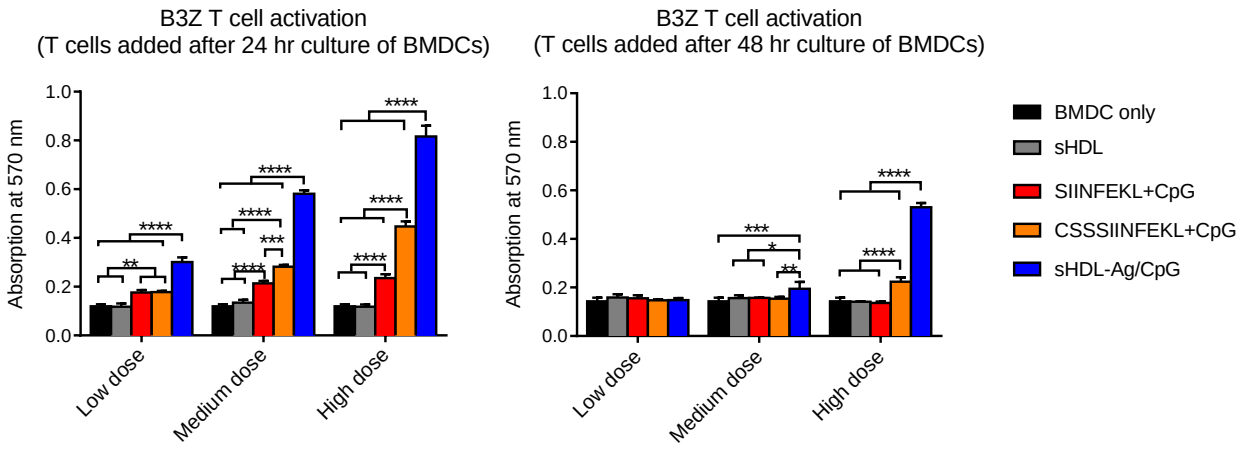

Figure 2.8, BMDCs were incubated with different concentrations of indicated formulations: low dose = 20 nM SIINFEKL and 3 nM CpG; medium dose = 100 nM SIINFEKL and 15 nM CpG; and high dose = 500 nM SIINFEKL and 75 nM CpG. After incubation for 24 h or 48 h, BMDCs were co-cultured with SIINFEKL-specific B3Z T-cell hybridoma for another 24 h, followed by assessment of T cell activation. The data show mean ± SD from a representative experiment (n = 3) from 2-4 independent experiments. * $p < 0.05$, ** $p < 0.01$, *** $p < 0.001$, and **** $p < 0.0001$, analyzed by two-way ANOVA with Bonferroni multiple comparisons post-test.

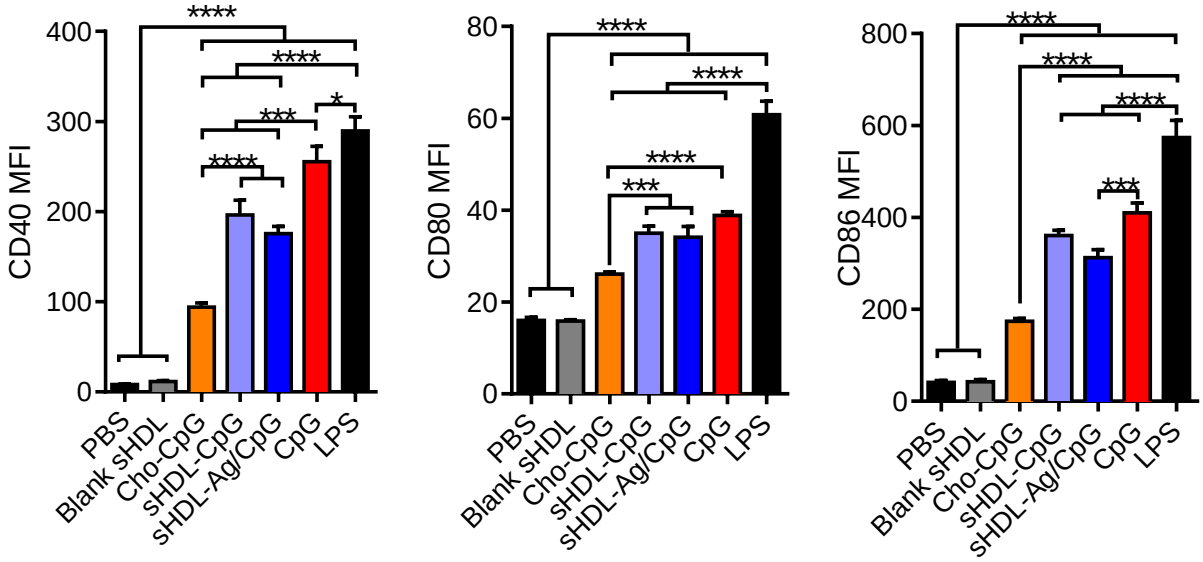

Figure 2.9. Stimulation of bone marrow-derived dendritic cells (BMDCs) by CpG-containing formulations. BMDCs were incubated with blank sHDL or 75 nM CpG formulations for 24 h. The expression levels of CD40, CD80, and CD86 were measured by flow cytometry after staining with corresponding fluorophore-labeled antibodies. The data show mean ± SD from a representative experiment (n = 3) from 3 independent experiments. * $p< 0.05$, ** $p< 0.01$, *** $p< 0.001$, **** $p < 0.0001$, one-way ANOVA with Bonferroni post-test.

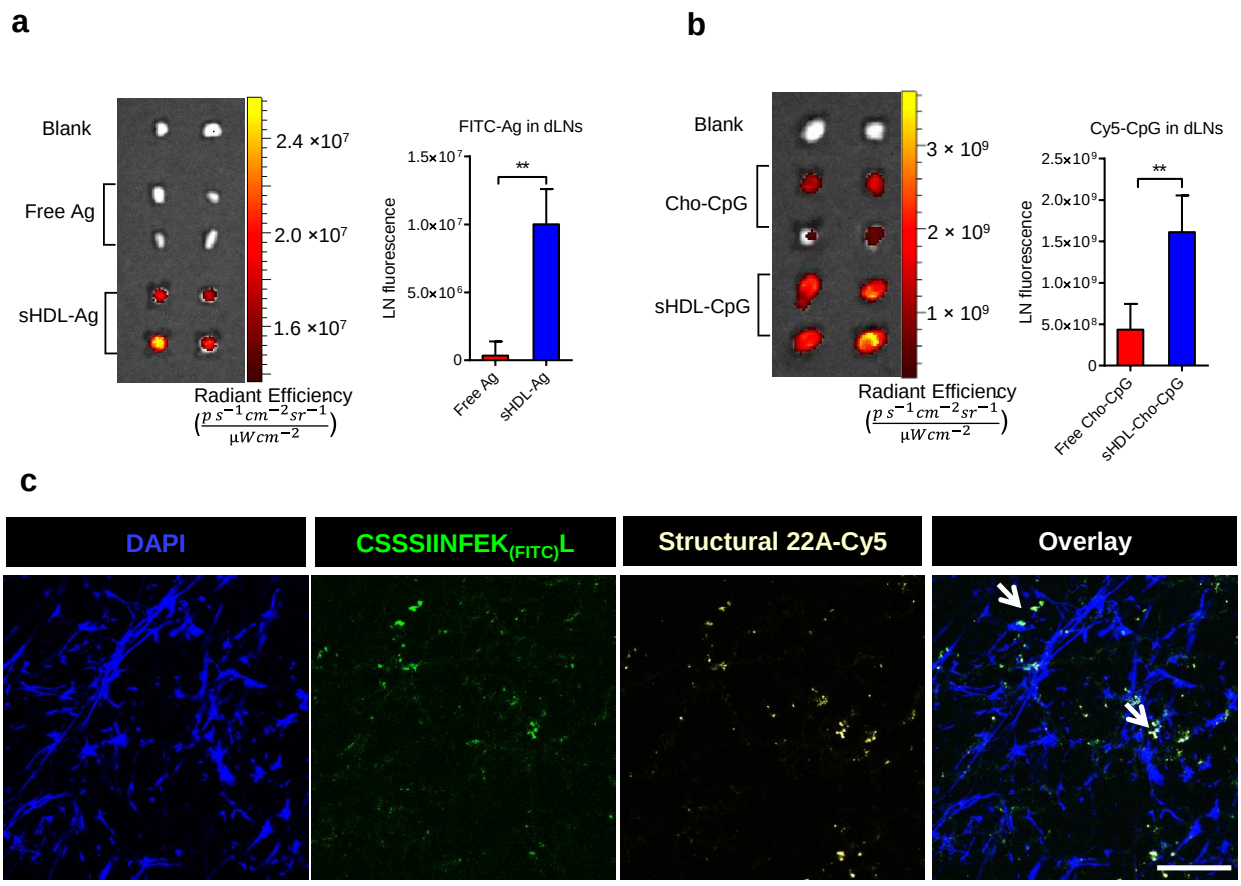

Figure 2.10. Vaccine nanodiscs for LN-targeting of Ag and adjuvants and elicitation of CTL responses. **a-b,** C57BL/6 mice were administered subcutaneously at tail base with **a,** 31 nmol FITC-tagged Ag (CSSSIINFEK$_{(FITC)}$L) or **b,** 2.3 nmol Cho-CpG (20% labeled by Cy5) in free soluble or sHDL form, and fluorescence signal in the draining inguinal LNs were quantified with IVIS after 24 h. **c,** sHDL-CSSSIINFEK$_{(FITC)}$L nanodiscs incorporated with Cy5-labeled 22A were injected subcutaneously (31 nmol antigen peptides/mouse) at the tail base of C57BL/6 mice. After 24 h, draining inguinal lymph nodes were harvested and frozen sections were prepared for confocal microscopy. The confocal images showed antigen peptides and 22A were colocalized in the lymph nodes (indicated by white arrows). Scale bar = 50 µm. The data show mean ± SD from a representative experiment (n = 4-5) from 2-3 independent experiments. * $p < 0.05$, ** $p < 0.01$, *** $p < 0.001$, and **** $p < 0.0001$, analyzed by (**a-b**) two-tailed unpaired Student's *t* test.

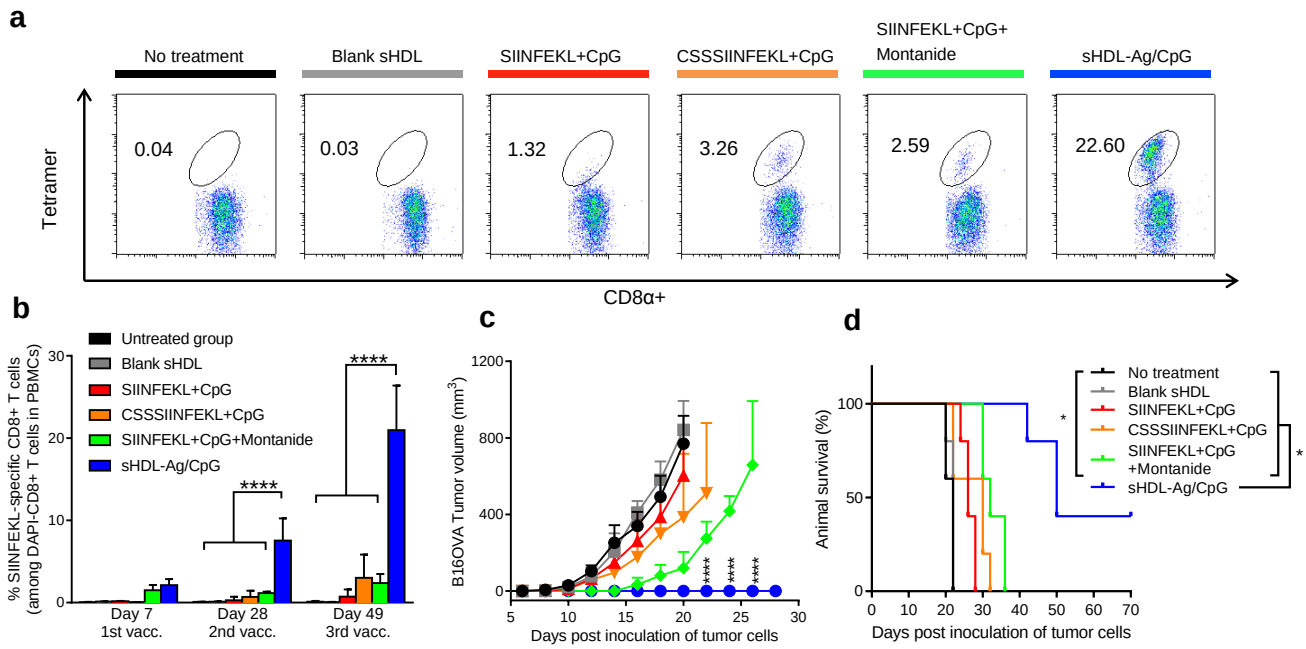

Figure 2.11. Vaccine nanodiscs for LN-targeting of Ag and adjuvants and elicitation of CTL responses. **a-d,** C57BL/6 mice were immunized with the indicated formulations (15.5 nmol Ag peptide and 2.3 nmol CpG) on days 0, 21, and 42. **a,** Shown are their representative scatter plots on day 49 and **b** the frequency of SIINFEKL-specific CD8α+ T-cells in peripheral blood measured 7 days post each immunization by flow-cytometry analysis of tetramer+ CD8α+ T-cells. **c-d,** On day 50, pre-vaccinated animals were challenged with subcutaneous flank injection of 2×10^5 B16OVA cells. Tumor growth and animal survival were measured over time. The data show mean ± SD from a representative experiment (n = 4-5) from 2-3 independent experiments. * $p < 0.05$, ** $p < 0.01$, *** $p < 0.001$, and **** $p < 0.0001$, analyzed by (**b,c**) two-way ANOVA with Bonferroni multiple comparisons post-test or log rank (Mantel-Cox) test (**d**). Asterisks in panel **c** indicate statistically significant differences between sHDL-Ag/CpG and SIINFEKL+CpG+Montanide.

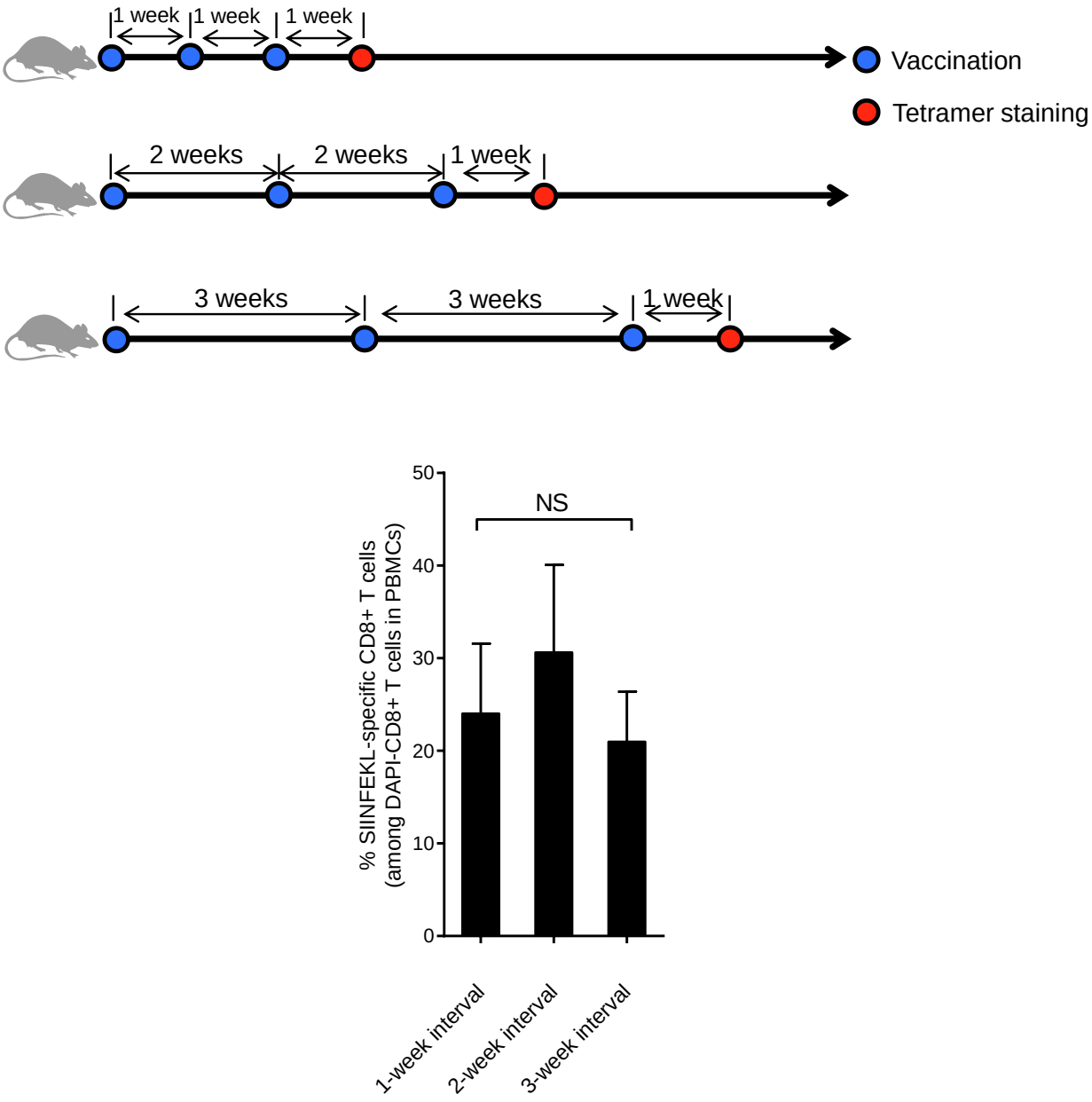

Figure 2.12. C57BL/6 mice were immunized with sHDL-Ag/CpG for 3 times in an 1-week interval, 2-week interval or 3-week interval. Shown are the percent of SIINFEKL-specific CD8+ T cells among PBMCs one week after the third vaccination. Data represent mean ± SD from a representative experiment (n = 5) from 2-3 independent experiments. NS, non-statistically significant.

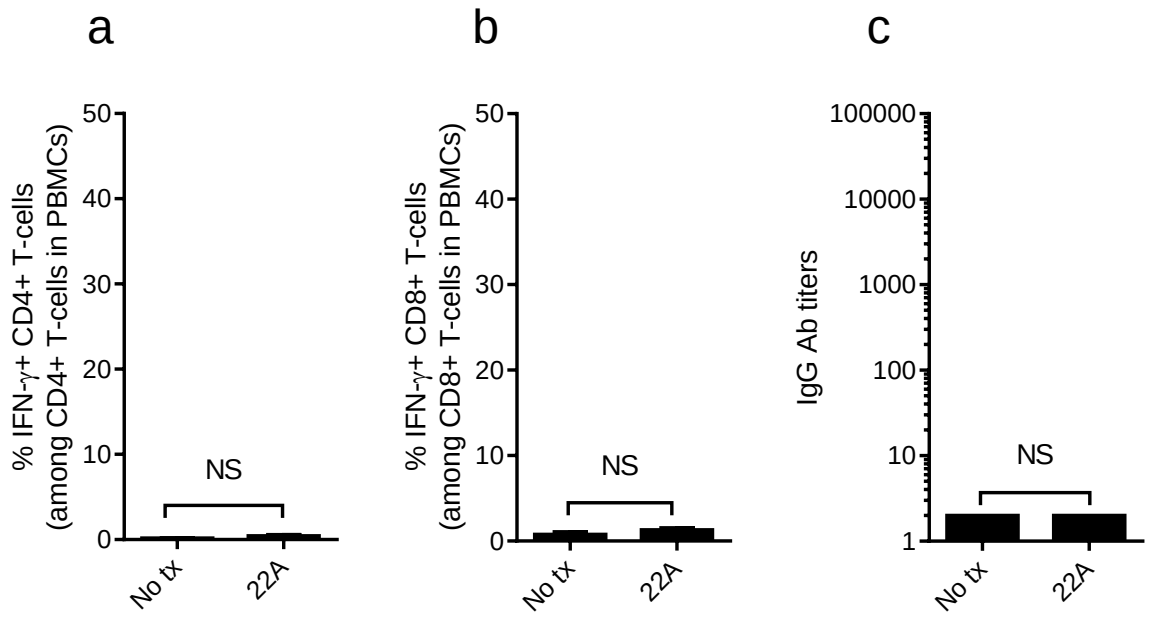

Figure 2.13. C57BL/6 mice were immunized with sHDL-CpG (equivalent to 2.3 nmol CpG per dose) for 3 times in an 1-week interval. Shown are the percent of 22A-specific CD4+ T cells (a), 22A-specific CD8+ T cells (b) among PBMCs one week after the third vaccination, and (c) the titers of IgG antibody against 22A one week after the third vaccination. Data represent mean ± SD from a representative experiment (n = 3) from 2 independent experiments. NS, non-statistically significant.

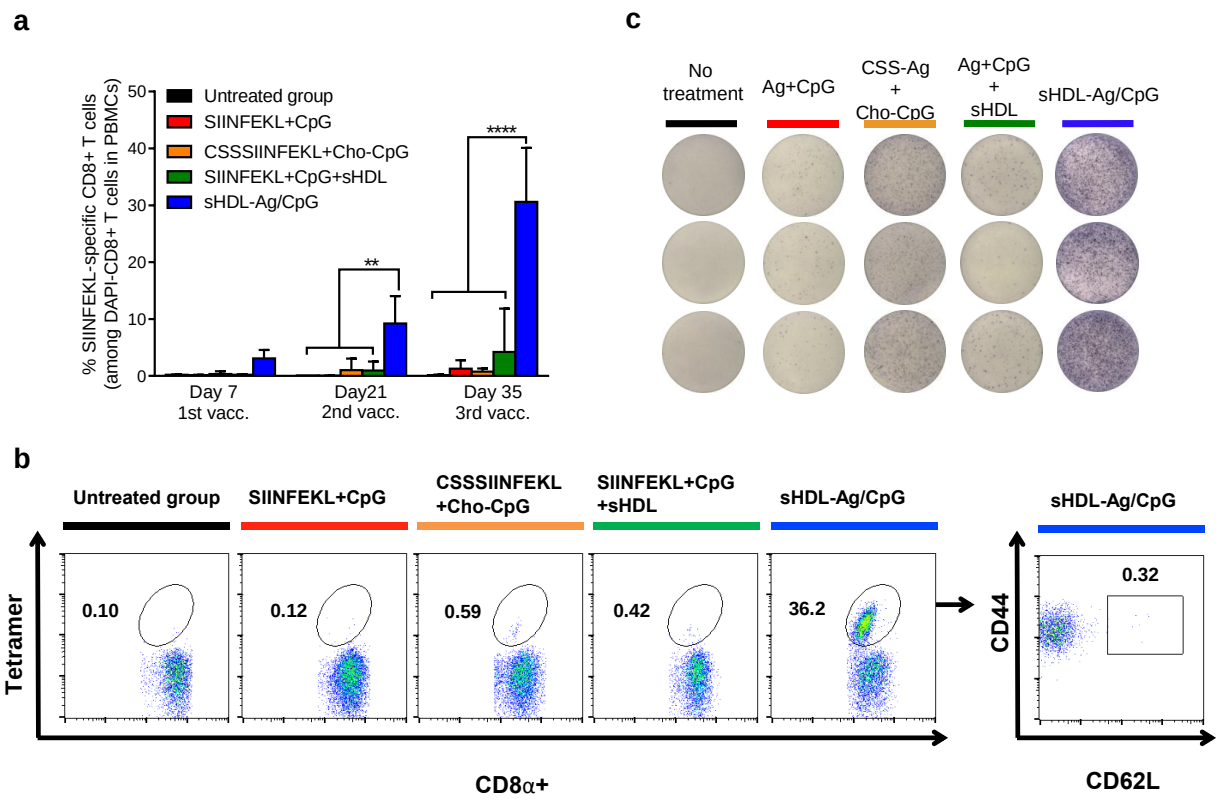

Figure 2.14. Vaccine nanodiscs for LN-targeting of Ag and adjuvants and elicitation of CTL responses. **a-b,** C57BL/6 mice were immunized with the indicated formulations (15.5 nmol Ag peptide and 2.3 nmol CpG) three times in a biweekly interval. Shown are **a,** percent of SIINFEKL-specific CD8α+ T-cells in peripheral blood; **b**, representative scatter plots for SIINFEKL-specific CD8+ T-cells among PBMCs on day 35 and their effector CD8+ T-cell phenotype as analyzed by CD44 and CD62L staining; and c**,** ELISPOT analysis of IFN-γ spot-forming cells among splenocytes after *ex vivo* restimulation with SIINFEKL on day 35. The data show mean ± SD from a representative experiment (n = 4-5) from 2-3 independent experiments. ** $p < 0.01$, and **** $p < 0.0001$, analyzed by two-way ANOVA with Bonferroni multiple comparisons post-test.

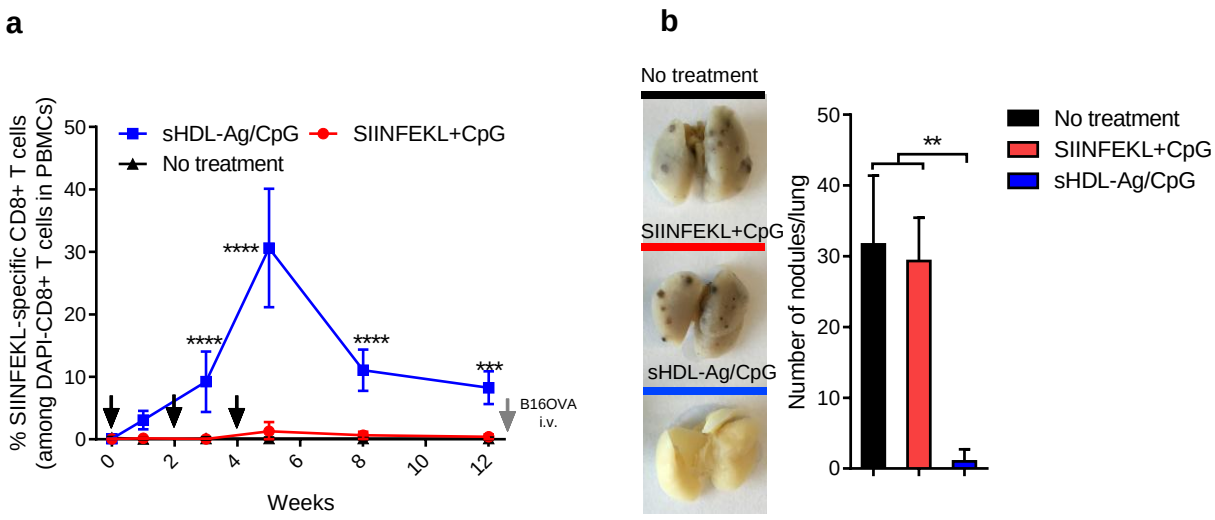

Figure 2.15. Vaccine nanodiscs for LN-targeting of Ag and adjuvants and elicitation of CTL responses. **a,** C57BL/6 mice were immunized with the indicated formulations (15.5 nmol Ag peptide and 2.3 nmol CpG) in a biweekly interval. Shown are Ag-specific CD8α+ T-cell responses measured over 12 weeks post vaccination (black arrows indicate days of immunizations). **b**, Vaccinated mice in **(a)** were intravenously challenged with 5×10^4 B16OVA cells two months after the third vaccination. Shown are pictures of the lungs and numbers of lung metastatic nodules counted on day 20 after the B16OVA challenge. The data show mean ± SD from a representative experiment (n = 4-5) from 2-3 independent experiments. ** $p < 0.01$, *** $p < 0.001$, and **** $p < 0.0001$, analyzed by (**a**) two-way ANOVA, or (**b**) one-way ANOVA with Bonferroni multiple comparisons post-test.

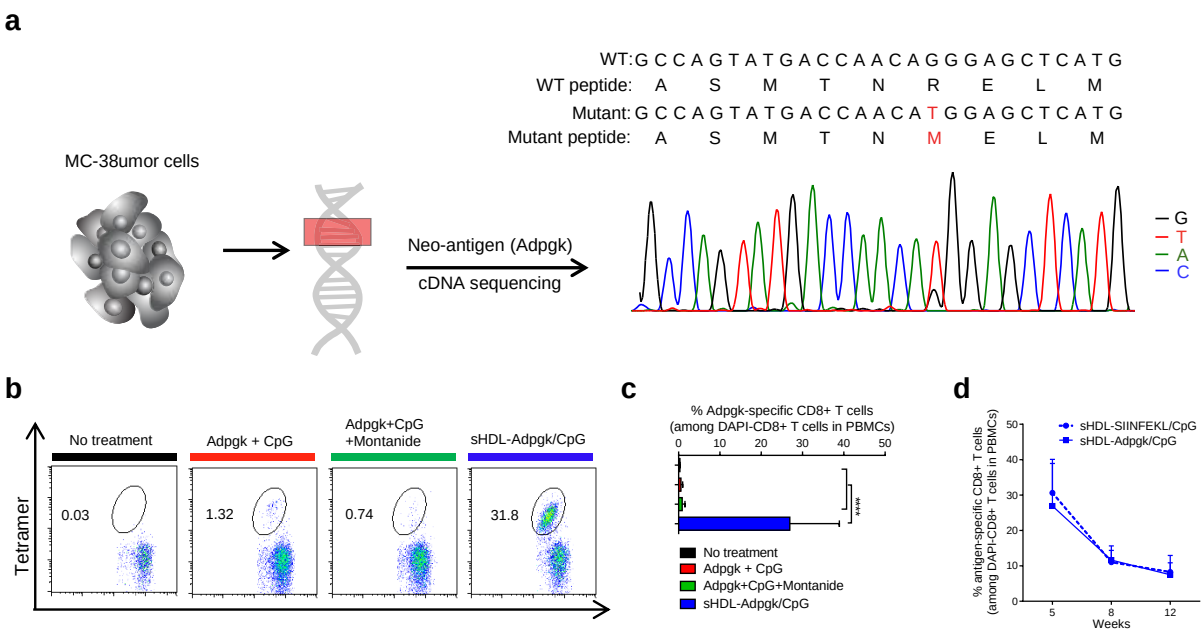

Figure 2.16. Nanodisc-based neo-antigen vaccination for personalized immunotherapy. **a,** Mutation of Adpgk in MC-38 murine colon adenocarcinoma cells was confirmed by sequencing cDNA of Adpgk. **b-d,** C57BL/6 mice were vaccinated three times with the indicated formulations (equivalent to 15.5 nmol mutated Adpgk peptide and 2.3 nmol CpG) in a bi-weekly interval, and the frequency of Adpgk-specific CD8α+ T-cells in peripheral blood was measured . Shown are **b**, the representative scatter plots, and **c**, the frequency of Adpgk-specific CTLs on day 35. **d**, Clonal contraction of Ag-specific CD8α+ T-cell responses elicited by sHDL-Adpgk/CpG and sHDL-SIINFEKL/CpG vaccines was monitored for eight weeks after the last vaccination. The data show mean ± SD from a representative experiment (n = 5-10) from 2-3 independent experiments. **** $p < 0.0001$, analyzed by (**c**) one-way ANOVA with Bonferroni multiple comparisons post-test.

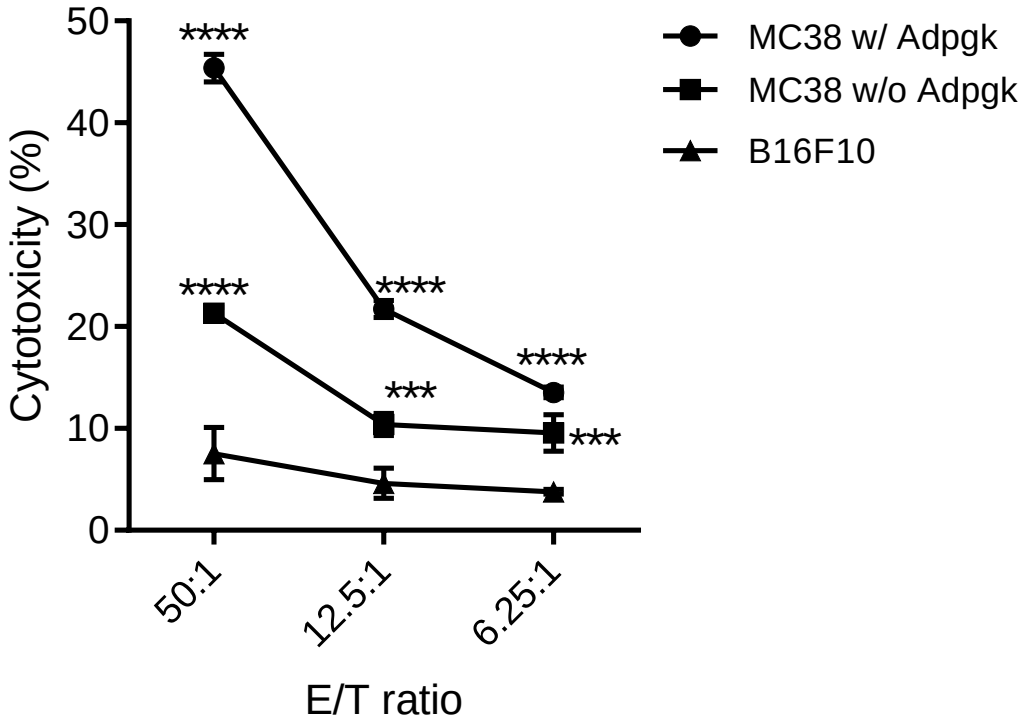

Figure 2.17. Effector splenocytes (E) were incubated with 5000 target MC38 cells (T) pulsed with the neoantigen peptide (MC38 w/Adpgk) or not pulsed with the neoantigen peptide (MC38 w/o Adpgk) at indicated ratios for 6 ~ 8 h. Then specific lysis was analyzed by the nonradioactive LDH release assay by following the manufacturer's instructions. Data represent mean ± SD from a representative experiment (n = 3). *** $p < 0.001$, and **** $p < 0.0001$, analyzed by two-way ANOVA with Bonferroni post-test. Asterisks next to MC38 w/Adpgk indicate the difference for all groups. Asterisks next to MC38 w/o Adpgk indicate the difference between MC38 w/o Adpgk and B16F10.

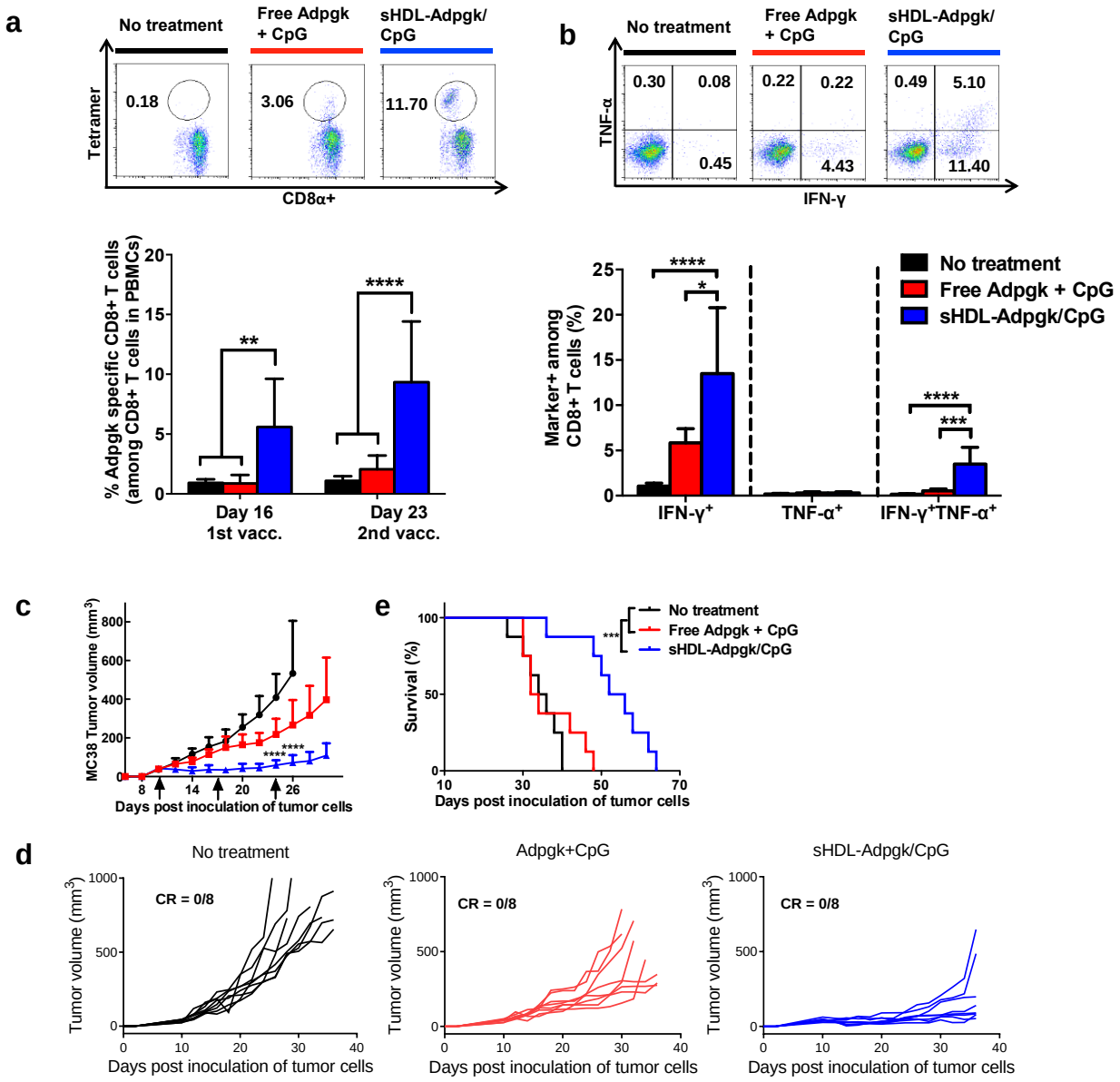

Figure 2.18. sHDL-Ag/CpG for vaccination against mutated tumor-specific neo-antigen. **a-e,** C57BL/6 mice were inoculated subcutaneously with 1×10^5 MC-38 tumor cells and vaccinated with the indicated formulations (equivalent to 15.5 nmol mutated Adpgk peptide and 2.3 nmol CpG) on days 10, 17, and 24. Shown are **a,** the frequencies of Adpgk-specific CD8α+ T-cells among PBMCs and representative scatter plots of Adpgk-tetramer+ CD8α+ T-cells on day 23; **b,** the percentages of intracellular IFN-γ^+, TNF-α^+, and IFN-γ^+TNF-α^+ CD8α+ T-cells among PBMCs on day 30 after ex vivo restimulation with the mutated Adpgk Ag and their representative scatter plots. **c,** average tumor growth; **d,** individual tumor growth of MC-38 tumor masses; and **e,** animal survival. The data show mean ± SD from a representative experiment (n = 5-8) from 2-3 independent experiments. * $p < 0.05$, ** $p < 0.01$, *** $p < 0.001$, and **** $p < 0.0001$, analyzed by (**a,b,c**) two-way ANOVA with Bonferroni post-test or (**e**) log-rank (Mantel-Cox) test. Asterisks in panels **c** indicate statistically significant differences between sHDL-Ag/CpG and all other groups.

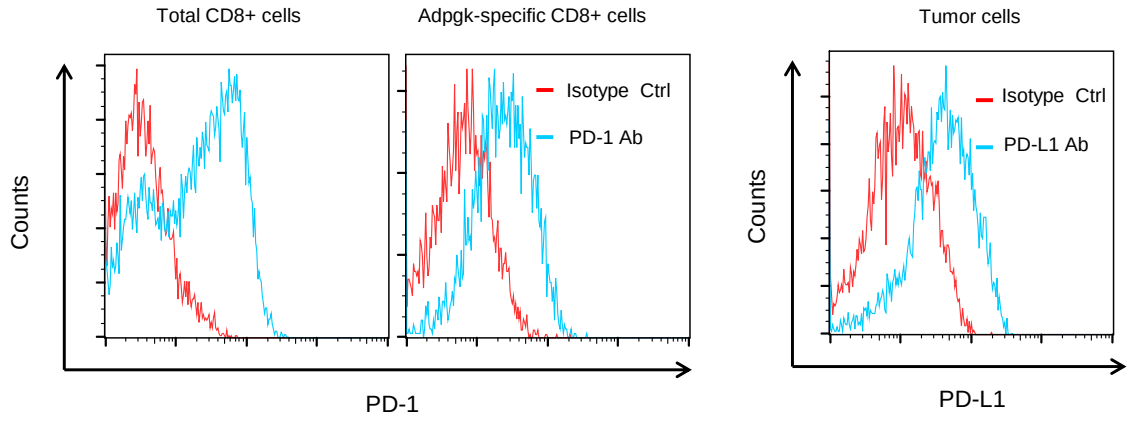

Figure 2.19. Expression levels of PD-1 on tumor-infiltrating lymphocytes and PD-L1 on tumor cells were confirmed by flow cytometry on day 23 from the experiment shown in **Fig. 4e**. Shown are representative scatter plots of PD-1 expression on intratumoral total CD8+ T cells and Adpgk-specific CD8+ T cells, and PD-L1 expression on tumor cells.

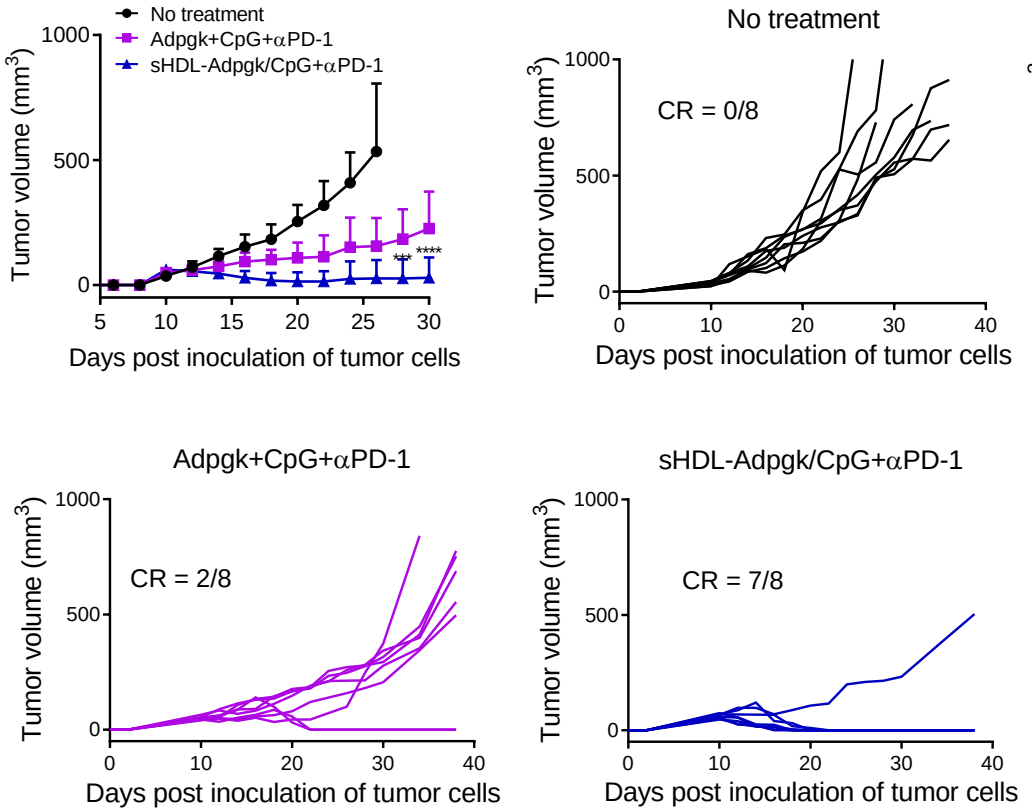

Figure 2.20.C57BL/6 mice were inoculated subcutaneously with 10^5 MC-38 tumor cells and vaccinated with the indicated formulations (equivalent to 15.5 nmol mutated Adpgk peptide and 2.3 nmol CpG) on days 10 and 17. On days 1 and 4 after each vaccination, mice were administered intraperitoneally with αPD-1 (100 μg/mouse). Average and individual MC-38 tumor growth curves are shown. The data show mean ± SD from a representative experiment (n = 5-8) from 2-3 independent experiments. *** $p < 0.001$, and **** $p < 0.0001$, analyzed by two-way ANOVA with Bonferroni post-test.

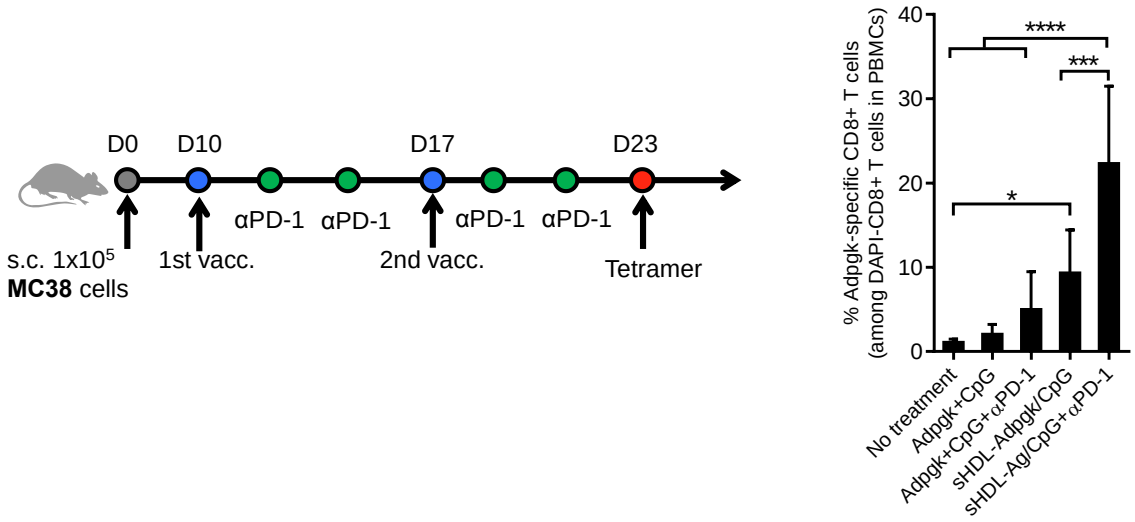

Figure 2.21. C57BL/6 mice were inoculated subcutaneously with 1×10^5 MC-38 tumor cells and vaccinated with the indicated formulations (equivalent to 15.5 nmol mutated Adpgk peptide and 2.3 nmol CpG) on days 10 and17 and αPD-1 (100 μg per dose) on days 1 and 4 after each vaccination. Shown are the frequencies of Adpgk-specific CD8α+ T-cells among PBMCs on day 23. Data represent mean ± SD from a representative experiment (n = 5-8) from 2 independent experiments. * $p < 0.05$, *** $p < 0.001$, and **** $p < 0.0001$, analyzed by one-way ANOVA with Bonferroni post-test.

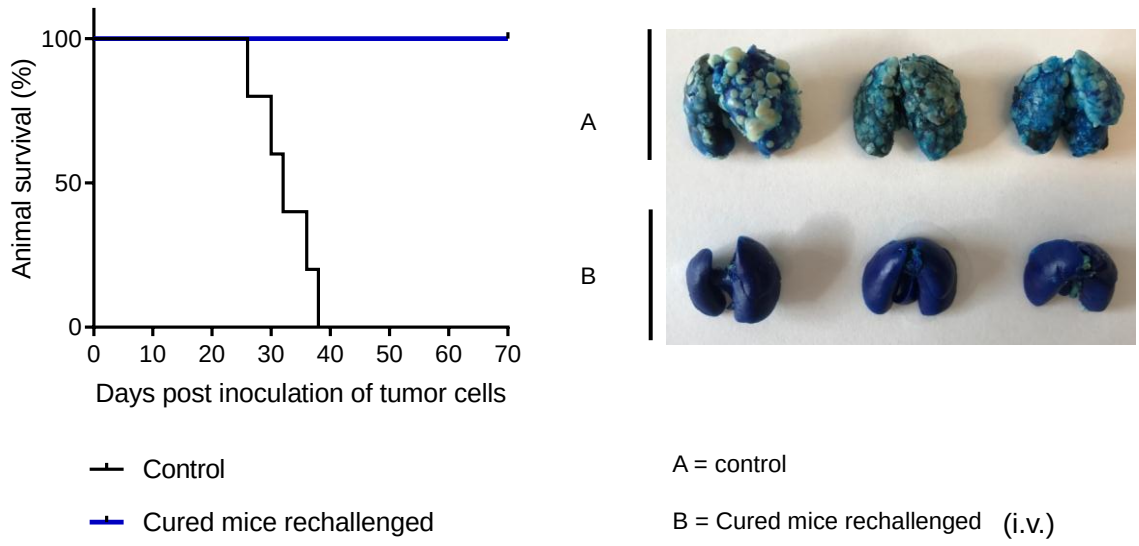

Figure 2.22. On day 70, cured mice were re-challenged subcutaneously (**a**) or intravenously (**b**) with 1×10^5 MC38 cells. Shown are the animal survival (**a**) and lung metastasis (**b**) of MC38 cells on day 25 after re-challenge. Naïve mice were used as control and inoculated with the same number of tumor cells.

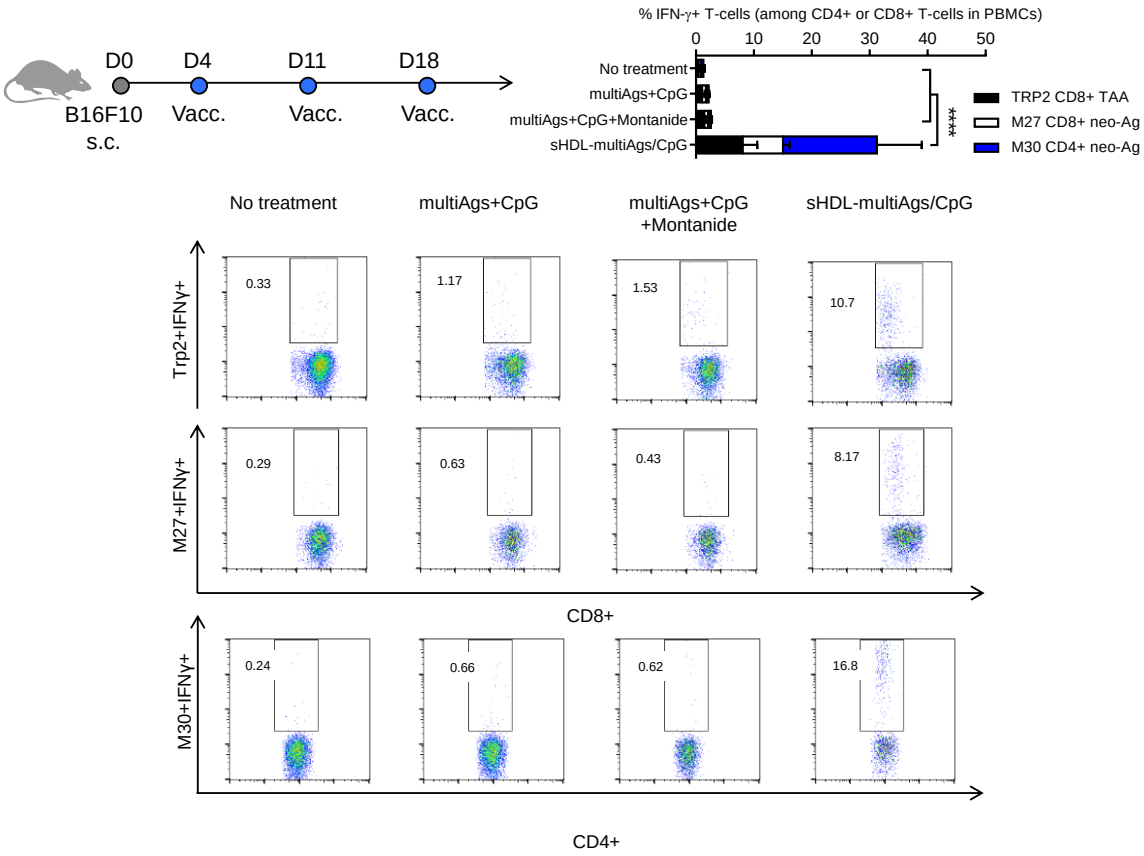

Figure 2.23. C57BL/6 mice were injected with 1×10^5 B16F10 cells on day 0. On days 4, 11, and 18, tumor-bearing mice were vaccinated with indicated formulations (multiAgs = Trp2 + M27 + M30). Shown are the percent of IFN-γ^+ CD8α+ or CD4+ T cells in peripheral blood measured by intracellular cytokine staining and representative scattering plots of intracellular cytokine staining of PBMCs from mice vaccinated with indicated formulations on day 17. The data show mean ± SD from a representative experiment (n = 5) from 2-3 independent experiments. **** $p < 0.0001$, analyzed by one-way ANOVA with Bonferroni multiple comparisons post-test.

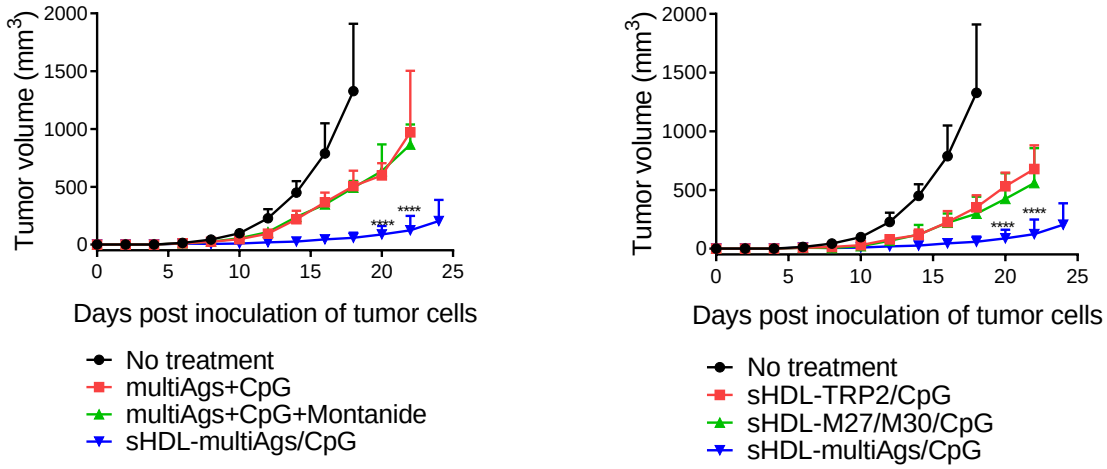

Figure 2.24. C57BL/6 mice were inoculated subcutaneously with 10^5 melanoma B16F10 cells and vaccinated on days 4, 11, and 18 with indicated formulations (10 nmol of each antigen peptide and 2.3 nmol of CpG). Shown are the average B16F10 tumor growth curves. The data show mean ± SD from a representative experiment (n = 5) from 2-3 independent experiments. **** $p < 0.0001$ analyzed by two-way ANOVA with Bonferroni multiple comparisons post-test. Asterisks indicate statistically significant differences between sHDL-Ag/CpG and all other treatment groups.

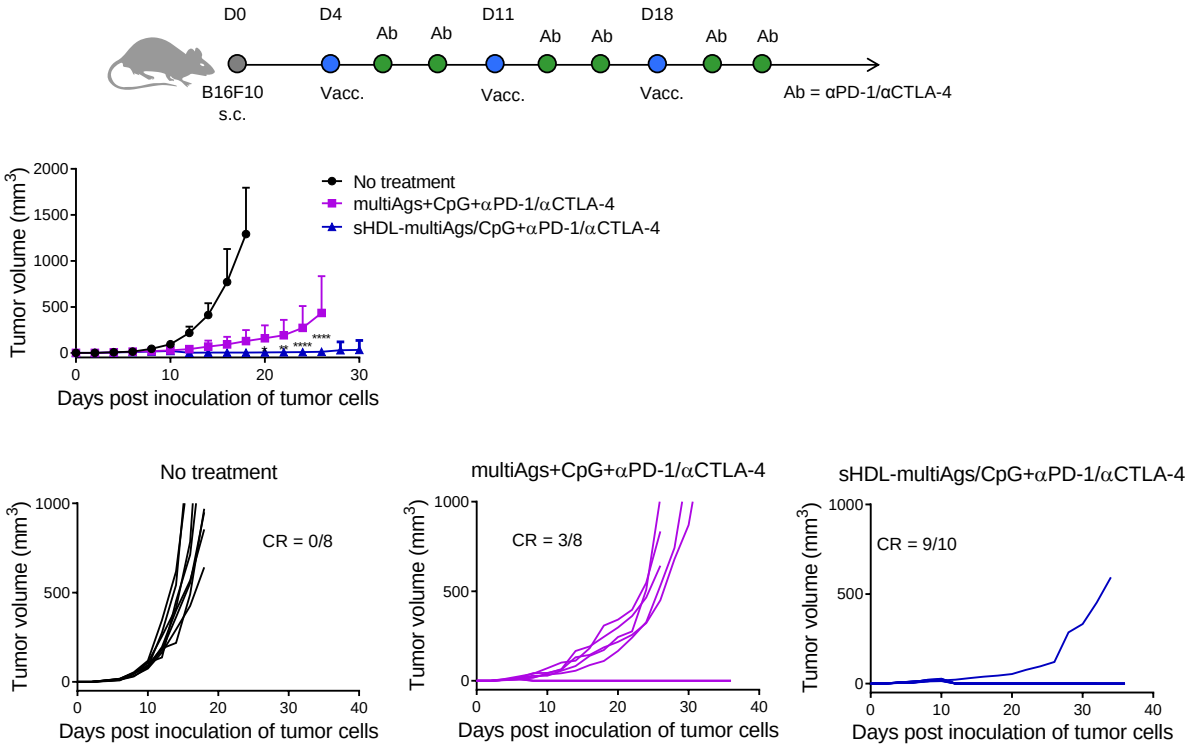

Figure 2.25. C57BL/6 mice were inoculated subcutaneously with 10^5 melanoma B16F10 cells and vaccinated on days 4, 11, and 18 with indicated formulations (10 nmol of each antigen peptide and 2.3 nmol of CpG). For the combination immunotherapy, on days 1 and 4 after each vaccination, αPD-1 and αCTLA-4 (100 μg/mouse each) were administered intraperitoneally. Shown are average and individual B16F10 tumor growth curves. The data show mean ± SD (n = 8-10). * $p < 0.05$, ** $p < 0.01$, and **** $p < 0.0001$, analyzed by two-way ANOVA with Bonferroni multiple comparisons post-test.

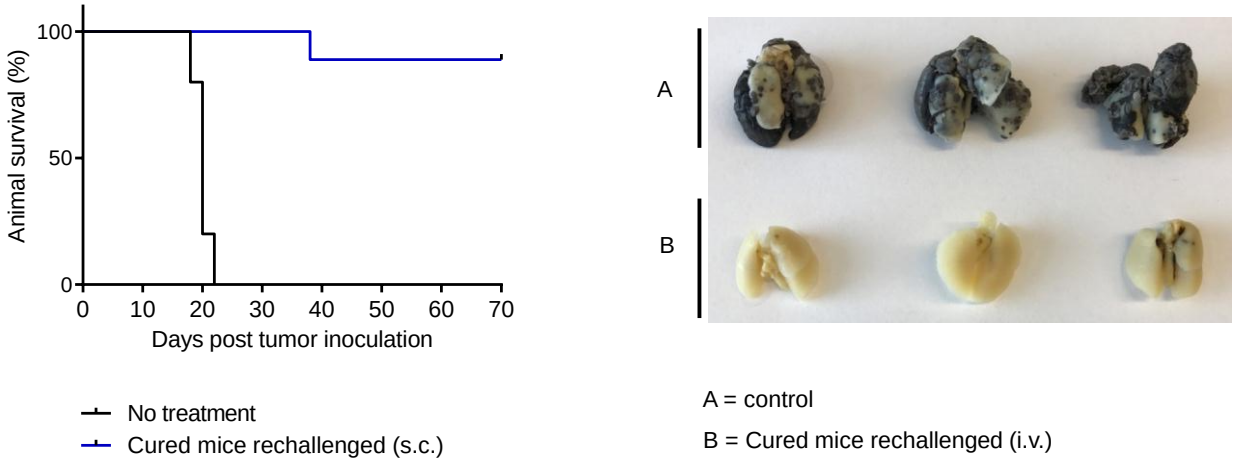

Figure 2.26. On day 70, cured mice were re-challenged subcutaneously (**a**) or intravenously (**b**) with 1×10^5 B16F10 cells. Shown are the animal survival (**a**) and lung metastasis (**b**) of B16F10 cells on day 25 after re-challenge. Naïve mice were used as control and inoculated with the same number of tumor cells.

2.7 References

1. Melief CJ, van der Burg SH. Immunotherapy of established (pre)malignant disease by synthetic long peptide vaccines. *Nat Rev Cancer.* May 2008;8(5):351-360.

2. Speiser DE, Lienard D, Rufer N, et al. Rapid and strong human CD8+ T cell responses to vaccination with peptide, IFA, and CpG oligodeoxynucleotide 7909. *J Clin Invest.* Mar 2005;115(3):739-746.

3. Fourcade J, Kudela P, Andrade Filho PA, et al. Immunization with analog peptide in combination with CpG and montanide expands tumor antigen-specific CD8+ T cells in melanoma patients. *J Immunother.* Oct 2008;31(8):781-791.

4. Hailemichael Y, Dai Z, Jaffarzad N, et al. Persistent antigen at vaccination sites induces tumor-specific CD8(+) T cell sequestration, dysfunction and deletion. *Nat Med.* Apr 2013;19(4):465-472.

5. Reddy ST, van der Vlies AJ, Simeoni E, et al. Exploiting lymphatic transport and complement activation in nanoparticle vaccines. *Nat Biotechnol.* Oct 2007;25(10):1159-1164.

6. Moon JJ, Suh H, Bershteyn A, et al. Interbilayer-crosslinked multilamellar vesicles as synthetic vaccines for potent humoral and cellular immune responses. *Nat Mater.* Mar 2011;10(3):243-251.

7. Lee IH, Kwon HK, An S, et al. Imageable antigen-presenting gold nanoparticle vaccines for effective cancer immunotherapy in vivo. *Angew Chem Int Ed.* Aug 27 2012;51(35):8800-8805.

8. Li AV, Moon JJ, Abraham W, et al. Generation of effector memory T cell-based mucosal and systemic immunity with pulmonary nanoparticle vaccination. *Sci Transl Med.* Sep 25 2013;5(204):204ra130.

9. Jeanbart L, Ballester M, de Titta A, et al. Enhancing efficacy of anticancer vaccines by targeted delivery to tumor-draining lymph nodes. *Cancer Immunol Res.* May 2014;2(5):436-447.

10. Xu Z, Wang Y, Zhang L, Huang L. Nanoparticle-delivered transforming growth factor-beta siRNA enhances vaccination against advanced melanoma by modifying tumor microenvironment. *ACS nano.* Apr 22 2014;8(4):3636-3645.

11. Liu H, Moynihan KD, Zheng Y, et al. Structure-based programming of lymph-node targeting in molecular vaccines. *Nature.* Mar 27 2014;507(7493):519-522.

12. Rosalia RA, Cruz LJ, van Duikeren S, et al. CD40-targeted dendritic cell delivery of PLGA-nanoparticle vaccines induce potent anti-tumor responses. *Biomaterials.* Feb 2015;40:88-97.

13. Chiu YC, Gammon JM, Andorko JI, Tostanoski LH, Jewell CM. Modular vaccine design using carrier-free capsules assembled from polyionic immune signals. *ACS Biomater Sci Eng.* 2015;1(12):1200-1205.

14. Fan Y, Moon JJ. Nanoparticle Drug Delivery Systems Designed to Improve Cancer Vaccines and Immunotherapy. *Vaccines (Basel).* 2015;3(3):662-685.

15. Lizotte PH, Wen AM, Sheen MR, et al. In situ vaccination with cowpea mosaic virus nanoparticles suppresses metastatic cancer. *Nat Nanotechnol.* 2016;13(3):295-303.

16. Yadav M, Jhunjhunwala S, Phung QT, et al. Predicting immunogenic tumour mutations by combining mass spectrometry and exome sequencing. *Nature.* Nov 27 2014;515(7528):572-576.

17. Kreiter S, Vormehr M, van de Roemer N, et al. Mutant MHC class II epitopes drive therapeutic immune responses to cancer. *Nature.* Apr 30 2015;520(7549):692-U269.

18. Rajasagi M, Shukla SA, Fritsch EF, et al. Systematic identification of personal tumor-specific neoantigens in chronic lymphocytic leukemia. *Blood.* Jul 17 2014;124(3):453-462.

19. Schumacher TN, Schreiber RD. Neoantigens in cancer immunotherapy. *Science.* Apr 3 2015;348(6230):69-74.

20. Wolfrum C, Shi S, Jayaprakash KN, et al. Mechanisms and Optimization of *in Vivo* Delivery of Lipophilic siRNAs. *Nat Biotechnol.* Oct 2007;25(10):1149-1157.

21. Fischer NO, Rasley A, Corzett M, Hwang MH, Hoeprich PD, Blanchette CD. Colocalized delivery of adjuvant and antigen using nanolipoprotein particles enhances the immune response to recombinant antigens. *J Am Chem Soc.* Feb 13 2013;135(6):2044-2047.

22. Duivenvoorden R, Tang J, Cormode DP, et al. A statin-loaded reconstituted high-density lipoprotein nanoparticle inhibits atherosclerotic plaque inflammation. *Nat Commun.* 2014;5:3065.

23. Li D, Gordon, S., Schwendeman, A. & Remaley, A.T. Apolipoprotein mimetic peptides for stimulating cholesterol efflux. In: Anantharamaiah GMG, D., ed. *Apolipoprotein Mimetics in the Management of Human Disease*. Switzerland: Springer; 2015:29-42.

24. Khan M, Lalwani, N., Drake, S., Crockatt, J. & Dasseux, J. Single-dose intravenous infusion of ETC-642, a 22-Mer ApoA-I analogue and phospholipids complex, elevates HDL-C in atherosclerosis patients. *Circulation.* 2003;108 (Suppl IV):563-564.

25. Miles J, et al. . Single-dose tolerability, pharmacokinetics, and cholesterol mobilization in HDL-C fraction following intravenous administration of ETC-642, a 22-mer ApoA-I analogue and phospholipids complex, in atherosclerosis patients. *Proceedings of Arteriosclerosis Thrombosis and Vascular Biology* 2004;24:E19-E19.

26. Kuai R, Li D, Chen YE, Moon JJ, Schwendeman A. High-Density Lipoproteins: Nature's Multifunctional Nanoparticles. *ACS nano.* Mar 22 2016;10(3):3015-3041.

27. Alexis F, Pridgen E, Molnar LK, Farokhzad OC. Factors affecting the clearance and biodistribution of polymeric nanoparticles. *Mol Pharm.* Jul-Aug 2008;5(4):505-515.

28. Anselmo AC, Mitragotri S. A Review of Clinical Translation of Inorganic Nanoparticles. *AAPS J.* Sep 2015;17(5):1041-1054.

29. Kuai R, Yuan W, Qin Y, et al. Efficient delivery of payload into tumor cells in a controlled manner by TAT and thiolytic cleavable PEG co-modified liposomes. *Molecular pharmaceutics.* Oct 4 2010;7(5):1816-1826.

30. Lutz MB, Kukutsch N, Ogilvie AL, et al. An advanced culture method for generating large quantities of highly pure dendritic cells from mouse bone marrow. *J Immunol Methods.* Feb 1 1999;223(1):77-92.

31. Karbach J, Gnjatic S, Bender A, et al. Tumor-reactive CD8+ T-cell responses after vaccination with NY-ESO-1 peptide, CpG 7909 and Montanide ISA-51: association with survival. *Int J Cancer.* Feb 15 2010;126(4):909-918.

32. Gorrin-Rivas MJ, Arii S, Furutani M, et al. Mouse macrophage metalloelastase gene transfer into a murine melanoma suppresses primary tumor growth by halting angiogenesis. *Clin Cancer Res.* May 2000;6(5):1647-1654.

33. Ochyl LJ, Moon JJ. Whole-animal imaging and flow cytometric techniques for analysis of antigen-specific CD8+ T cell responses after nanoparticle vaccination. *J Vis Exp.* 2015(98):e52771.

34. Sanger F, Nicklen S, Coulson AR. DNA sequencing with chain-terminating inhibitors. *Proc Natl Acad Sci.* Dec 1977;74(12):5463-5467.

35. Hirosue S, Kourtis IC, van der Vlies AJ, Hubbell JA, Swartz MA. Antigen delivery to dendritic cells by poly(propylene sulfide) nanoparticles with disulfide conjugated peptides: Cross-presentation and T cell activation. *Vaccine.* Nov 23 2010;28(50):7897-7906.

36. Saini SK, Ostermeir K, Ramnarayan VR, Schuster H, Zacharias M, Springer S. Dipeptides promote folding and peptide binding of MHC class I molecules. *Proc Natl Acad Sci.* Sep 17 2013;110(38):15383-15388.

37. US National Library of Medicine. ClinicalTrials.gov [online], http://clinicaltrials.gov/show/NCT00819806, (2016).

38. US National Library of Medicine. ClinicalTrials.gov [online], http://clinicaltrials.gov/ct2/show/record/NCT00640861, (2016).

39. Topalian SL, Hodi FS, Brahmer JR, et al. Safety, activity, and immune correlates of anti-PD-1 antibody in cancer. *N Engl J Med.* Jun 28 2012;366(26):2443-2454.

40. Zou W, Wolchok JD, Chen L. PD-L1 (B7-H1) and PD-1 pathway blockade for cancer therapy: Mechanisms, response biomarkers, and combinations. *Sci Transl Med.* Mar 2 2016;8(328):328rv324.

41. Verdegaal EM, de Miranda NF, Visser M, et al. Neoantigen landscape dynamics during human melanoma-T cell interactions. *Nature.* Jun 27 2016.

42. Moynihan KD, Opel CF, Szeto GL, et al. Eradication of large established tumors in mice by combination immunotherapy that engages innate and adaptive immune responses. *Nat Med.* Oct 24 2016.

43. Formenti SC, Demaria S. Combining radiotherapy and cancer immunotherapy: a paradigm shift. *J Natl Cancer Inst.* Feb 20 2013;105(4):256-265.

44. Kang TH, Mao CP, Lee SY, et al. Chemotherapy acts as an adjuvant to convert the tumor microenvironment into a highly permissive state for vaccination-induced antitumor immunity. *Cancer Res.* Apr 15 2013;73(8):2493-2504.

45. Gubin MM, Zhang X, Schuster H, et al. Checkpoint blockade cancer immunotherapy targets tumour-specific mutant antigens. *Nature.* Nov 27 2014;515(7528):577-581.

46. Robbins PF, Lu YC, El-Gamil M, et al. Mining exomic sequencing data to identify mutated antigens recognized by adoptively transferred tumor-reactive T cells. *Nat Med.* Jun 2013;19(6):747-752.

47. Linnemann C, van Buuren MM, Bies L, et al. High-throughput epitope discovery reveals frequent recognition of neo-antigens by CD4+ T cells in human melanoma. *Nat Med.* Jan 2015;21(1):81-85.

48. Kuai R, Ochyl LJ, Bahjat KS, Schwendeman A, Moon JJ. Designer vaccine nanodiscs for personalized cancer immunotherapy. *Nat Mater.* Apr 2017;16(4):489-496.

Chapter 3 Nanodiscs for Targeted Withalongolides Delivery to Adrenocortical Carcinoma

3.1 Abstract

Adrenocortical carcinoma (ACC) is a rare endocrine malignancy and has a five-year survival rate of less than 35%. ACC cells require cholesterol for steroid hormone production, and this requirement is met via expression on the cell surface of a high level of the scavenger receptor (class B1; SR-B1), which is responsible for the uptake of high density lipoproteins (HDL) that carry and transport cholesterol *in vivo*. Here we describe how this natural lipid-carrier function of SR-B1 can be utilized to improve the tumor-targeted delivery of a novel natural product derivative withalongolide A-4,19,27-triacetate (WGA-TA), which has shown potent antitumor efficacy but poor aqueous solubility. Our strategy is to use synthetic HDL (sHDL) nanodiscs, which are effective in tumor targeted delivery due to their small size, long circulation half-life, documented safety, and ability to bind to SR-B1. In this study, we prepared sHDL nanodiscs using an optimized phospholipid composition combined with ApoA-I mimetic peptide (22A), which has previously been tested in clinical trials, to load WGA-TA. Following optimization, WGA-TA nanodiscs showed a drug encapsulation efficiency of 78%, a narrow particle size distribution (9.81 ± 0.41 nm), discoidal shape, and sustained drug release in PBS. WGA-TA-sHDL nanodiscs exhibited higher cytotoxicity in the ACC cell line H295R (IC_{50} 0.260 ± 0.045 μM) than did free WGA-TA (IC_{50} 0.492 ± 0.115 μM, $p < 0.05$). Fluorescent dye-loaded sHDL nanodiscs efficiently accumulated in H295R adrenal carcinoma xenografts 24 hours following dosing. Moreover, daily IP administration of 7 mg/kg of WGA-TA-loaded sHDL nanodiscs

significantly inhibited tumor growth during 21-day administration to H295R xenograft-bearing mice compared to placebo ($p < 0.01$). Collectively, these results suggest that WGA-TA-loaded nanodiscs may represent a novel and beneficial therapeutic strategy for the treatment of adrenocortical carcinoma.

3.2 Introduction

Adrenocortical carcinoma (ACC) is a rare endocrine malignancy with a poor prognosis.[1] The majority of the ACC patients have metastasis at the time of diagnosis, resulting in a five-year survival rate of less than 35%.[2] Complete surgical resection remains the standard of care today. Other commonly used pharmacological interventions include the adrenotoxic drug, mitotane (o,p'-DDD), which is administered either alone or in combination with other cytotoxic chemotherapy, such as etoposide, doxorubicin, and platinum agents.[3] Because this method of treatment has a relatively low response rate and carries significant systemic toxicity, better treatment methods are critically needed for more effective targeting and inhibition of ACC.

Recently, we showed that the novel semi-synthetic withalongolide A 4, 19, 27-triacetate, from the plant Physalis *longifolia,* targets several oncogenic pathway proteins implicated in ACC.[4] This toxicity occurs through a combined mechanism of induction of an oxidative stress-response in cancer cells along with functional inhibition of the molecular chaperone heat shock protein 90 (Hsp90) through its interaction with the co-chaperone CDC37.[4] Although WGA-TA has shown great efficacy both *in vitro* and *in vivo*, one significant limitation of its translational development has been its low aqueous solubility.[5]

ACC cells require cholesterol for steroidogenesis and are known to express the scavenger receptor class B type 1 (SR-B1) to take up cholesterol from circulating high density lipoprotein

(HDL).[6] Many patients with advanced ACC develop steroid over-secretion[7] and specific patient-derived ACC cell lines have been classified as “high cortisol secretors” (H295R) or “steroid non-secretors” (SW13).[8,9] In addition to ACC cells, lymphoma, prostate, breast and ovarian cancers have also been found to overexpress SR-B1 receptors.[10-12] In fact, in recent years, high SR-B1 expression has emerged as an indicator of aggressiveness in both prostate and breast cancer and a predictor of poor survival. Therefore, nanoparticles that recognize SR-B1 receptors can potentially improve the targeted delivery of drugs to a wide range of different cancers.

HDL is an endogenous nanoparticle ranging from 8 to 14 nm in diameter and mainly composed of lipids and apolipoproteins, with Apolipoprotein A-I (ApoA-I) acting as the main protein component.[13] The primary function of endogenous HDL involves effluxing excess cholesterol from cells in peripheral tissues and delivering it to the liver for metabolism. In addition to cholesterol, hormones, vitamins, signaling lipids, microRNAs, enzymes and even hydrophobic drugs have been found to associate with HDL, either by partitioning into the hydrophobic core of nanoparticle, inserting in the lipid layer, or binding to the negatively charged particle surface.[14,15] Thus, HDL, with its small size and large surface area, has emerged as an important vascular carrier of lipophilic products.

Several groups have utilized biomimetic HDL nanodiscs for drug delivery purposes.[16-19] Most biomimetic HDL has been prepared with full-length ApoA-I protein either purified from plasma or produced by recombinant means, which is then combined with lipids and drugs in the presence of surfactant to form HDL nanodiscs. In most cases, the resulting nanoparticles have a heterogeneous size distribution with an average particle size larger than that of endogenous HDL and thus require purification prior to use.[20] The resulting ApoA-I expression/purification and HDL assembly processes are technically complex and expensive; moreover, the process does not

assure the removal of clinically unacceptable impurities, such as endotoxins, surfactants, and particulates.

To circumvent some of these technical issues, our laboratory utilizes a fully synthetic ApoA-I-mimetic peptide, 22A, to prepare highly homogeneous sHDL with an average diameter of 10-12 nm. The surfactant-free assembly process, involves co-lyophilization of ApoA-I peptide, phospholipids, and anticancer or imaging agents from organic solvent solution followed by hydration with buffer to form sHDL.[21-23]. This specific ApoA-I peptide and same process for nanoparticle assembly were used to prepare ETC-642, an HDL product for treatment of cardiovascular diseases.[24,25] In clinical studies, ETC-642 was found to have long plasma residence time (~8 hours) and to be safe when administered at 30 mg/kg peptide (90 mg/kg total components) by weekly intravenous.[15,26] Prior clinical safety data with ETC-642 can facilitate clinical translation of sHDL-mediated drug delivery for treatment of adrenal diseases.

In the present study, we first characterized expression levels of SR-B1 in various ACC cell lines. Next, we explored cellular uptake of fluorescently labeled HDL nanoparticles in both high (H295R) and low (SW13) SR-B1-expressing ACC cell lines and examined the extent to which SR-B1 mediated the cellular uptake. We then confirmed the accumulation of sHDL in ACC tumor xenografts *in vivo*. For this, we optimized phospholipid composition of biomimetic sHDL to encapsulate a novel natural product derivative WGA-TA and characterized the nanoparticle size, morphology, drug loading, and drug release kinetics. The cytotoxicity of WGA-TA-sHDL was confirmed *in vitro* and then compared *in vivo* with free drug, blank HDL, and a model standard of care chemotherapy treatment using H295R tumor xenografts.

3.3 Materials and Methods

3.3.1 Materials

Phospholipids, including 1,2-dipalmitoyl-*sn*-glycero-3-phosphocholine (DPPC), egg sphingomyelin (SM), 1,2-dimyristoyl-*sn*-glycero-3-phosphocholine (DMPC), 1-palmitoyl-2-oleoyl-*sn*-glycero-3-phosphocholine (POPC), 1,2-dioleoyl-*sn*-glycero-3-phosphocholine (DOPC), and egg yolk phosphocholine (EPC) were purchased from NOF America Corporation (White Plains, NY). ApoA-I-mimetic peptide was synthesized by Genscript (Piscataway, NJ). WGA-TA was provided by Dr. Barbara N. Timmermann (University of Kansas). Fluorescent dyes 3,3'-dioctadecyloxacarbocyanine perchlorate (DiO) and 1,1'-dioctadecyl-3,3,3,3'-tetramethylindotricarbocyanine iodide (DiR) were purchased from Invitrogen. All other chemical reagents were obtained commercially and were of analytical grade.

3.3.2 Preparation of WGA-TA-loaded sHDL

Lipid mixtures (DPPC, SM, DMPC, POPC, DOPC, and EPC), 22A peptide, and the anticancer drug WGA-TA were dissolved in glacial acetic acid at predetermined ratios (Table 1). The acetic acid was removed by freeze-drying and the powder was hydrated at 15 mg/mL 22A peptide concentration with PBS (pH 7.4). The suspension was cycled 3 times between 50 ℃ (3 min) and 20 ℃ (3 min) with gentle shaking to obtain drug-loaded sHDL nanoparticles. The fluorophore-loaded sHDL were prepared using the same protocol but the anticancer drug was instead replaced with DiO or DiR dyes at 2:1:0.02 weight ratio of phospholipids to 22A peptide and to dye.

3.3.3 Characterization of WGA-TA-loaded sHDL

The drug encapsulation efficiency was determined using the desalting-column centrifugation method. Briefly, WGA-TA-sHDL was passed through the desalting column (cut off = 7000 Da) to remove any unencapsulated drug. Ethanol was added to break sHDL and dissolve the drug

before HPLC analysis.[27] WGA-TA concentration was determined by HPLC using isocratic elution with 35% A (water with 0.1% acetic acid) and 65% B (methanol with 0.1% acetic acid) at a flow rate of 0.7 mL/min. A C18 column (250 × 4.6 mm) was used for separation and the detector wavelength was set at 230 nm. Dynamic light scattering (DLS) and gel permeation chromatography (GPC) were employed for the analysis of average size, size distribution and purity of WGA-TA-loaded sHDL nanoparticles. For DLS, 10 μl of the sHDL were diluted to 1 mL with PBS before measurement on the Malvern Zetasizer Nano (ZSP). For GPC, 40 μl of the sHDL formulation (0.5 mg/mL 22A peptide) were injected into the HPLC equipped with a TSK 2000 GPC column. The flow rate was set at 0.7 mL/min, and the detector wavelength was 220 nm. Morphology of sHDL particles was further characterized by transmission electron microscopy (TEM). All images were acquired on a JEM 1200EX electron microscope (JEOL USA, Peabody, MA) equipped with an AMT XR-60 digital camera (Advanced Microscopy Techniques Corp, Woburn, MA).[28]

To evaluate the *in vitro* release profile of drugs, 1 mL of 0.15 mg/mL free drug (dissolved at 0.3 mg/mL in DMSO and diluted to 1 mL with PBS) or 1 mL of 0.15 mg/mL of WGA-TA-loaded sHDL was added in a dialysis bag (6-8 kDa), which was sealed and placed in 200 mL PBS (pH 7.4) containing 0.1% Tween 80.[29,30] The contents were gently shaken at 100 rpm in a 37°C air bath shaker. An equal amount of free drug was directly added in the release medium to mimic complete drug release. At predetermined time points, 2 ml of the release medium were sampled, and an equal volume of fresh release medium was added back. The amount of drug in the media was quantified by reverse-phase HPLC described above. The cumulative release was calculated using the following equation: Cumulative release (%) = $C_t/C_{max} \times 100\%$, where C_t is the

concentration of WGA-TA in the release media and C_{max} is the concentration of WGA-TA when the drug was completely released.

3.3.4 Cell Culture

Human adrenocortical cancer cell lines H295R (high-cortisol secretor) and SW-13 (non-secretor) were obtained from ATCC. RL251 (non-secretor) was derived using clinical protocol approved by the IRB at University of Michigan Hospital and validated by the provider.[31] H295R cells were grown in 1:1 of Dulbecco's modified Eagle medium: nutrient mixture F12 (DMEM: F12, Life Technologies, Grand Island, NY) supplemented with 5% fetal bovine serum, 100 U/mL penicillin, 100 µg/mL streptomycin and 1x ITS (final concentrations 0.001 mg/ml bovine insulin, 0.0055 mg/ml human transferrin and 6.7 ng/ml sodium selenite) (Life Technologies, Grand Island, NY). ACC cell lines SW13, and RL251 were grown in DMEM supplemented with 10% FBS. All cell lines were cultured at 37^{o}C in a humidified incubator with 5% CO_2.

3.3.5 Quantification of SR-B1 expression

The mRNA and protein expression levels of SR-B1 in the ACC cell lines were evaluated by RT-PCR and western blot methods, respectively. For RT-PCR, RNA was isolated from cells grown in culture using RNease kit as per the manufacturer's protocol (Qiagen, Valencia, CA). The mRNA was reverse transcribed and the expression of SR-B1 and the control β-actin was examined with specific primer sets by the standard curve method in Viia7 real time PCR system (Thermo Fisher Scientific, Waltham, MA). For the western blot, cells were lysed using RIPA buffer (50 mM Tris–HCI pH 7.4, 150 mM NaCI, 1% (v/v) NP-40, 0.5% (w/v) sodium deoxycholate, 10 mM sodium fluoride, 1 mM sodium orthovanadate, 1 mM PMSF, 10 mM sodium pyrophosphate, 0.1% (w/v), and SDS supplemented with protease inhibitor solution (EMD Millipore, Billerica, MA). The lysates were centrifuged at 14,000 rpm for 20 minutes and

the proteins were quantified using Protein Assay Reagent (Thermo Scientific, Rockford, IL). Equal amounts of total proteins were separated using SDS-PAGE and then transferred onto a Hybond nitrocellulose membrane (GE Healthcare Life Sciences, Piscataway, NJ). The membranes were blocked using 5% milk and probed over night with appropriate dilutions of the primary antibodies (SR-B1 or actin) for proteins. The blots were then washed three times with PBST and incubated with HRP-conjugated secondary antibodies (1:5000 dilution) from Santa Cruz Biotechnology (Santa Cruz, CA). To ensure equal loading of proteins, actin was used as a control. The bands were visualized using Enhanced chemiluminescence reagent (Thermo Scientific, Rockford, IL). The images were captured on Kodak X-ray film. ImageJ software (NIH) was used for quantification of the western blot.

3.3.6 Cellular uptake of fluorophore-loaded sHDL

The ability of ACC H295R and SW13 cells to recognize sHDL nanodiscs and internalize sHDL's cargo through the SR-B1 receptor was examined after a 2-h incubation of cells with DiO-labeled sHDL. For the confocal microscopy, cells were fixed with 4% paraformaldehyde, permeabilized with 0.1% Triton X-100, and stained with 4', 6-diamidino-2-phenylindole (DAPI). The cellular uptake was then visualized using a Nikon A-1 Spectral Confocal microscope system (Nikon Corporation, Tokyo). Quantification of the cellular fluorescent signal was determined using a flow cytometer (Cyan5) at an excitation wavelength of 488 nm. To investigate whether the uptake of sHDL was mediated by the SR-B1, H295R cells were either pretreated with anti-SR-B1 antibody (NB400-113, Novus biological) at a 1:100 dilution or pre-incubated with 100-fold excess of unlabeled sHDL for 1 h at 37 ºC.

3.3.7 Cytotoxicity of drug-loaded sHDL on adrenal cancer cells

For *in vitro* testing of drug efficacy, H295R was used and the viability was determined by Cell Titer 96 Aqueous non-radioactive Cell proliferation assay. Approximately 8,000 H295R cells/well were seeded in 96- well micro titer plates in 90 μL of growth media and cells were allowed to attach overnight. On the second day, 10 μL serial dilutions of the sHDL nanoparticle, WGA-TA (4,19,27-withalongolide A triacetate) and sHDL-WGA-TA were added to the plates. The cells were then incubated for 72 h at 37^{o}C in a CO_2 humidified chamber. In some experiments H295R cells were pretreated with the SR-B1 antibody (1:100 dilution) or PBS for 1 h before incubation with WGA-TA-sHDL for 24 h. The number of viable cells was determined by measuring the absorbance at a 490 nm wavelength of the dissolved formazan reagent on a BioTek Synergy Neo plate reader (BioTek, Winooski, VT) after the addition of 20 μL of the MTS reagent for 2 h as per the manufacturer's protocol (Promega, Fitchburg, WI). All experiments were carried out in triplicate and the viability of the cells was expressed as the ratio of the number of viable cells with treatment compared to untreated cells. The half-maximal inhibitory concentrations (IC50) were calculated from the MTS assay curves using GraphPad Prism 5 software.

3.3.8 In vivo biodistribution of fluorophore-loaded sHDL in H295R xenografts

Animal experiments were performed in accordance with federal, state, and local guidelines. All work performed on animals was in accordance with and approved by the University Committee on Use and Care of Animals (UCUCA) at University of Michigan, Ann Arbor. When H295R cells reached 60-70% confluence, cells were collected using 0.25% trypsin-0.02% EDTA (Sigma-Aldrich, St. Lewis, MO) and mechanical dissociation, then suspended at 6×10^7 cells/mL in phosphate buffered saline (PBS) and placed on ice. Within 30 minutes, athymic nude

mice (Athymic Nude-*Foxn1*^{nu}, Harlan Laboratories, Indianapolis, IN) were anesthetized with isoflurane, and 6×10^6 cells suspended in 100 µL PBS were injected subcutaneously in the right flank.

For immunohistochemical analysis of SR-BI receptors, tumors were collected when they were ~ 6 mm in diameter and fixed in 10% buffered formalin (Fisher Diagnostics™). Immunohistochemical staining was performed on the Biocare Intellipath Flx in the ULAM IVAC Histology Core at the University of Michigan. Briefly, slides were deparaffinized in xylene, rehydrated through graded alcohols to water then Heat Induced Epitope Retrieval (HIER) was performed in the Decloaking Chamber (Biocare Medical) with Diva, (Biocare Medical). Slides were incubated in Peroxidazed 1 (Biocare Medical) for 5 minutes followed by 30 minutes of incubation in Rodent Block M (Biocare Medical). Rabbit anti-mouse SRB1 (Novus Biologicals) antibody was applied for 30 minutes then SR-B1 was detected with Rabbit on Rodent HRP Polymer (Biocare Medical) for 30 minutes. HRP staining was visualized with DAB (Biocare Medical). Slides were counterstained in Hematoxylin (Biocare Medical), rinsed in deionized water, dehydrated through graded alcohols, cleared in xylene and mounted with Micromount (Lecia Biosystems). Stained slides were imaged with the microscope (PerkinElmer Mantra).

To characterize the biodistribution and tumor-targeting efficacy of the sHDL-WGA-TA nanoparticle *in vivo*, imaging studies were performed in the adrenocortical cancer (H295R) tumor-bearing mice when the tumors were ~6 mm in diameter. DiR (Invitrogen, NY)-labeled sHDL nanoparticles (20 ug/mL DiR) were injected into the tail vein or intraperitoneally at 0.2 mL/dose. At the end of 24 h, animals were sacrificed and organs including the spleen, liver, heart, lung, kidney, brain and tumor were harvested and imaged to characterize biodistribution using a Xenogen IVIS Spectrum Imaging System. [32,33]

3.3.9 Inhibition of tumor growth by WGA-TA sHDL nanodisc in H295R xenografts

The ability of WGA-TA-sHDL nanodiscs to inhibit tumor growth was examined in H295R xenografts in athymic mice. The tumors were implanted as described above, and the treatment was started when tumors reached ~100 mm^3. The mice were randomized into five groups with eight animals per group including: WGA-TA-sHDL (6 mg/kg/day drug, 150 mg/kg/day 22A peptide), WGA-TA (6 mg/kg/day), blank sHDL (150 mg/kg/day 22A peptide), the standard of care Italian protocol (etoposide x 7.5mg/kg/day, doxorubicin x 1.5 mg/kg/day, cisplatin x 2.5 mg/kg/day and mitotane x 300 mg/kg/day) and no-treatment control. Mice were treated with daily intraperitoneal injections for 21 days. Tumor length and width measurements were recorded by digital caliper every 3 days for the duration of treatment. Some mice became moribund during treatment and were euthanized. Average tumor volume was calculated using the formula: tumor volume (mm^3) = $(\pi/6) \times (\text{width})^2 \times \text{length}$.

Following 21 days of treatment, serum was collected for analysis of aspartate transaminase (AST) and alanine transaminase (ALT) levels, which were performed at the In-Vivo Animal Core (IVAC) Animal Diagnostic Laboratory at the University of Michigan. The normal range of AST and ALT was 39.55-386.05 U/L and 24.30-115.25 U/L, respectively. Histologic analysis was performed following 21 days of treatment to evaluate the liver toxicity of different formulations. Signs of chronic inflammation (defined by the presence of lymphocytes and plasma cells), cellular necrosis, and steatohepatitis were assessed in the liver. "Normal" was assigned to specimens with essentially no pathology except for a small degree of inflammation comparable to what is seen physiologically. "Mild, moderate or severe" was assigned to specimens with a less than 10%, 10-50% and greater than 50% increase in inflammatory cells compared to the physiologic state, respectively.

3.3.10 Statistical analysis

Data were analyzed statistically using one-way ANOVA Kruskal-Wallis non-parametric test, and two-way ANOVA for comparisons of 3 or more variables with either Dunn's or Holm-Sidak's multiple comparisons tests, and two-tailed Student's t test for comparisons of two values. P values of <0.05 were considered statistically significant.

3.4 Results and Discussion

3.4.1 Preparation and Characterization of sHDL

The schematic of WGA-TA- and dye-loaded sHDL nanoparticle preparation is shown in **Figure 3.1**. Phospholipids, 22A peptide, and either drug or dye were first dissolved in organic solvent and lyophilized. The resulting powder was hydrated at the temperature above phospholipid melting temperature (T_m) to facilitate nanoparticle assembly and drug incorporation. The 1:2 weight ratio of 22A to phospholipids was used because it is known to result in formation of a homogenous HDL 10-12 nm in diameter.[34] The theoretical loading of WGA-TA was set at 1% (0.3 mg/30 mg peptide-lipid mixture). Following assembly, sHDL-drug nanoparticles were passed through the desalting column (7000 Da) to remove un-incorporated drug and determine WGA-TA encapsulation efficiency (**Table 3.1**).

Due to the limited space available for incorporating drug inside sHDL, molecular interactions between phospholipids and WGA-TA are rather important. The fatty acid chain length and saturation determine T_m and the resulting fluidity of phospholipid bilayer, which is important for incorporation and retention of WGA-TA in sHDL. We used phospholipids of different T_m to prepare WGA-TA-sHDL nanoparticles, including DPPC (T_m = 41°C), SM (T_m = 38°C), DMPC (T_m = 23°C), POPC (T_m = -3°C), and their mixtures.[21] The visual appearance of the resulting

suspension correlated to both the size and quality of the resulting nanoparticles, with clear solutions correlating to the formation of 10-12 nm sHDL particles and cloudy solutions indicating HDL aggregation and drug precipitation. When WGA-TA-sHDL was prepared with DPPC and/or SM, the nanoparticle solutions were clear at 50°C but cloudy at both 37°C and 20°C, indicating drug precipitation at temperatures below T_m. When DMPC (T_m = 23°C) was used to prepare nanoparticles, the drug-loaded sHDL was clear at 50^0C and 37^0C but cloudy at 20^0C. Samples with cloudy solutions showed a loss of drug upon passage through the desalting column and a low encapsulation efficiency of 31-50% (**Table 3.1**).

Lipids with a low transition temperature, such as POPC and DOPC, failed to form sHDL, so they were not used for the preparation of drug-loaded sHDL. However, the mixture of DMPC and POPC resulted in successful loading of WGA-TA into sHDL and clear sHDL solutions at all temperatures tested. For this formulation, drug encapsulation efficiency of 78% was obtained, which corresponded to 0.78% of WGA-TA weight loading. This formulation was selected for additional analytical characterization and was used in cell culture and animal experiments.

3.4.2 Characterization of WGA-TA-sHDL nanoparticles

To examine the purity and size of the WGA-TA-sHDL nanoparticles, blank and drug-loaded sHDL nanoparticles were analyzed by gel permeation chromatography (GPC), dynamic light scattering (DLS), and transmission electron microscopy (TEM). GPC confirmed formation of homogeneous WGA-TA-sHDL distribution without the presence of large nanoparticle aggregates or unbound 22A peptide (**Figure 3.2a**). The DLS measurement showed a narrow size distribution for sHDL and WGA-TA-sHDL of 9.7 ± 0.61 nm and 9.81 ± 0.41 nm, respectively. Consistent with the DLS and GPC data, TEM results also showed that the formulation had

homogeneous discoidal-shaped WGA-TA-sHDL nanoparticles with an average size of ~10 nm (**Figure 3.2b-c**). This size and shape closely resemble the characteristics of endogenous HDL nanoparticles.[15]

To examine drug-release kinetics, WGA-TA-sHDL nanoparticles were placed in a dialysis bag and incubated in sink conditions in 200 mL of PBS containing 0.1% Tween 80 for 24 hours. To compare nanoparticle release with free drug, the same amount of WGA-TA-sHDL was dissolved in 50% DMSO and placed in dialysis bag. The free drug was rapidly released to the media, with almost 100% release within 10 h (**Figure 3.2d**). In contrast, the release of WGA-TA from sHDL was relatively slow, with about 46% released to the media within 10 h, and 65% released within 24 h. These results indicated that the encapsulation of WGA-TA into sHDL significantly alters drug release behavior.

3.4.3 Quantification of SR-B1 on ACC cells

To select ACC cell lines for evaluation of sHDL cellular uptake and WGA-TA-sHDL cytotoxicity, we examined the SR-B1 expression in various ACC cell lines by measuring mRNA levels using RT-PCR and protein levels by western blot analysis (**Figure 3.3**). Actin was used as internal control for RT-PCR, and actin immunoblot confirmed equal loading of the protein per each well. The steroid hormone-synthesizing H295R cells were found to have much higher mRNA and protein expression levels of SR-B1 compared to the other two human ACC cell lines, SW13 and RL251 ($p < 0.0001$), which do not synthesize steroid hormones. Hence, H295R was selected to assess cellular uptake and cytotoxicity of WGA-TA-sHDL.

3.4.4 Cellular uptake of sHDL

To determine if our sHDL is recognized by SR-B1 and capable of delivering its cargo to the target cells efficiently, DiO-loaded sHDLs were incubated with high (H295R) and low (SW13) SR-B1 expressing ACC cell lines for 2 h (**Figure 3.4a-b**). After incubation, the cells were imaged by confocal microscopy and DiO fluorescence in cells was quantified by flow cytometry. It is clear from the image that SR-B1 positive H295R cells effectively internalized DiO-labeled sHDL, in contrast to SW13 cells, which showed limited dye uptake. The addition of anti-SR-B1 antibody or the excess of blank sHDL nanoparticles reduced dye uptake in H295R cells, confirming the involvement of SR-B1 (**Figure 3.4a**). Fluorescence quantification by flow cytometry confirmed visual observations (**Figure 3.4b**). Over 80% of H295R cells showed a positive DiO signal, while fewer than 10% of SW13 cells showed DiO uptake. The pre-incubation of H295R cells with anti-SR-B1 antibody or blank sHDL reduced dye uptake by 2.5-fold and 20%, respectively, confirming the interaction between SR-B1 and sHDL nanodiscs. Based on these results, H295R cells were selected to confirm cytotoxicity and *in vivo* efficacy of WGA-TA-sHDL nanodiscs in ACC.

3.4.5 Cytotoxicity of WGA-TA-loaded sHDL

The cytotoxicity of WGA-TA-loaded sHDL nanodiscs was evaluated by the MTS proliferation assay in the H295R cell line. The cells were treated with varying concentrations of either sHDL, free WGA-TA, or the WGA-TA-loaded sHDL nanodiscs for 72 h, and the viability of the cells was then analyzed (**Figure 3.5a-b**). The results indicate that, compared to either sHDL or WGA-TA alone, WGA-TA-loaded sHDL nanoparticles demonstrated improved cytotoxicity (reduction in cell viability with lower IC50 levels by quantitative curve-fitting using Graph Pad 5.0). The IC_{50} calculated by quantitative curve-fitting using Graph Pad 5.0 was 0.260 ± 0.045 μM for

WGA-TA-sHDL and 0.492 ± 0.115 μM for WGA-TA ($p < 0.05$). The blank sHDL treatment showed some cytotoxicity, likely due to ability of sHDL to efflux cholesterol and inhibit corticosteroid synthesis as we previously reported,[35] but sHDL cytotoxicity was observed at a higher concentration relative to WGA-TA-sHDL (IC50 corresponding to 8.630 ± 1.520 μM WGA-TA ($p < 0.05$) and equivalent to 0.13 ± 0.02 mg/mL of 22A peptide). The presence of SR-B1 antibody significantly decreased the cytotoxicity of WGA-TA-sHDL in H295 cells, with a 2-fold decrease and 4.8-fold decrease of viability for 2.5 μM and 5 μM WGA-TA-sHDL, respectively, indicating the uptake of WGA-TA-sHDL was at least partially mediated by the SR-B1 receptor.

3.4.6 In vivo biodistribution of fluorophore-loaded sHDL

Efficient accumulation throughout individual tumors is important for the targeted delivery of anticancer drugs. In order to test the ability of our sHDL to accumulate in tumor regions efficiently, DiR-loaded sHDL nanodiscs were prepared and administered by either intravenous (IV) or intraperitoneal (IP) routes into athymic mice bearing H295R tumors, which express high levels SR-B1 receptors (**Figure 3.6a**). At 24 h following the injection, biodistribution of DiR-sHDL was examined by imaging individual organs (**Figure 3.6b-c**). The imaging clearly demonstrated that tumors harvested 24 h after either IV or IP injection had efficient accumulation of sHDL cargo DiR, providing direct evidence for *in vivo* ACC targeting with sHDL. As expected, strong fluorescent signals from the liver were observed, which is supported given that the liver is the major organ for elimination of nanoparticles. The accumulation of the sHDL nanodiscs in other organs was significantly less compared to that in either the liver or tumor. Since IV and IP injection showed similar distribution profiles of sHDL-DiR ($p > 0.05$),

for the therapeutic efficacy study in H295R xenografts, WGA-TA-sHDL was administered by the IP route.

3.4.7 Tumor growth inhibition in vivo

The ability of WGA-TA-sHDL nanodiscs to inhibit growth of ACC *in vivo* was tested in H295R xenografts, which exhibit high levels of SR-B1 expression in tumors (Supplementary Figure 1). Once the tumor volume reached ~100 mm^3, the tumor-bearing mice were randomly assigned to one of the five treatment groups. The control group received no treatment, while the other groups received either blank sHDL, free WGA-TA, WGA-TA-sHDL, or standard of care treatment Italian protocol (etoposide, doxorubicin, cisplatin and mitotane) by IP administration daily for 21 days. Following the start of treatment, the tumor volumes were assessed every three days, which are shown in **Figure 3.7**. H295R is a very aggressive and rapidly growing tumor with high animal-to-animal variability and rapid growth kinetics, making this tumor very difficult to cure. The results from the study, however, showed significant differences in tumor volume between the no-treatment control and WGA-TA-sHDL group at the end of treatment ($p < 0.01$). No statistical differences between other groups were observed. Importantly, we didn't see any significant change to the serum ALT and AST levels, as both were in the normal range for all treated groups following 21-day treatment (**Figure 3.7b**). Moreover, livers from all the experimental groups were shown to be normal (**Figure 3.7c**). Although both mice treated with free WGA-TA and WGA-TA-HDL had lower body weights than other groups, it should be noted that part of the body weight decrease for WGA-TA-HDL can be ascribed to the tumor volume decrease following treatment. Compared to the free drug-treated animals that had much larger tumors and lower body weights, the WGA-TA-sHDL treatment decreased the side effects of WGA-TA *in vivo* (**Figure 3.8**).

3.5 Conclusion

In summary, we have optimized the composition of sHDL for delivery of a novel lipophilic natural product, withalongolide A (WGA)-4,19,27-triacetate (WGA-TA). When WGA-TA was loaded into sHDL, this formulation was shown to kill the SR-B1-expressing H295R cancer cells more efficiently than free drug alone *in vitro*. In addition, sHDL cargo molecules could accumulate in tumor regions of ACC *in vivo,* and the WGA-TA-sHDL formulation was more effective in halting the growth of ACC tumors than the standard-of-care Italian protocol. Taken together, sHDL delivery could represent a more useful drug-delivery platform for hydrophobic chemotherapeutics in tumors such as ACC that overexpress SR-B1 and should be further evaluated for potential clinical application. Additionally, this unique drug-delivery strategy could be applied for the delivery of hormones, steroids, and other therapeutics agents in treating other adrenal diseases. [36]

3.6 Figures

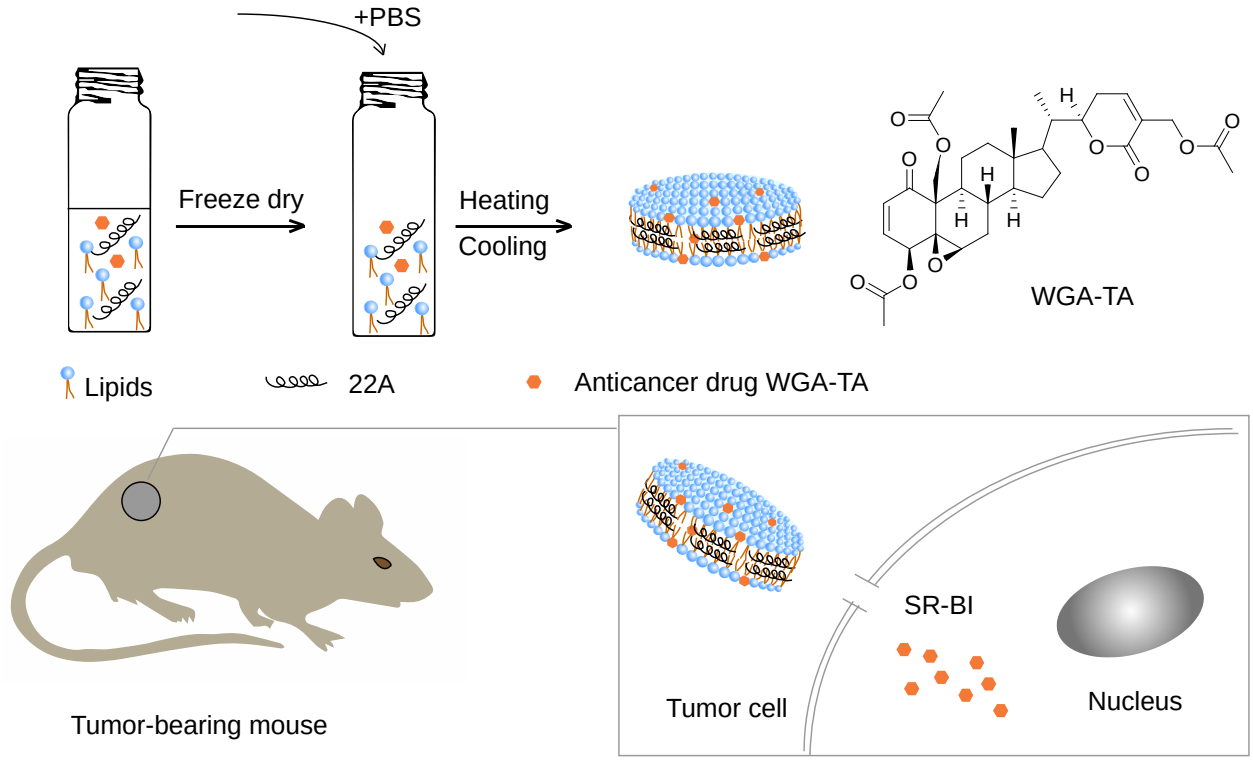

Figure 3.1. Schematic for the preparation of WGA-TA-sHDL and SR-B1-mediated uptake of sHDL cargo.

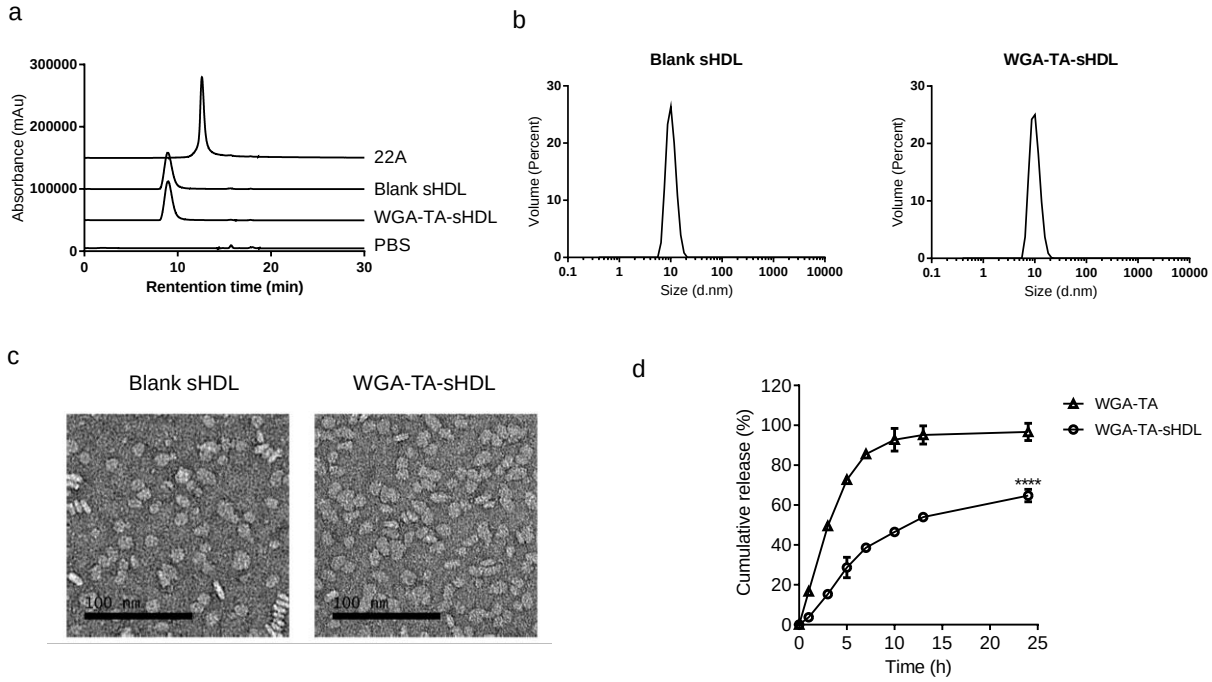

Figure 3.2. Characterization of blank sHDL and WGA-TA-sHDL. a, gel permeation chromatography (GPC) of indicated formulations; b, dynamic light scattering (DLS), and c, transmission electron microscopy (TEM) of blank sHDL and WGA-TA-sHDL; d, WGA-TA release from sHDL nanodiscs compared with a solution of free drug in PBS containing 0.1% Tween 80 at 37 ºC.

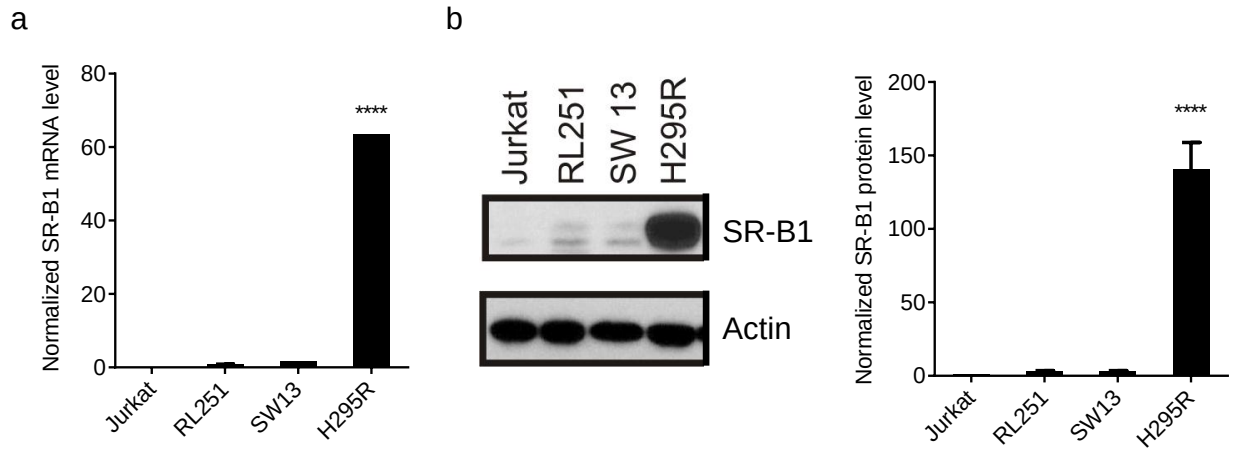

Figure 3.3. SR-B1 expression in different cell lines. SR-B1 levels in ACC cell lines were analyzed by RT PCR (a) and western blot (b). Asterisks represent the significant difference between H295R cells and all other groups.

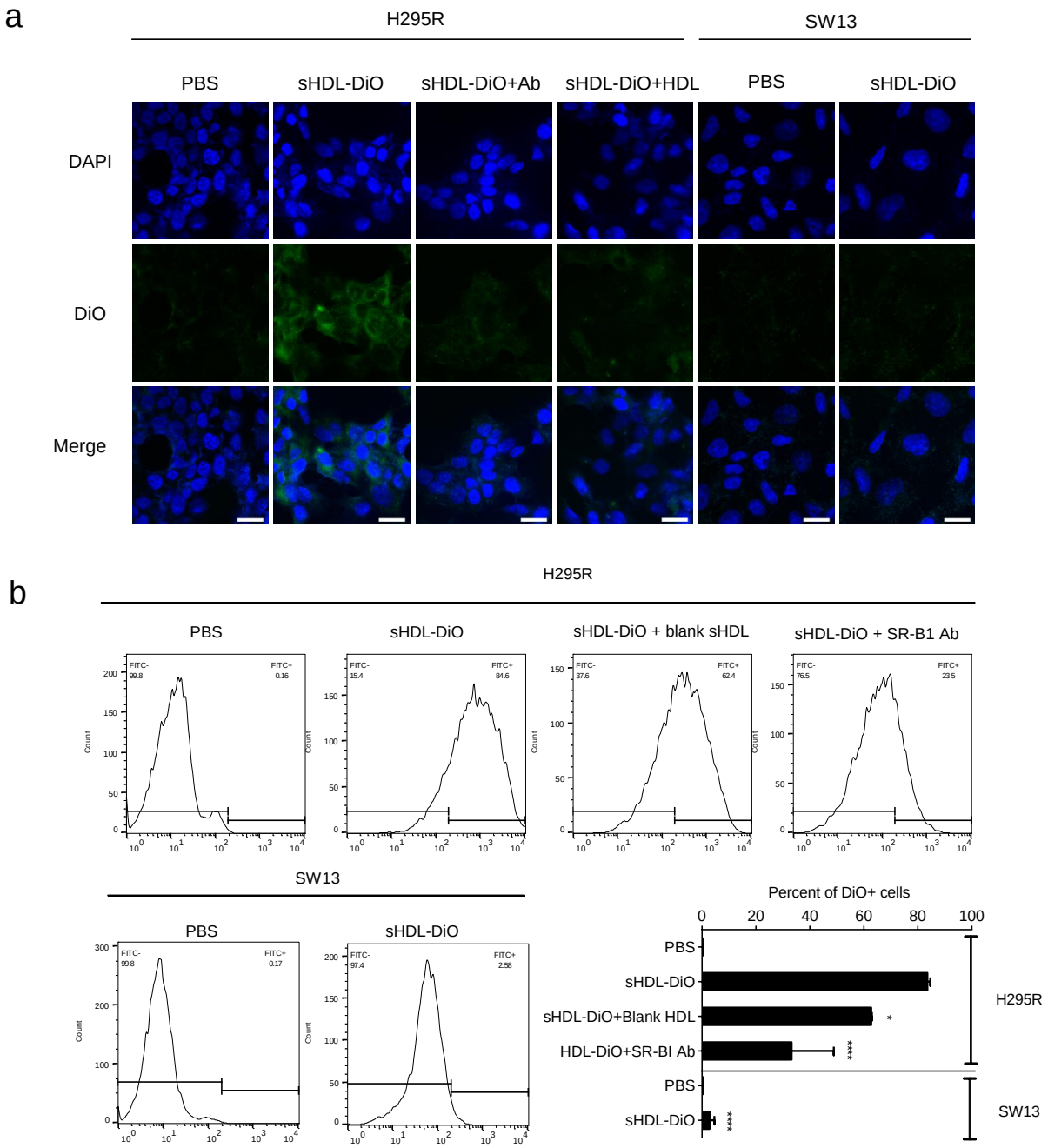

Figure 3.4. Cellular uptake of DiO-sHDL by different cell lines. (a) Confocal microscopy images and (b) flow cytometry of H295R cells and SW13 cells following incubation with indicated formulations for 2 h at 37 ºC. * $p < 0.05$, and **** $p < 0.0001$. Asterisks in (b) represent the significant difference between H295R cells and indicated groups.

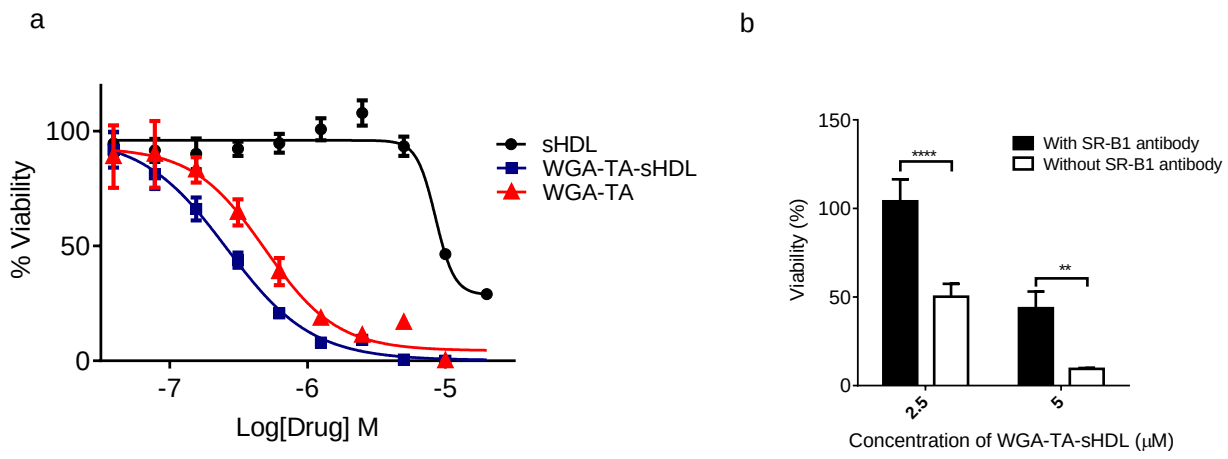

Figure 3.5. Cytotoxicity of free WGA-TA, WGA-TA-sHDL and blank sHDL on H295R cells. (a) H295R cells were incubated with indicated formulations for 72 h at 37 ºC and the viability was determined by Cell Titer 96 Aqueous non-radioactive Cell proliferation assay. (b) H295R cells were pretreated with the SR-B1 antibody (1:100 dilution) or PBS for 1 h before incubation with indicated concentrations of WGA-TA-sHDL for 24 h. The viability was measured using the same method as described in (a).

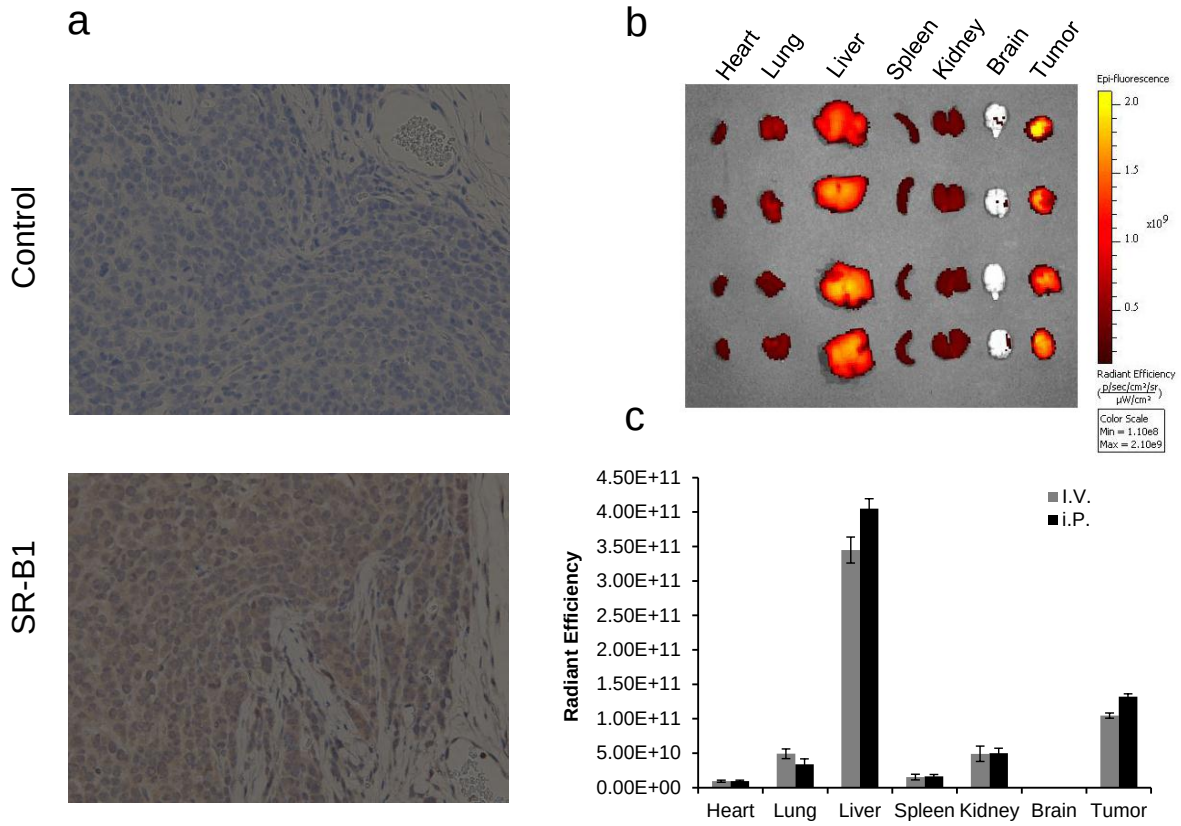

Figure 3.6. Biodistribution of DiR-sHDL in H295 tumor-bearing mice. (a) Immunohistochemical (IHC) staining of SR-B1 in H295R tumors. Immunohistochemical staining was performed on the Biocare Intellipath Flx in the ULAM IVAC Histology Core at the University of Michigan by using rabbit anti-mouse SRB1(rabbit polyclonal; Novus Biologicals) revealed with rabbit horseradish peroxidase. Shown are the representative IHC staining of slides of H295 tumors without using anti-mouse SRB1 (control) or with anti-mouse SRB1. (b) DiR-sHDL was injected either intravenously or intraperitoneally in H295 tumor-bearing mice and major organs were harvested and imaged 24 h after injection. (c) Quantification of fluorescence for organs in (b).

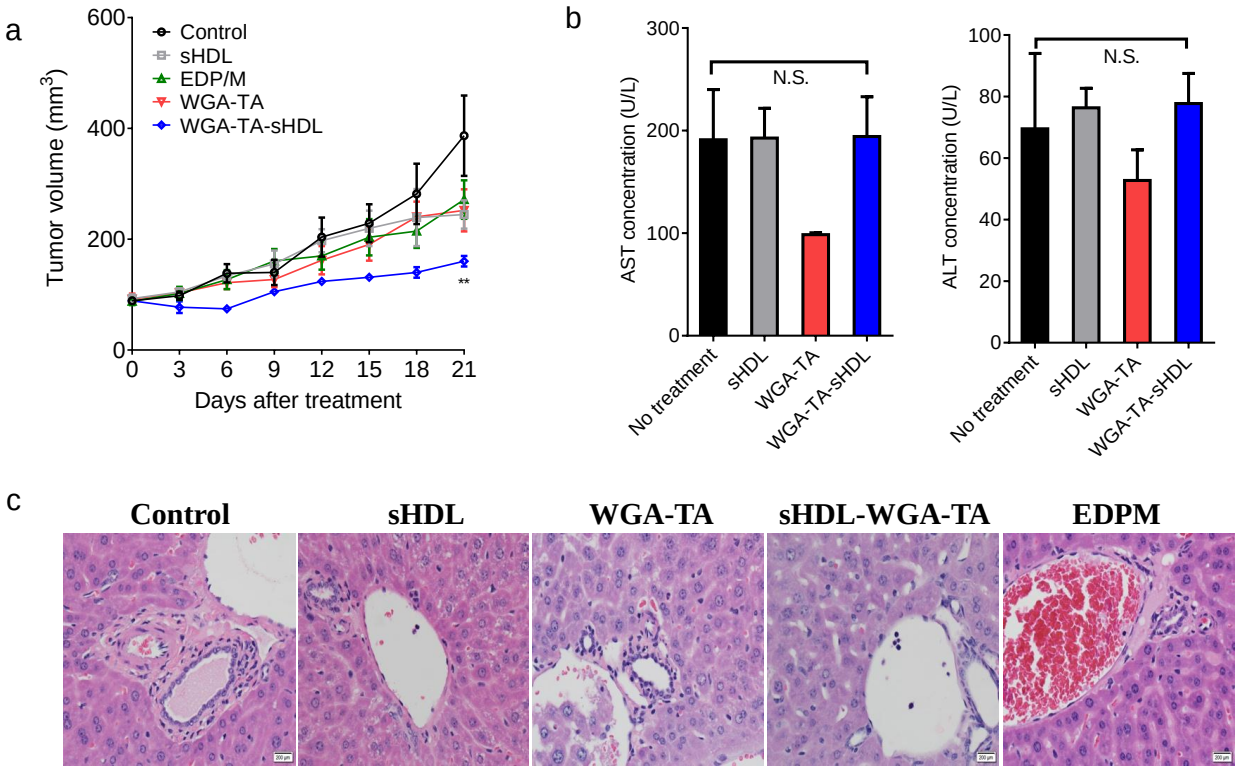

Figure 3.7. In vivo therapeutic effect of WGA-TA-sHDL. H295 tumor-bearing mice were treated with indicated formulations daily for 21 days after the tumor volume reached ~100 mm3. Shown are (a) the average tumor growth curves; (b) serum ALT and AST levels for indicated formulations, and (c) H&E staining of livers for indicated formulations following 21 days of treatment. ** $p < 0.01$.

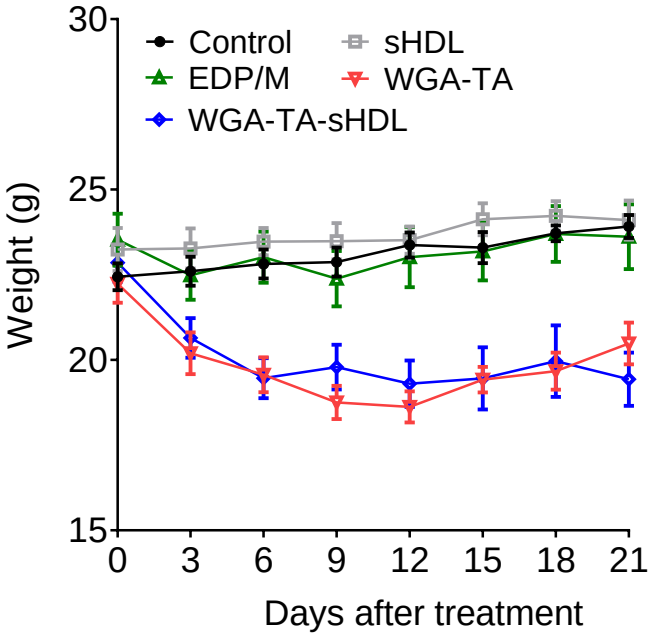

Figure 3.8. Body weights of animals treated with indicated formulations. Data represent mean ± SEM (n=4-6).

Table 3.1. Characterization of WGA-TA-sHDLs with different compositions.

Lipid composition	DPPC (mg)	SM (mg)	DMPC (mg)	POPC (mg)	22A (mg)	WGA-TA	EE %
DPPC	20	0	0	0	10	0.3	45%
SM	0	20	0	0	10	0.3	45%
DMPC	0	0	20	0	10	0.3	31%
DPPC/SM	10	10	0	0	10	0.3	50%
DMPC/POPC	0	0	10	10	10	0.3	78%

3.7 References

1. Libe R. Adrenocortical carcinoma (ACC): diagnosis, prognosis, and treatment. *Front Cell Dev Biol.* 2015;3:45.

2. Dy BM, Wise KB, Richards ML, et al. Operative intervention for recurrent adrenocortical cancer. *Surgery.* Dec 2013;154(6):1292-1299.

3. Else T, Kim AC, Sabolch A, et al. Adrenocortical carcinoma. *Endocr Rev.* Apr 2014;35(2):282-326.

4. Subramanian C, Zhang H, Gallagher R, Hammer G, Timmermann B, Cohen M. Withanolides are potent novel targeted therapeutic agents against adrenocortical carcinomas. *World J Surg.* Jun 2014;38(6):1343-1352.

5. White PT, Subramanian C, Motiwala HF, Cohen MS. Natural Withanolides in the treatment of chronic diseases. *Adv Exp Med Biol.* 2016;928:329-373.

6. Miller WL, Auchus RJ. The molecular biology, biochemistry, and physiology of human steroidogenesis and its disorders. *Endocr Rev.* Feb 2011;32(1):81-151.

7. Lerario AM, Moraitis A, Hammer GD. Genetics and epigenetics of adrenocortical tumors. *Mol Cell Endocrinol.* Apr 05 2014;386(1-2):67-84.

8. Rainey WE, Bird IM, Mason JI. The NCI-H295 cell line: a pluripotent model for human adrenocortical studies. *Mol Cell Endocrinol.* Apr 1994;100(1-2):45-50.

9. Leibovitz A, McCombs WM, 3rd, Johnston D, McCoy CE, Stinson JC. New human cancer cell culture lines. I. SW-13, small-cell carcinoma of the adrenal cortex. *J Natl Cancer Inst.* Aug 1973;51(2):691-697.

10. Leon CG, Locke JA, Adomat HH, et al. Alterations in cholesterol regulation contribute to the production of intratumoral androgens during progression to castration-resistant prostate cancer in a mouse xenograft model. *Prostate.* Mar 01 2010;70(4):390-400.

11. Pussinen PJ, Karten B, Wintersperger A, et al. The human breast carcinoma cell line HBL-100 acquires exogenous cholesterol from high-density lipoprotein via CLA-1 (CD-36 and LIMPII analogous 1)-mediated selective cholesteryl ester uptake. *Biochem J.* Jul 15 2000;349(Pt 2):559-566.

12. Imachi H, Murao K, Sayo Y, et al. Evidence for a potential role for HDL as an important source of cholesterol in human adrenocortical tumors via the CLA-1 pathway. *Endocr J.* Feb 1999;46(1):27-34.

13. Nofer JR, Kehrel B, Fobker M, Levkau B, Assmann G, von Eckardstein A. HDL and arteriosclerosis: beyond reverse cholesterol transport. *Atherosclerosis.* Mar 2002;161(1):1-16.

14. Vickers KC, Palmisano BT, Shoucri BM, Shamburek RD, Remaley AT. MicroRNAs are transported in plasma and delivered to recipient cells by high-density lipoproteins. *Nat Cell Biol.* Apr 2011;13(4):423-433.

15. Kuai R, Li D, Chen YE, Moon JJ, Schwendeman A. High-Density Lipoproteins: Nature's Multifunctional Nanoparticles. *ACS nano.* Mar 22 2016;10(3):3015-3041.

16. Duivenvoorden R, Tang J, Cormode DP, et al. A statin-loaded reconstituted high-density lipoprotein nanoparticle inhibits atherosclerotic plaque inflammation. *Nat Commun.* 2014;5:3065.

17. Zhang XB, Chen BS. Recombinant High Density Lipoprotein Reconstituted with Apolipoprotein AI Cysteine Mutants as Delivery Vehicles for 10-Hydroxycamptothecin. *Cancer Lett.* Dec 1 2010;298(1):26-33.

18. Mooberry LK, Nair M, Paranjape S, McConathy WJ, Lacko AG. Receptor Mediated Uptake of Paclitaxel from a Synthetic High Density Lipoprotein Nanocarrier. *J Drug Target.* Jan 2010;18(1):53-58.

19. Bricarello DA, Smilowitz JT, Zivkovic AM, German JB, Parikh AN. Reconstituted Lipoprotein: A Versatile Class of Biologically-Inspired Nanostructures. *Acs Nano.* Jan 2011;5(1):42-57.

20. Cao W, Ng KK, Corbin I, et al. Synthesis and evaluation of a stable bacteriochlorophyll-analog and its incorporation into high-density lipoprotein nanoparticles for tumor imaging. *Bioconjug Chem.* Nov 2009;20(11):2023-2031.

21. Yuan Y, Wen J, Tang J, et al. Synthetic high-density lipoproteins for delivery of 10-hydroxycamptothecin. *Int J Nanomedicine.* 2016;11:6229-6238.

22. Tang J, Kuai R, Yuan W, Drake L, Moon J, A S. Effect of size and pegylation of liposomes and peptide-based synthetic lipoproteins on tumor targeting. *Nanomedicine.*In press.

23. Subramanian C, Kuai R, Zhu Q, et al. Synthetic High-Density Lipoprotein Nanoparticles: A Novel Therapeutic Strategy for Adrenocortical Carcinomas. *Surgery.* Jan 2016;159(1):284-295.

24. Di Bartolo BA, Nicholls SJ, Bao S, et al. The Apolipoprotein A-I Mimetic Peptide ETC-642 Exhibits Anti-Inflammatory Properties That Are Comparable to High Density Lipoproteins. *Atherosclerosis.* Aug 2011;217(2):395-400.

25. Miles J, et al. . Single-dose tolerability, pharmacokinetics, and cholesterol mobilization in HDL-C fraction following intravenous administration of ETC-642, a 22-mer ApoA-I

analogue and phospholipids complex, in atherosclerosis patients. *Proceedings of Arteriosclerosis Thrombosis and Vascular Biology* 2004;24:E19-E19.

26. Li D, Gordon S, Schwendeman A, Remaley AT. Apolipoprotein mimetic peptides for stimulating cholesterol efflux. *Apolipoprotein Mimetics in the Management of Human Disease.* 2015:29-42.

27. Zhang WL, Gu X, Bai H, Yang RH, Dong CD, Liu JP. Nanostructured lipid carriers constituted from high-density lipoprotein components for delivery of a lipophilic cardiovascular drug. *Int J Pharm.* May 31 2010;391(1-2):313-321.

28. Subramanian C, Kuai R, Zhu Q, et al. Synthetic high-density lipoprotein nanoparticles: A novel therapeutic strategy for adrenocortical carcinomas. *Surgery.* Jan 2016;159(1):284-294.

29. Yang T, Choi MK, Cui FD, et al. Preparation and evaluation of paclitaxel-loaded PEGylated immunoliposome. *J Control Release.* Jul 31 2007;120(3):169-177.

30. Zhang W, He H, Liu J, et al. Pharmacokinetics and atherosclerotic lesions targeting effects of tanshinone IIA discoidal and spherical biomimetic high density lipoproteins. *Biomaterials.* Jan 2013;34(1):306-319.

31. Schteingart DE, Giordano TJ, Benitez RS, et al. Overexpression of CXC chemokines by an adrenocortical carcinoma: a novel clinical syndrome. *J Clin Endocrinol Metab.* Aug 2001;86(8):3968-3974.

32. Kuai R, Yuan W, Li W, et al. Targeted delivery of cargoes into a murine solid tumor by a cell-penetrating peptide and cleavable poly(ethylene glycol) comodified liposomal delivery system via systemic administration. *Mol Pharm.* Dec 5 2011;8(6):2151-2161.

33. Yuan W, Kuai R, Ran R, et al. Increased delivery of doxorubicin into tumor cells using extracellularly activated TAT functionalized liposomes: in vitro and in vivo study. *J Biomed Nanotechnol.* Aug 2014;10(8):1563-1573.

34. Tang J, Li D, Drake L, et al. Influence of route of administration and lipidation of apolipoprotein A-I peptide on pharmacokinetics and cholesterol mobilization. *J Lipid Res.* Jan 2017;58(1):124-136.

35. Taylor MJ, Sanjanwala AR, Morin EE, et al. Synthetic high-density lipoprotein (sHDL) inhibits steroid production in HAC15 adrenal cells. *Endocrinology.* Aug 2016;157(8):3122-3129.

36. Kuai R, Subramanian C, White PT, et al. Synthetic high-density lipoprotein nanodisks for targeted withalongolide delivery to adrenocortical carcinoma. *Int J Nanomed.* 2017;12:6581-6594.

Chapter 4 Elimination of Established Tumors with Nanodisc-Based Combination Chemoimmunotherapy

4.1 Abstract

Although immune checkpoint blockade has shown initial success for various cancers, only a small subset of patients benefits from this therapy. Some chemotherapeutic drugs have been reported to induce antitumor T cell responses, prompting a number of clinical trials on combination chemoimmunotherapy. However, it remains unclear how to achieve potent immune activation with traditional chemotherapeutics in a manner that is safe, effective, and compatible with immunotherapy. Here we show that high-density lipoprotein (HDL)-mimicking nanodiscs loaded with doxorubicin (DOX), a widely used chemotherapeutic agent, can potentiate immune checkpoint blockade in murine tumor models. Delivery of DOX via nanodiscs triggered immunogenic cell death of cancer cells and exerted antitumor efficacy without any overt off-target side effects. Importantly, "priming" tumors with DOX-carrying nanodiscs elicited robust antitumor CD8+ T cell responses while broadening their epitope recognition to tumor-associated antigens, neoantigens, as well as intact whole tumor cells. Combination chemoimmunotherapy with nanodiscs plus anti-PD-1 therapy induced complete regression of established CT26 and MC38 colon carcinoma tumors in 80-88% of animals and protected survivors against tumor recurrence. Our work provides a new, generalizable framework for utilizing nanoparticle-based chemotherapy to initiate antitumor immunity and sensitize tumors to immune checkpoint blockade.

4.2 Introduction

Cancer immunotherapy aims to harness the host's own immune system to fight against cancer, and immune checkpoint blockers (ICBs) have shown striking initial success in the past few years, as exemplified by the clinical success of anti-CTLA-4 (αCTLA-4), anti-PD-1 (αPD-1), and recently FDA-approved anti-PD-L1 antibodies[1-4]. However, despite their potential, ICBs currently benefit only a subset of patients, generally with 10 - 40% response rates reported in the clinic[2,5]. As their therapeutic efficacy depends largely on licensing pre-existing antitumor T cells to kill their target tumor cells, the majority of patients bearing "cold" tumors with a low number of tumor antigen-specific T cells respond poorly to ICBs[6,7]. Hence, there has been considerable interest to develop complementary approaches, including therapeutic vaccines[8-10], radiation therapy[11-13], and chemotherapy[14-16], which could increase the repertoire and abundance of antitumor T cells so that combination immunotherapy with ICBs might exert strong antitumor immunity against cancer cells.

Notably, recent studies have shown that certain chemotherapeutic drugs, such as doxorubicin (DOX), may contribute to antitumor T cell responses by inducing a special form of tumor-cell killing, known as immunogenic cell death (ICD)[17-22]. Tumor cells undergoing ICD upregulate "eat me" and "danger" signals. The "eat me" signals, such as calreticulin (CRT) exposed on the surfaces of immunogenically dying tumor cells, enable dendritic cells (DCs) to phagocytose those tumor cells and present tumor antigen epitopes in the context of major histocompatibility complex (MHC) class I or II[18,22]. In turn, the "danger" signals, such as high-mobility group box 1 (HMGB1) released by immunogenically dying tumor cells, promote activation of DCs and trigger antigen-specific T cell responses[17,21,23]. Thus, the use of ICD-inducing chemotherapeutic

agents may offer a convenient and universal strategy for killing cancer cells, while simultaneously eliciting broad antitumor T cell responses.

Importantly, recent studies have shown promising pre-clinical results reporting antitumor immune responses induced by free DOX treatment either as a monotherapy or combined with immunotherapy[14,24-26]. Such findings have led to multiple ongoing clinical trials in phases I, II, and III that aim to investigate DOX therapy combined with ICBs[27-30]. While results these clinical trials are yet to be reported, it remains to be seen how to achieve an optimal therapeutic outcome with chemoimmunotherapy, especially since there are concerns of inadequate circulation half-life and limited intratumoral accumulation of DOX as well as its off-target toxicities, including its widely-documented cardiotoxicity[31], which may exacerbate toxicities of ICBs[32].

To address these challenges, here we have sought to develop a general strategy for improving the delivery of chemotherapeutics in a way that is safe, effective, and compatible with immune activation for combination immunotherapy. We have chosen to work with DOX since it is a widely-used anti-cancer therapeutic agent and has ICD-inducing properties[18,21,22,33]. Delivery of DOX via nano-systems has been investigated intensively with a wide range of biomaterials, including liposomes, synthetic polymers, micelles, and inorganic nanostructures, in various stages of development[34-38]. However, it is not yet clear how to apply these drug delivery systems to achieve immune activation in a manner compatible with cancer immunotherapy, while, at the same time, addressing the long-standing issues of industrial scale-up and clinical safety associated with various classes of nanomedicine.

In this study, we have developed synthetic high density lipoprotein-like nanodiscs (sHDL), composed of an apolipoprotein A1 (ApoA1)-mimetic peptide and phospholipids, for stimuli-

responsive delivery of chemotherapy and demonstrated their potency for combination chemoimmunotherapy *in vivo* (**Figure 4.1**). In particular, in recent clinical trials for cardiovascular applications, sHDL platform has been successfully scaled up and demonstrated to be safe[39-41], thus prompting us to evaluate sHDL as the delivery platform for chemoimmunotherapy. In that effort, we have achieved efficient loading of DOX in sHDL and its pH-dependent release in endosomes/lysosomes of tumor cells. Treatment with sHDL covalently attached with DOX (sHDL-DOX) induced ICD of tumor cells, improved pharmacokinetic profiles and tumor targeting of DOX, and exhibited significant antitumor efficacy without causing any overt off-target side effects. Tumor-bearing mice treated with sHDL-DOX elicited robust T cell responses directed against live tumor cells, tumor-associated antigens as well as neoantigens, which are a class of patient-specific mutant epitopes encoded by somatic mutations in cancerous cells[42] and shown to dictate patient responses to immune checkpoint blockade[43-45]. Importantly, we report that sHDL-DOX markedly potentiated antitumor T cell responses and therapeutic efficacy of αPD-1 immunotherapy, leading to elimination of established CT26 and MC38 tumors in 80-88% of mice and long-term immunity against tumor cell re-challenge. Overall, these results demonstrated a generalizable strategy for inducing robust antitumor immunity with nanoparticle-based chemotherapy that can sensitize tumors to immune checkpoint blockade.

4.3 Materials and methods

4.3.1 Materials

1,2-dipalmitoyl-sn-glycero-3-phosphocholine (DPPC) was Nippon Oils and Fats (Osaka, Japan). 1,2-dipalmitoyl-*sn*-glycero-3-phosphothioethanol (PTD) was purchased from Avanti Polar Lipids (Alabaster, AL). DWLKAFYDKVAEKLKEAFPDWAKAAYDKAAEKAKEAA (37A)

was from GenScript Corp. (Piscataway, NJ). Anti-mouse CD16/32 was from eBioscience (San Diego, CA). Anti-mouse CD8α-APC, IFN-γ-PE, and CD11c-PECy7 were from BD Bioscience (San Jose, CA). Anti-mouse PD-1 (RMP1-14) was purchased from BioXcell (West Lebanon, NH). CT26 cells were from the American Type Culture Collection (ATCC). MC-38 cells were from Dr. Weiping Zou (University of Michigan, Ann Arbor, MI).

4.3.2 Preparation and characterization of sHDL-DOX

sHDL was prepared by using the lyophilization method that we have previously developed[41,46,47]. Briefly, 1,2-dipalmitoyl-sn-glycero-3-phosphocholine (DPPC) and an ApoA1-mimetic peptide DWLKAFYDKVAEKLKEAFPDWAKAAYDKAAEKAKEAA (37A) were mixed at 1.5:1 weight ratio in acetic acid, followed by lyophilization. The lyophilized powder was hydrated in PBS (pH 7.4) and cycled between 55 ^{0}C and room temperature to obtain sHDL. We synthesized a pH-sensitive lipid-DOX conjugate for efficient loading and pH-triggered release of DOX from sHDL. Briefly, DOX was activated with N-β-maleimidopropionic acid hydrazide (BMPH, Thermo Fisher) in anhydrous methanol containing TFA[34]. The mixture was allowed to react for 24 h at room temperature, followed by rotary evaporation. Activated DOX was then reacted with 1,2-dipalmitoyl-*sn*-glycero-3-phosphothioethanol (PTD) in chloroform containing 10% triethylamine for 24 h in the dark. After rotary evaporation, the resulting lipid-DOX conjugate was kept at -20 ^{0}C until further use. The molecular weight of the conjugate was confirmed by electrospray ionization (ESI) mass spectrometry. To load DOX in sHDL, the lipid-DOX conjugate was dissolved in DMSO and then incubated with pre-formed sHDL suspension in PBS (pH 7.4) for 5 min at 37 ^{0}C on an orbital shaker. The resulting sHDL-DOX was passed through a desalting column (Pierce) to remove any unincorporated DOX.

The concentration of DOX loaded in sHDL-DOX was measured by a fluorescence-based method. Ten μL of sHDL-DOX diluted in water was incubated with 240 μL of 1% Triton X-100 solution for 30 min at RT in the dark, and the fluorescence signal from DOX was detected using a microplate reader with Ex = 470 nm and Em = 590 nm. Homogeneity of sHDL-DOX was analyzed by gel permeation chromatography (GPC) using a Shimadzu HPLC system equipped with a TSKgel G2000SWxl column (7.8 mm ID × 30 cm, Tosoh Bioscience LLC) and the detection wavelengths were set at 220 nm and 485 nm for quantification of ApoA-I mimetic peptide 37A and DOX, respectively. The particle size of sHDL-DOX was measured by dynamic light scattering (DLS) on a Malvern Zetasizer (Westborough, MA). The sHDL morphology was assessed by transmission electron microscopy (TEM) after proper dilution of the original samples. Then, 3 μL of the diluted sample solution was deposited on a carbon film-coated 400 mesh copper grid (Electron Microscopy Sciences) and dried for 1 minute. Samples were then negatively stained with 1% (w/v) uranyl formate, and the grid was dried before TEM observation. All specimens were imaged on a 100kV Morgagni TEM equipped with a Gatan Orius CCD.

4.3.3 Intracellular delivery and cytotoxicity of sHDL-DOX

To examine sHDL-DOX for its pattern of intracellular delivery, 100,000 CT26 tumor cells were seeded in 35 mm Petri dishes (MatTek Corp., Ashland, MA) and cultured overnight. Cells were incubated with 40 μM sHDL-DOX or free DOX for predetermined durations (10 min, 10 h, and 24 h). After incubation, cells were washed with PBS, fixed with 4% paraformaldehyde, and stained with DAPI before imaging with a confocal microscope (Nikon A1). Cytotoxicity of sHDL-DOX was measured using a cell counting kit-8 (CCK8, Dojindo Molecular Technologies) following the manufacturer's instructions.

4.3.4 Immunogenic cell death in tumor cells treated with sHDL-DOX

Markers of immunogenic cell death, such as calreticulin (CRT) and HMGB1, were analyzed following published reports[17,18]. Briefly, 100,000 CT26 cells were seeded on 35 mm Petri dishes (MatTek Corp., Ashland, MA) pre-coated with polylysine. After overnight incubation, cells were treated with 50 μM DOX or sHDL-DOX for 24 h, washed twice with FACS buffer (1% BSA in PBS) followed by incubation with CD16/32 for 10 min and rabbit anti-mouse CRT Ab (1:100 dilution) for 30 min. Cells were washed and then incubated with Hoechst 33342 and anti-rabbit Ab labeled with APC for 20 min and then observed under a confocal microscope. To measure the release of HMGB1 from dying tumor cells, 50,000 CT26 cells seeded in 96-well plates were incubated with 50 μM DOX or sHDL-DOX for 72 h. After incubation, each supernatant was collected and centrifuged at 1,000 g for 20 min before HMGB1 measurement using a mouse HMGB1 ELISA kit (LifeSpan BioSciences, Inc).

4.3.5 Biodistribution and pharmacokinetic studies *in vivo*

sHDL was loaded with a near-infrared fluorescent dye, DiR, for the biodistribution study[48]. Briefly, DiR (0.1 mol %) was mixed with DPPC and 37A in acetic acid, followed by lyophilization and hydration in PBS to form sHDL-DiR as described above. BALB/c mice inoculated with 200,000 CT26 tumor cells were injected intravenously with sHDL-DiR (20 μg/mL DiR) on day 10. At predetermined time points post-injection, whole body imaging was performed using the IVIS optical imaging system. At the 72 h time point, the tumor-bearing mice were euthanized and major organs (brain, heart, liver, spleen, lung, kidney, and tumor) were harvested for *ex vivo* imaging. For the pharmacokinetic analysis, mice were administered with 4 mg/kg DOX or sHDL-DOX IV. Following drug treatment, at each time point (15 min, 1 h, 3 h, 7 h, and 24 h), 50 μL of blood was collected in Microvette® 500 Z-gel tubes by submandibular

bleeding and kept on ice. The samples were centrifuged at 10,000 g for 5 min at RT, and 10 μL of the serum was added with 10 μL of PBS and incubated with 480 μL of acidified isopropanol (75 mM HCl, 10% water, 90% isopropanol) overnight at 4 ^{0}C in the dark to extract DOX. The isopropanol extract was centrifuged at 14,000 rpm for 10 min, and 125 μL of the supernatant was used for fluorescence detection of DOX on a microplate reader with Ex = 485 and Em = 590 nm. The standard curve was generated with DOX spiked in normal serum and measured following the same protocol. Dox serum concentration vs time curves were fitted with a two-compartment model by GraphPad Prism 6 to determine the AUC values[49].

4.3.6 Therapeutic study in tumor-bearing animals

Mice were cared for following federal, state, and local guidelines. All work performed on animals was in accordance with and approved by University Committee on Use and Care of Animals (UCUCA) at University of Michigan, Ann Arbor. For treatment studies involving animals injected with CT26 cells, BALB/c mice were inoculated with 2×10^5 CT26 cells per mouse on the right flank by subcutaneous injection on day 0 and intravenously injected with 4 mg/kg DOX in sHDL or free soluble form on days 8, 11, and 14. For the combinatorial chemoimmunotherapy, anti-mouse PD-1 (100 μg/mouse) was administered intraperitoneally on days 9, 12 and 15 in addition to the i.v. injection of DOX-containing formulations. For MC38 studies, C57BL/6 mice were inoculated subcutaneously with 2×10^5 MC38 cells on day 0 and intravenously injected with 4 mg/kg DOX in sHDL or free soluble form on days 8 and 11 with or without intraperitoneal administration of anti-mouse PD-1 (100 μg/mouse) on days 9 and 12. Tumor growth was monitored every other day, and the tumor volume was calculated by the following equation: tumor volume = length × width^2 × 0.52. When individual tumor masses reached 15 mm in diameter or when animals became moribund with severe weight loss or active

ulceration, animals were euthanized. On day 20, some CT26 tumor-bearing mice were euthanized and the hearts and livers were collected and fixed in 10% Buffered Formalin (Fisher Diagnostics™). A series of 5-μm sections were stained with hematoxylin and eosin (H&E). Stained slides were then observed microscopy (PerkinElmer Mantra). On day 60, mice cured of primary CT26 or MC38 tumors were re-challenged by subcutaneous injection of 2×10^5 of the same tumor cells, and subsequent tumor growth was monitored as described above. Alternatively, some mice, cured of primary CT26 or MC38 tumors, were re-challenged by intravenous injection of 2×10^5 the same tumor cells and the lung metastasis of CT26 or MC38 tumor cells was visualized by injecting India ink (1:10 dilution in PBS) into the lungs via the trachea and fixing the lungs in Fetek's solution[50]. Naïve mice were used as controls and re-challenged in the same way.

For a subset of studies, tumor tissues and tumor-draining lymph nodes (TDLNs) harvested on indicated time points were cut into small pieces of 2-4 mm and cells were dissociated in digestion buffer [collagenase type IV (1 mg/mL) and DNase I (100 U/mL) in serum-free RPMI] for 20~30 min at 37 ^{0}C with gentle shaking[10]. This cell suspension was passed through a 70-μm nylon strainer and washed with FACS buffer. Cells were then incubated with CD16/32 for 10 min, and then stained with antibodies against CD4 (RM4-5), CD8α (53-6.7), CD11c (HL3), CD11b (M1/70), Ly6c (AL-21), and CD86 (GL1) on ice before flow cytometry (Cyan 5, Beckman Coulter, USA). In some experiments, cells were incubated with AH1 peptide-MHC tetramer (H-2L^d-restricted SPSYVYHQF) to label the antigen-specific T cells at room temperature for 30 min before incubation with the above antibodies.

4.3.7 Tetramer staining and intracellular cytokine staining

The percentages of tumor antigen-specific CD8α+ T cells among peripheral blood mononuclear cells (PBMCs) were analyzed using the tetramer staining assay, as described previously[10]. Briefly, 100 µl of blood was collected from each mouse on indicated days by submandibular bleeding, and red blood cells were lysed using ACK lysis buffer. PBMCs were then washed with FACS buffer and blocked by anti-CD16/32 antibody and incubated with peptide-MHC tetramer (e.g., H-2L^{d}-restricted SPSYVYHQF or H-2D^{b}-restricted ASMTNMELM) for 30 min at room temperature. Samples were then incubated with anti-mouse CD8α-APC for 20 min on ice. Cells were washed twice with FACS buffer and resuspended in 2 µg/ml DAPI solution for analysis by flow cytometry.

For intracellular cytokine staining (ICS) assay[10], 100-150 µL peripheral blood collected from mice was lysed with ACK lysis buffer, washed with PBS, and plated at ~10 million cells/mL in 50 µL T cell media (RPMI 1640 supplemented with 10% FBS, 2 mM L-glutamine, 55 µM β-mercaptoethanol, 1 mM pyruvate, 100 U/mL penicillin, 100 µg/mL streptomycin, 10 mM HEPES, and non-essential amino acids) in 96-well U-bottom plates. These PBMCs were incubated with 0.1 million CT26 cells/well for 16 h in the presence of the protein transport inhibitor, brefeldin A (BD Biosciences). Cells were then washed twice with ice-cold FACS buffer (1% BSA in PBS), followed by incubation with anti-CD16/32 for at least 10 minutes and anti-CD8α for 20 min on ice. Cells were then fixed/permeabilized for 20 min on ice and then stained with anti-IFN-γ-PE for 30 min on ice. After extensive washing, cells were analyzed by flow cytometry.

4.3.8 Statistical analysis

Sample sizes were chosen based on preliminary data from pilot experiments and previously published results in the literature. All animal studies were performed after randomization. Data were analyzed by one- or two-way analysis of variance (ANOVA), followed by Tukey's multiple comparisons post-test or log rank (Mantel-Cox) test with Prism 6.0 (GraphPad Software). Data were normally distributed and variance between groups was similar. *P* values less than 0.05 were considered statistically significant. All values are reported as means ± SD with the indicated sample size. No samples were excluded from analysis.

4.4 Results and Discussion

4.4.1 Preparation and characterization of sHDL-DOX

We prepared sHDL nanodiscs composed of an ApoA1-mimetic 37-mer peptide and 1,2-dipalmitoyl-sn-glycero-3-phosphocholine (DPPC) using a thermal-cycling method as we have reported previously[41,48,51]. To promote loading and pH-triggered release of DOX from sHDL, we tethered DOX to a hydrophobic anchor with a hydrazone linker[34], which allowed for stable drug incorporation at pH 7.4 but rapid drug release at pH 5. We conjugated DOX to 1,2-dipalmitoyl-*sn*-glycero-3-phosphothioethanol (PTD) with N-β-maleimidopropionic acid hydrazide (BMPH) linker (**Figure 4.2**), and confirmed the formation of lipid-DOX conjugate by mass spectrometry (**Figure 4.3**). To load lipid-DOX into the lipid layers of sHDL, pre-formed sHDL was simply admixed with lipid-DOX and incubated for 5 min at 37 ^{0}C, resulting in efficient incorporation of lipid-DOX into sHDL (80 ± 2% encapsulation efficiency and 2.0 ± 0.2% w/w loading) as demonstrated by co-elution of sHDL and DOX (maximum absorbance at 220 nm and 485 nm, respectively) in gel permeation chromatography (GPC) (**Figure 4.4a**). In contrast, when free DOX without the lipid tail was incubated with pre-formed sHDL, < 1% of lipid-DOX was

incorporated into sHDL (**Figure 4.4a**), suggesting the intermolecular interaction between the hydrophobic anchor of lipid-DOX and sHDL lipid layers is the major factor that drives drug loading. Transmission electron microscopy (TEM) and dynamic laser scattering (DLS) showed the homogeneous hydrodynamic size of ~ 10 nm for both "blank" sHDL and sHDL-DOX, indicating the minimal impact of drug loading on the formation and homogeneity of sHDL-DOX (**Figure 4.4b,c**). Notably, sHDL-DOX stored in a lyophilized powder form for at least 2 months was readily reconstituted with water to form homogeneous sHDL-DOX with the hydrodynamic size, PDI, and GPC chromatogram similar to those of freshly prepared sHDL-DOX (**Figure 4.4c,d**). We then examined pH-sensitive release of DOX from sHDL-DOX. Whereas sHDL-DOX incubated at pH 7.4 in PBS released less than 5% of DOX over 24 h, sHDL-DOX incubated at pH 5 rapidly released ~60% of DOX within 24 h (**Figure 4.4e**), demonstrating pH-responsive drug release at intracellular pH of endosomes/lysosomes.

4.4.2 Intracellular delivery of doxorubicin and expression of ICD markers

We next investigated the intracellular delivery of DOX and sHDL-DOX and examined their impact on 'danger signals' (e.g. HMGB1 and CRT) implicated in ICD[20,21]. We treated CT26 colon cancer cells, a widely used murine model of colon adenocarcinoma, with DOX formulations and visualized DOX fluorescence with confocal microscopy. Within 10 min of treatment, CT26 cancer cells internalized free DOX as shown by dim, diffuse DOX fluorescence signal detected throughout the cells, and uptake of free DOX was further increased until 10 h after incubation (**Figure 4.5a,b**). In contrast, sHDL-DOX treatment slowed down DOX uptake (**Figure 4.5a,b**) with the nanodiscs first phagocytosed into endolysosomes (**Figure 4.6**) and the intracellular DOX signal steadily increasing over 24 h. The IC50 value of free DOX was slightly lower than that of sHDL-DOX *in vitro* in CT26 cells (3 μM and 15 μM, respectively, **Figure**

4.7a) as well as in another murine colon carcinoma cell line, MC38 cells (0.11 μM and 0.62 μM, respectively, **Figure 4.7b**). The reduction in cytotoxicity of sHDL-DOX may be attributed to the delayed cellular uptake and drug release from sHDL-DOX *in vitro*. Importantly, despite delayed sHDL-DOX internalization, sHDL-DOX treatment mediated up-regulation of CRT **(Figure 4.8a)** and triggered robust release of HMGB1 from CT26 cells ($P < 0.01$, compared to the no treatment control, **Figure 4.8b**) to a similar degree as free DOX treatment. Overall, we have successfully synthesized a sHDL-DOX nano-formulation with the attractive features of efficient drug loading, homogeneity, long-term stability, and stimuli-responsive drug release tailored to the endolysosomal condition (**Figure 4.4-4.6**). Furthermore, despite delayed cellular uptake, sHDL-DOX can effectively kill cancer cells while maintaining the pharmacological activity of DOX to induce ICD (**Figure 4.7-4.8**).

4.4.3 In vivo chemotherapy with sHDL-DOX

We next examined the *in vivo* distribution and efficacy of the sHDL formulations in tumor-bearing mice. We inoculated BALB/c mice subcutaneously in the flank with CT26 colon carcinoma cells on day 0 and performed intravenous administration on day 11 with sHDL carrying DiR, a model fluorescent tracer with a hydrophobic anchor as in the lipid-DOX conjugate. Non-invasive whole animal imaging over time revealed that sHDL-DiR efficiently accumulated in CT26 tumors, with the fluorescence signal peaking at 24 h and lasting up to 72 h after injection (**Figure 4.9a**). When we harvested major organs at 72 h and performed quantitative imaging, we detected at least 7-fold greater radiant efficiency (defined as fluorescence intensity/area/time) in tumor tissues, compared with those in spleens, lungs, or kidneys (**Figure 4.9b,c**). As expected, the sHDL-DiR signal was strong in the liver, which is the major site for elimination of HDL[52]. To understand how sHDL affects the pharmacokinetics of

DOX, we quantified the serum concentrations of DOX after intravenous administration and fitted the results into a two-compartment model. The area under the curve (AUC) for sHDL-DOX was 27-fold greater than that of free DOX (217.5 ± 15.2 μg/mL*h for sHDL-DOX and 7.9 ± 0.1 μg/mL*h for DOX, respectively, **Figure 4.9d**). Consistent with the improved AUC, sHDL-DOX treatment resulted in 2.8-fold increase in the cellular uptake of DOX within tumors, compared with free DOX treatment ($P < 0.01$, **Figure 4.9e**)

Having shown increased accumulation of sHDL in tumors as well as improved pharmacokinetics of sHDL-DOX, we next examined the therapeutic potential of sHDL-DOX and its effect on antitumor immune responses *in vivo*. BALB/c mice were inoculated subcutaneously with CT26 cells, and when the tumor size reached ~80 mm^3 on day 8, the animals were treated three times with 4 mg/kg of DOX in either the free soluble or sHDL form (**Figure 4.10a**). At this limited dose, free DOX treatment had no discernable impact on the overall tumor growth, compared with the no treatment control group (**Figure 4.10b,c**). In contrast, sHDL-DOX treatment significantly slowed tumor growth, compared with free DOX or no treatment groups ($P < 0.0001$, **Figure 4.10b,c**). Notably, as widely reported in the literature[31], free DOX treatment triggered adverse side effects, including the body weight decrease and vacuolization of cardiomyocytes (**Figure 4.10d,e**). However, mice treated up to 3 times with the equivalent 4 mg/kg of sHDL-DOX exhibited no overt signs of toxicity, weight loss, or cardiac or liver tissue damage (**Figure 4.10d,e**).

4.4.4 Robust antitumor T cell responses induced by sHDL-DOX therapy

We next examined the impact of sHDL-mediated delivery of DOX on antitumor immune responses. We first aimed to evaluate broad antitumor cellular immune responses induced by sHDL-DOX versus free DOX treatment. Briefly, we treated CT26 tumor-bearing BALB/c mice

with DOX formulations as indicated above and examined induction of functional $CD8\alpha^+$ T cells against whole CT26 tumor cells by co-culturing peripheral blood mononuclear cells (PBMCs) with live CT26 tumor cells and performing intracellular cytokine staining (ICS) for interferon-gamma (IFN-γ). Mice that received free DOX treatment failed to expand any CT26-specific IFN-$\gamma^+CD8\alpha^+$ T cells beyond the basal level, whereas sHDL-DOX treatment generated a 7-fold higher frequency of IFN-$\gamma^+CD8\alpha^+$ T cells that recognized intact CT26 tumor cells ($P < 0.01$, **Figure 4.11a,b**).

To gain insight into antigen-specificity of cellular immune responses, we used the major histocompatibility complex-I (MHC-I) minimal epitope of CT26 gp70 (AH1) (H-$2L^d$-restricted SPSYVYHQF) as the surrogate marker of tumor-specific antigen and quantitated the frequency of AH1-specific $CD8\alpha^+$ T cells among PBMCs. Whereas CT26 tumor-bearing mice that received free DOX treatment had the basal frequency of AH1-specific $CD8\alpha^+$ T cells among PBMCs, sHDL-DOX treatment induced 3.9-fold and 3.1-fold higher AH1-specific CD8α+ T cell responses, relative to the free DOX and no treatment groups, respectively ($P < 0.001$ and $P < 0.01$, respectively **Figure 4.11c,d**). Notably, compared with mice treated with free DOX, sHDL-DOX-treated animals had a higher frequency of CD11c+CD11b+Ly6c+ DCs within the tumor-draining lymph nodes (TDLNs) ($P < 0.05$, **Figure 4.11e**). These CD11c+CD11b+Ly6c+ DCs, which are a subset of APCs that play crucial roles in the presentation of tumor antigens[53], also exhibited increased expression of a co-stimulatory marker CD86 within TDLNs (**Figure 4.11f**).

4.4.5 Potent antitumor efficacy of sHDL-DOX + αPD-1

Having confirmed immune responses triggered by sHDL-DOX monotherapy, we asked whether we could further amplify antitumor immunity and improve the therapeutic efficacy of sHDL-DOX therapy by combining this treatment with immune checkpoint blockade. Specifically, we

chose to inhibit the immunosuppressive PD-1/PD-L1 pathway[5,54] with anti-PD-1 IgG therapy (αPD-1) to reflect ongoing combination immunotherapy clinical trials. BALB/c mice were inoculated subcutaneously with $2x10^5$ CT26 tumor cells, and when the tumor size reached ~80 mm^3 on day 8, the animals were treated intravenously on days 8, 11, and 14 with 4 mg/kg of DOX in either soluble or sHDL formulation, each supplemented with intraperitoneal administrations of αPD-1 (100 μg/dose) (**Figure 4.12a**). Compared with the αPD-1 monotherapy, the combination of free DOX and αPD-1 therapy did not lead to significant expansion of AH1-specific $CD8\alpha^+$ T cells, (**Figure 4.12b,c**). In stark contrast, the combination therapy of sHDL-DOX + αPD-1 led to remarkable expansion of AH1-specific $CD8\alpha^+$ T cells, reaching the peak frequency of 5-18% AH1-specific $CD8\alpha^+$ T cells among PBMCs on day 20 (8-fold greater than the αPD-1 monotherapy on average, $P < 0.01$; and 4-fold greater than the dual free DOX + αPD-1 therapy, $P < 0.05$; **Figure 4.12b,c**).

Consistent with the enhanced antitumor immune responses, the combination chemoimmunotherapy with sHDL-DOX and αPD-1 exerted dramatic antitumor efficacy, leading to the elimination of established tumors (~80 mm^3 at the initiation of treatment on day 8) in 88% of animals after three cycles of dual sHDL-DOX + αPD-1 therapy ($P < 0.0001$, **Figure 4.12d,e**). This is in stark contrast to the αPD-1 monotherapy or free DOX plus αPD-1 dual therapy that failed to inhibit the average tumor growth at this low dose/frequency regimen ($P < 0.0001$, **Figure 4.12d,e**). Importantly, 100% of the surviving animals from the sHDL-DOX + αPD-1 treatment group rejected the subsequent re-challenge with $2x10^5$ CT26 tumor cells performed on day 60 either by subcutaneous or intravenous route of administration (**Figure 4.12f,g**), suggesting the establishment of durable immunity against tumor relapse. Moreover, throughout our studies, we did not observe any signs of weight loss, toxicity, nor autoimmunity in animals

treated up to three times with sHDL-DOX + αPD-1 dual therapy. Collectively, these results demonstrated that sHDL-DOX therapy combined with αPD-1 therapy elicited potent antitumor $CD8\alpha^+$ T cell responses *in vivo*, thereby exerting robust antitumor efficacy against established tumors and tumor relapse.

4.4.6 T cell responses in the tumor microenvironment

Since tumor-infiltrating lymphocytes are one of the key determinants for the outcome of immunotherapy, we sought to profile antitumor T lymphocytes in the tumor microenvironment of animals undergoing chemoimmunotherapy. BALB/c mice were inoculated with $2x10^5$ CT26 tumor cells and treated with various formulations as stated above. Notably, among various formulations tested, the dual sHDL-DOX + αPD-1 therapy recruited the highest frequency of $CD8\alpha^+$ T cells into the tumor microenvironment (3-fold greater than the free DOX treatment, $P < 0.05$, **Figure 4.13a**). The sHDL-DOX + αPD-1 therapy also promoted the highest frequency and absolute number of tumor-infiltrating $CD8\alpha^+$ T cells recognizing the CT26 AH1 antigen (5-fold greater than the non-treated control group, $P < 0.05$, **Figure 4.13b,c)**. These results, in general, reflected the patterns of systemic antigen-specific $CD8\alpha^+$ T cell responses induced after the combination sHDL-DOX + αPD-1 therapy (**Figure 4.13b,c**).

4.4.7 Neoantigen-specific CD8+ T cell responses induced by chemoimmunotherapy

Recent studies have shown that antitumor efficacy of immune checkpoint blockade is strongly correlated with T cell responses against neoantigens, which are antigens encoded by somatic gene mutations only found in cancerous cells[42,44,55]. Here, we studied the impact of sHDL-mediated DOX delivery on the generation of neoantigen-specific T cell responses and also sought to validate our results using another murine colon carcinoma model of MC38 tumor cells syngeneic to C57BL/6 mice. Animals were inoculated with 2×10^5 MC38 tumor cells via

subcutaneous administration, and when the average tumor size reached ~60 mm^3 on day 8, we performed intravenous administration with 4 mg/kg dose of free DOX or sHDL-DOX, supplemented with αPD-1 therapy or PBS (**Figure 4.14a**). To monitor neoantigen-specific T cell responses, we utilized a recently reported mutated neo-epitope within Adpgk protein (ASMTN**R**ELM → ASMTN**M**ELM mutation), which is presented on MC38 tumor cells in the context of H-$2D^b$ molecules[56]. The dual sHDL-DOX + αPD-1 chemoimmunotherapy generated 2.4-fold greater expansion of neoantigen-specific $CD8\alpha^+$ T cells among PBMCs, compared with free DOX or sHDL-DOX treatment ($P < 0.05$, **Figure 4.14b,c**). Importantly, sHDL-DOX + αPD-1 dual therapy exerted potent antitumor efficacy, leading to complete regression of established tumors (~60 mm^3 at the initiation of therapy on day 8) to an undetectable level in 80% of animals ($P < 0.0001$, **Figure 4.15a,b**). This is in contrast to all other treatment groups that exhibited increasing average tumor sizes over time. Overall, two cycles of sHDL-DOX + αPD-1 chemoimmunotherapy led to complete tumor response in 80% of animals (**Figure 4.15a,b**). On the other hand, αPD-1 monotherapy and free DOX + αPD-1 dual therapy mediated tumor regression in ~40% of animals. None of the animals treated with DOX or sHDL-DOX chemotherapy had tumor regression. Importantly, mice cured of the primary MC38 tumors with sHDL-DOX + αPD-1 dual therapy were also completely protected from MC38 tumor cell re-challenge performed on day 60 by either subcutaneous or intravenous injection ($P < 0.01$, **Figure 4.15c,d**), thus indicating long-term protection against tumor relapse.

4.5 Conclusion

In this study, we present our proof-of-concept design that utilizes sHDL nanodiscs for delivering an ICD inducer, DOX, and achieving potent antitumor efficacy in combination with ICBs. Specifically, we have demonstrated that sHDL nanodiscs, composed of the 37-amino acid

ApoA1 mimetic peptide and phospholipids, serve as a promising platform for chemoimmunotherapy. Compared with free DOX therapy, sHDL-DOX showed a 27-fold increase in PK profiles in animals and increased tumor accumulation without any targeting moiety. Monotherapy with sHDL-DOX significantly delayed tumor growth without any overt off-target side effects. Importantly, sHDL-DOX treatment triggered robust antitumor T cell responses while broadening their epitope recognition to tumor-associated antigens, neoantigens, as well as intact whole tumor cells. Elicitation of neoantigen-specific T cell responses is quite notable as this class of tumor antigens is under intense investigation for personalized cancer vaccines, as we and others have reported[10,50,56]. Furthermore, the therapeutic efficacy of ICBs was recently shown to be directly correlated with neoantigen-specific T cell responses[43-45], thus raising the prospect that "priming" tumors with sHDL-DOX therapy may potentiate ICBs - even without *a priori* knowledge of tumor antigens. Indeed, the combination of sHDL-DOX plus ICB therapy elicited strong antitumor immune responses and markedly augmented their therapeutic efficacy; co-treatment with sHDL-DOX plus αPD-1 IgG antibody induced complete regression of established colon carcinoma in 80-88% of animals (CT26 and MC38 tumors in BALB/c and C57BL/6 mice, respectively) while protecting all survivors against tumor cell re-challenge. This is in stark contrast to the animals treated with free DOX plus αPD-1 dual therapy or αPD-1 monotherapy, which failed to decrease the average tumor sizes with the response rates remaining below 40%.

An extensive list of nanoparticle systems, such as liposomes, synthetic polymers, micelles, and inorganic nanostructures, has been examined for delivery of DOX with varying levels of success[34-38], but their impact on antitumor immunity and hence their potential as a platform for chemoimmunotherapy remains to be explored. The work presented here is, to the best of our

knowledge, the first report of chemo-nanotechnology designed to trigger ICD of tumor cells and elicit T cell immunity against a broad range of tumor antigens, including neoantigens, thereby potentiating immune checkpoint blockade. While other conventional nano-formulations may also be applicable to this approach, we believe the sHDL system is particularly attractive for translation due to the ease of synthesis, established large-scale manufacturing, proven human safety, and non-immunogenicity of the "blank" sHDL as demonstrated in a number of clinical trials[40,41,57]. In addition, the cardioprotective effect of HDL[58-60] may further alleviate cardiotoxicity associated with sHDL-DOX treatment. Moreover, conventional nanoparticles typically require PEGylation for sufficient circulation half-life and drug accumulation in tumors; however, repeated administrations of PEGylated materials can cause chronic Hand-Foot Syndrome[61] as well as anti-PEG antibody responses,[62] thus potentially complicating their application in immunotherapy. In contrast, sHDL nanodiscs mimicking endogenous HDL do not require PEGylation for efficient DOX delivery. While the precise mechanisms are under investigation, we speculate that sHDL-mediated intratumoral delivery of DOX is facilitated in part by their ultrasmall particle size (~10 nm), extended pharmacokinetics, and extensive uptake by metabolically highly active cancer cells that require a large amount of lipids and cholesterol for proliferation[41,48,49].

In conclusion, we have produced a new, generalizable framework for chemoimmunotherapy. By delivering chemotherapeutic agents via nanocarriers in a manner that sensitizes tumor cells to immune activation and subsequent immune checkpoint blockade, we have achieved potent antitumor efficacy, leading to elimination of established tumors in 80-88% of animals. Our approach may be readily applied to other chemotherapeutic agents known to induce ICD of tumor cells[17,18,21]. As there is intense interest in improving the patient response rate and

therapeutic efficacy of immune checkpoint blockade, our strategy presented here may have a wide-ranging impact in the field of drug delivery, nanotechnology, and cancer immunotherapy.

4.6 Figures

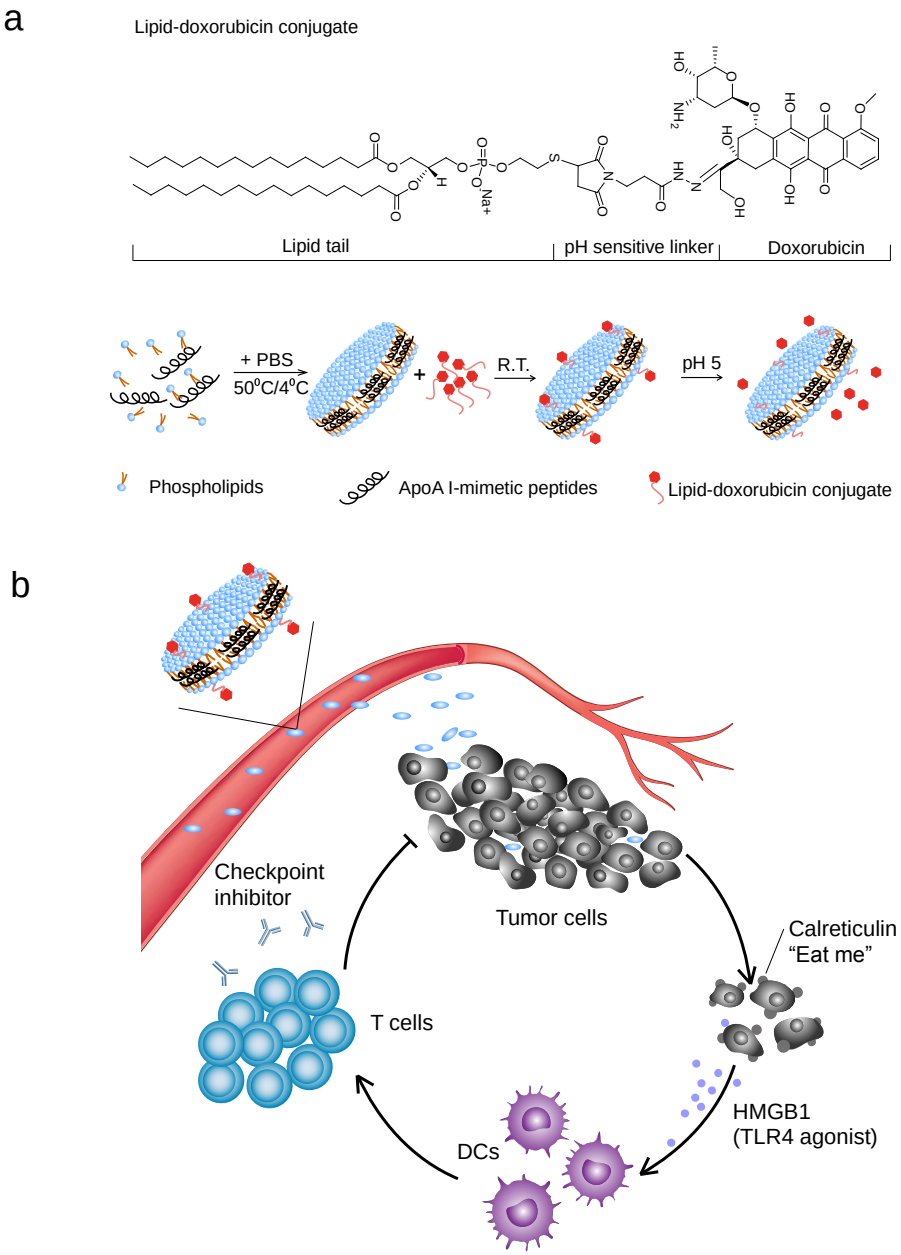

Figure 4.1. Schematic of doxorubicin-loaded sHDL (sHDL-DOX) for chemo-immunotherapy. **a**, sHDL-DOX is formulated by incubation of lipid-doxorubicin with preformed-sHDL. **b**, The ultrasmall size and prolonged circulation of sHDL enable intratumoral delivery of DOX, followed by internalization by tumor cells and pH-responsive release of DOX in the endosomes/lysosomes. Released DOX kills tumor cells and triggers immunogenic cell death, promoting upregulation of calreticulin (the "eat me" signal) and release of "danger " signals such as HMGB1. Dendritic cells recruited to the immunogenically dying tumor cells phagocytose them, process tumor antigens, and cross-prime tumor antigen-specific T cells. Antitumor immunity "primed" with sHDL-DOX synergizes with immune checkpoint blockade, leading to efficient elimination of established tumors and prevention of tumor relapse.

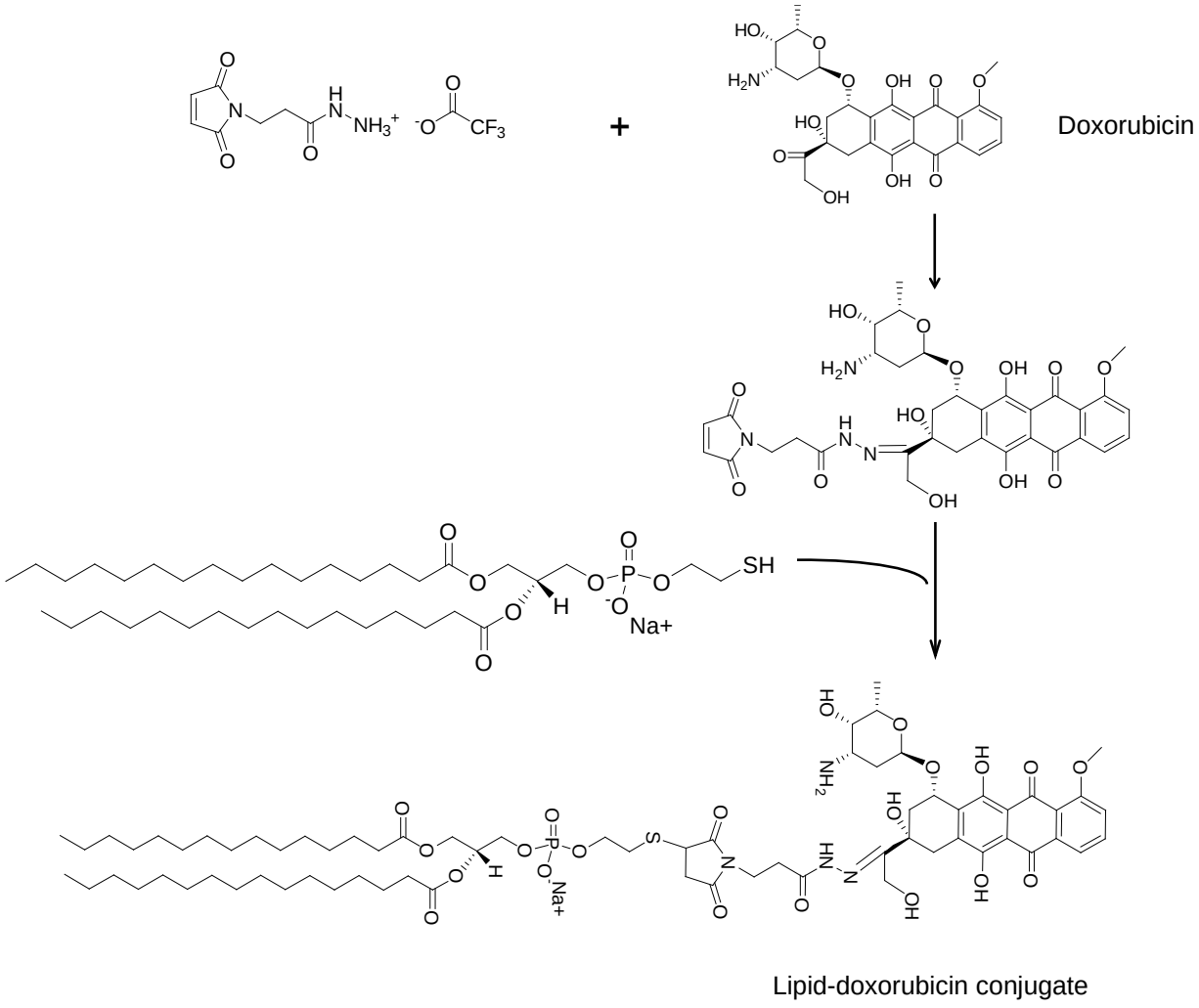

Figure 4.2 . Schematic for the synthesis of lipid-doxorubicin conjugate.

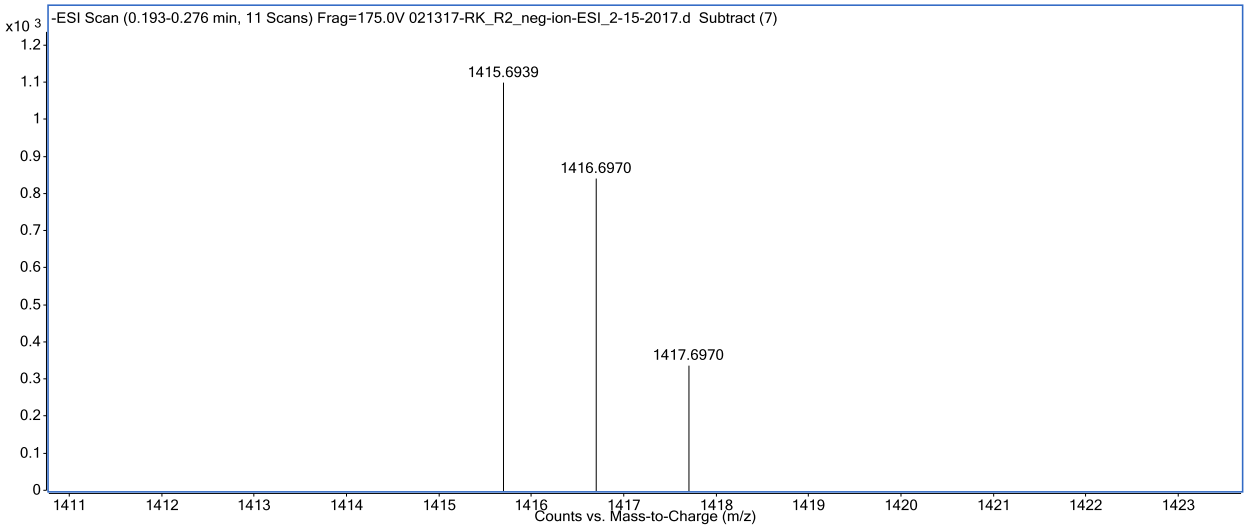

Figure 4.3. Mass spectroscopy confirmed the conjugation of doxorubicin to 1,2-Dipalmitoyl-sn-Glycero-3-Phosphothioethanol (PTD). The Measured m/z of [M-Na]+ is 1415.6939 and predicted value is 1415.6970.

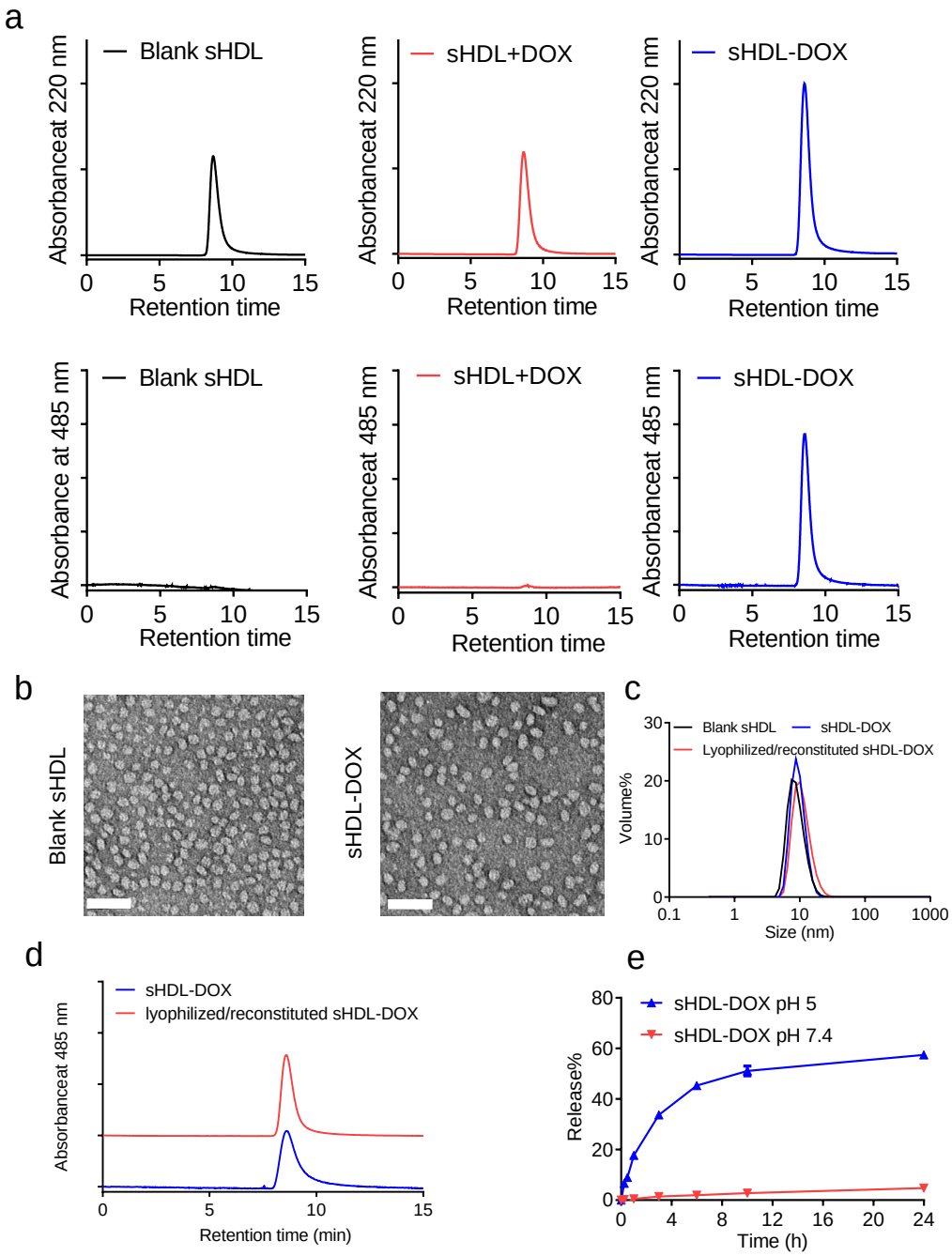

Figure 4.4. Preparation and characterization of sHDL-DOX. **a**, Gel permeation chromatography (GPC) of blank sHDL, the physical mixture of sHDL+DOX, and sHDL covalently attached with DOX (sHDL-DOX) at 220 nm and 485 nm. **b**, Transmission electron microscopy (TEM) of blank sHDL and sHDL-DOX. Scale bars = 50 nm. **c-d**, Sizes of sHDL-DOX before and after lyophilization/reconstitution measured by dynamic light scattering (DLS)(**c**) and GPC (**d**) . **e**, Release of doxorubicin from sHDL at pH 5 and pH 7.5. Data represent mean ± SD (n = 3).

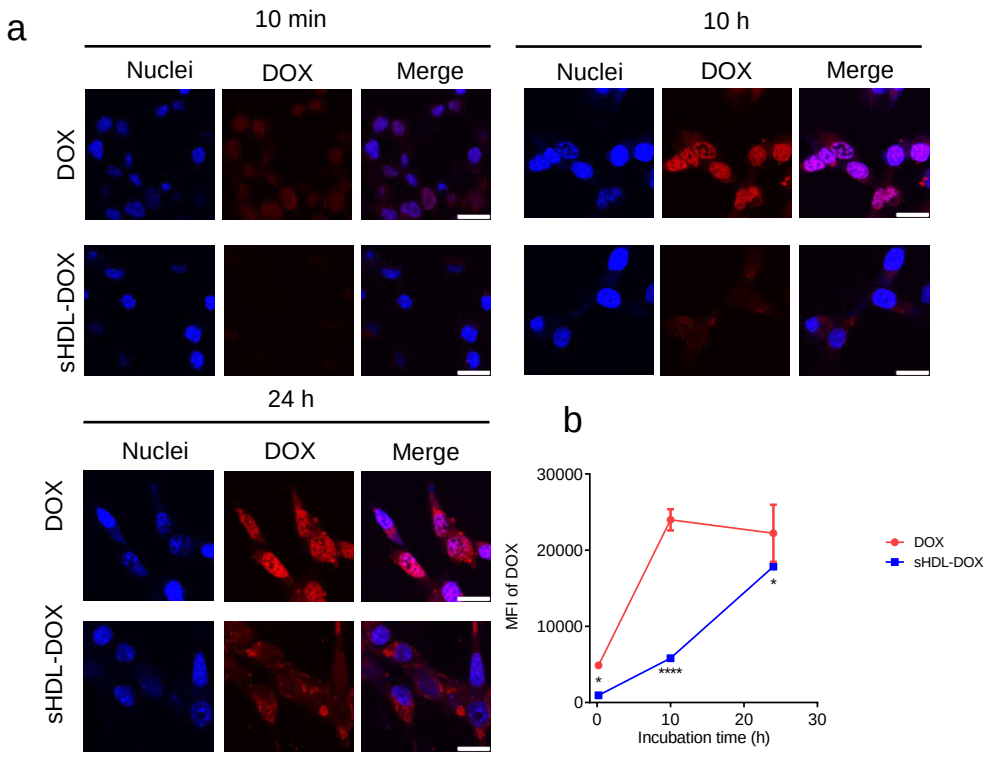

Figure 4.5. a-b CT26 cells were incubated with 40 μM DOX or sHDL-DOX for indicated for indicated lengths of time (10 min, 10 h, and 24 h). The cellular uptake of DOX or sHDL-DOX was analyzed by confocal microscopy (**a**) and flow cytometry (**b**). * $P < 0.05$, **** $P < 0.0001$ analyzed by two-way ANOVA with Bonferroni's multiple comparisons post-test. Data represent mean ± SD (n=3).

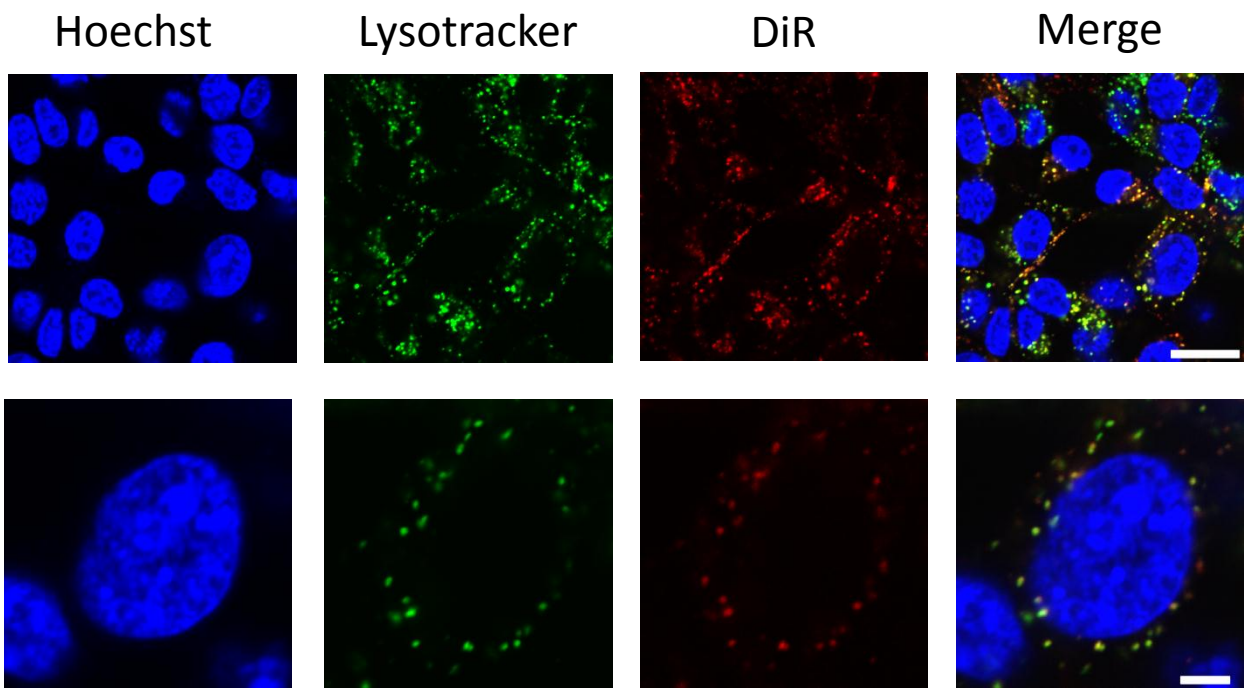

Figure 4.6. CT26 cells were incubated with sHDL-DiR (20 ng/DiR) for 24 h. Cells were then stained with lysotracker (green) and nuclei were stained with Hoechst before confocal microscopy. Scale bar = 20 μm.

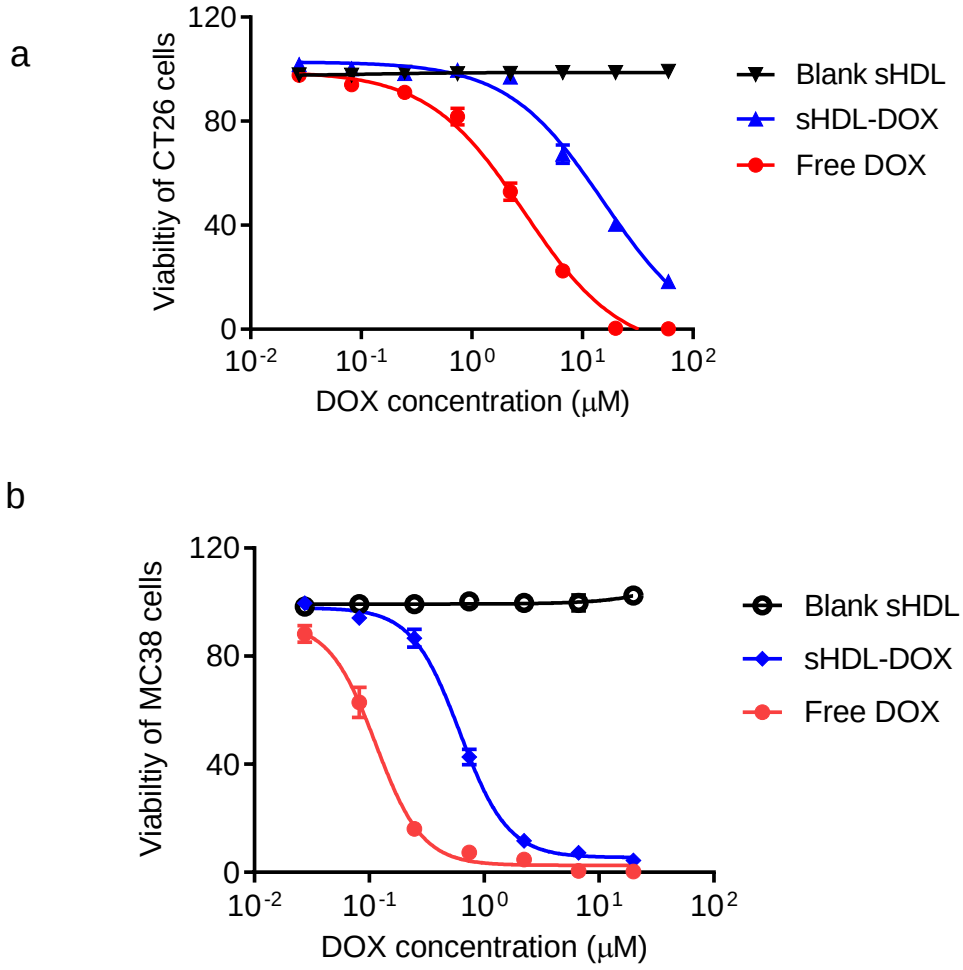

Figure 4.7. Cytotoxicity of sHDL-DOX. **a-b**, CT26 tumor cells (**a**) or MC38 tumor cells (**b**) were incubated with serial dilutions of free DOX or sHDL-DOX for 72 h, and cellular viability was measured by the cell counting kit. Data represent mean ± SD (n = 3) from a representative experiment from 2–3 independent experiments.

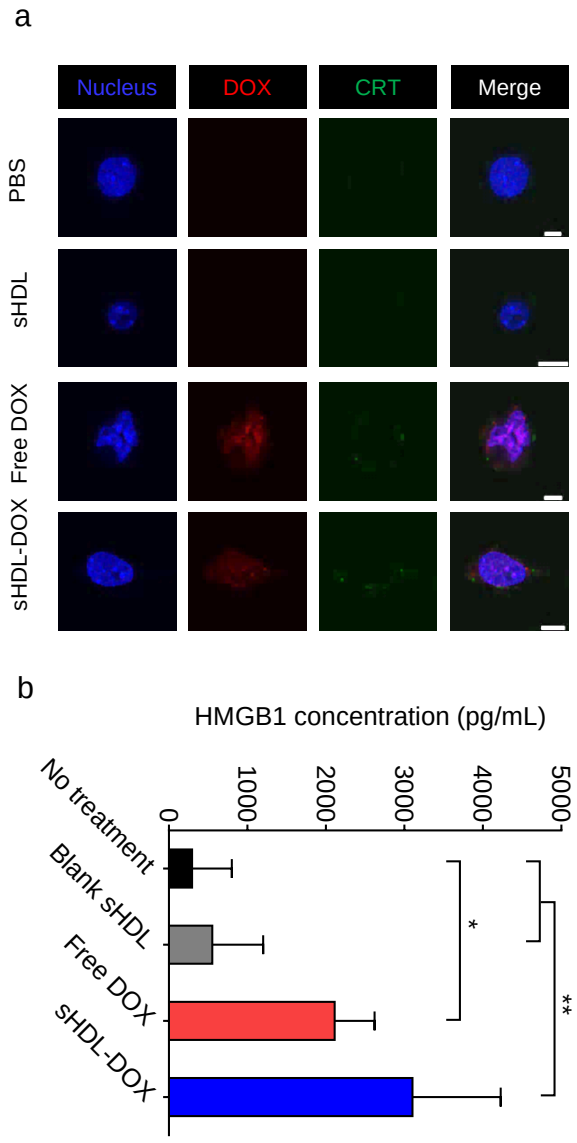

Figure 4.8. CT26 cells were incubated with indicated formulations (equivalent to 50 μM DOX) for 24 h. CRT was imaged by confocal microscopy after proper staining with fluorophore-tagged antibodies. Release of HMGB1 was quantified by ELISA after CT26 tumor cells were treated with indicated formulations (equivalent to 50 μM DOX). * $P < 0.05$, ** $P < 0.01$ analyzed by one-way ANOVA with Tukey's multiple comparisons post-test. Data represent mean ± SD (n = 3) from a representative experiment from 2–3 independent experiments.

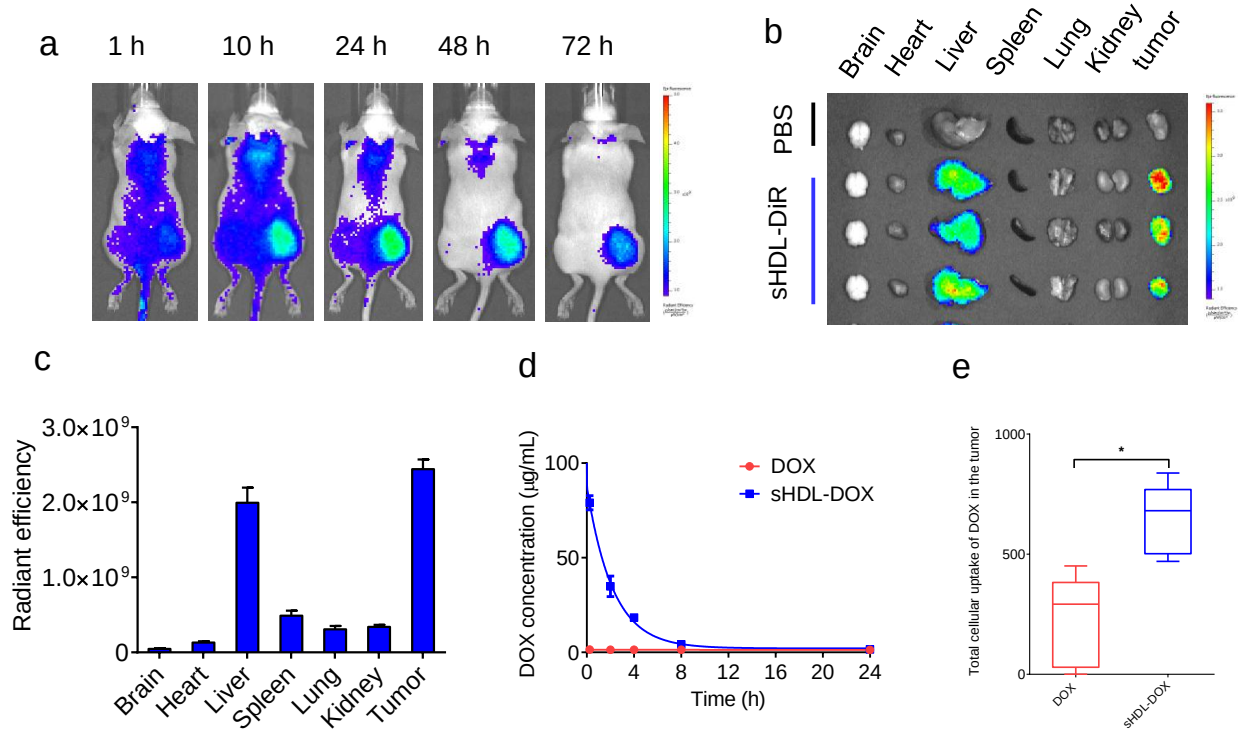

Figure 4.9. Antitumor efficacy and T cell immunity exerted by sHDL-DOX monotherapy**. a**, CT26 tumor-bearing mice were intravenously injected with sHDL-DiR, and the biodistribution of sHDL-DiR at different time points were imaged by the IVIS optical imaging system. **b**, At 72 h post injection, major organs were harvested and imaged ex vivo, and **c**, fluorescence signal was quantified. **d**, BALB/c mice were intravenously injected with free DOX or sHDL-DOX at 4 mg/kg DOX. Shown are the serum concentrations of DOX fitted to the two-compartment model. Data represent mean ± SD (n = 3) from a representative experiment from 2-3 independent experiments. **e**, CT26 tumor-bearing mice were intravenously injected with 8 mg/kg DOX or sHDL-DOX mL. Twenty-four hours after injection, mice were euthanized and tumors were harvested and prepared into single-cell suspension. The total uptake of DOX or sHDL-DOX by all cells in the tumors were measured by flow cytometry and represented as the MFI of DOX. $*P < 0.05$ analyzed by unpaired t test. n = 5.

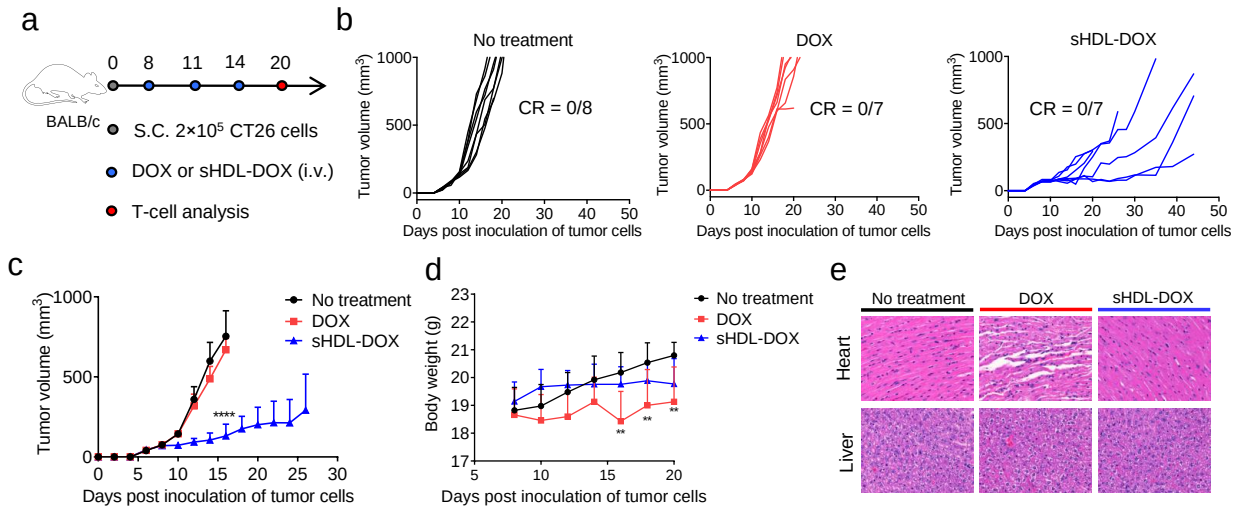

Figure 4.10. Antitumor efficacy and T cell immunity exerted by sHDL-DOX monotherapy**. a**, BALB/c mice were subcutaneously inoculated with 2×10^5 CT26 cells on day 0. On days 8, 11, and 14, tumor-bearing mice were treated with indicated formulations at 4 mg/kg DOX. **b-c**, The average and individual CT26 tumor growth curves for mice treated with indicated formulations. CR = complete tumor regression. **d**, Body weights of CT26 tumor-bearing mice treated with indicated formulations. **e**, H&E staining of the hearts and livers harvested on day 20 from tumor-bearing mice treated with indicated formulations. ** $P < 0.01$, *** $P < 0.001$, **** $P < 0.0001$ analyzed by two-way ANOVA (**c,d**) with Tukey's multiple comparisons post-test.

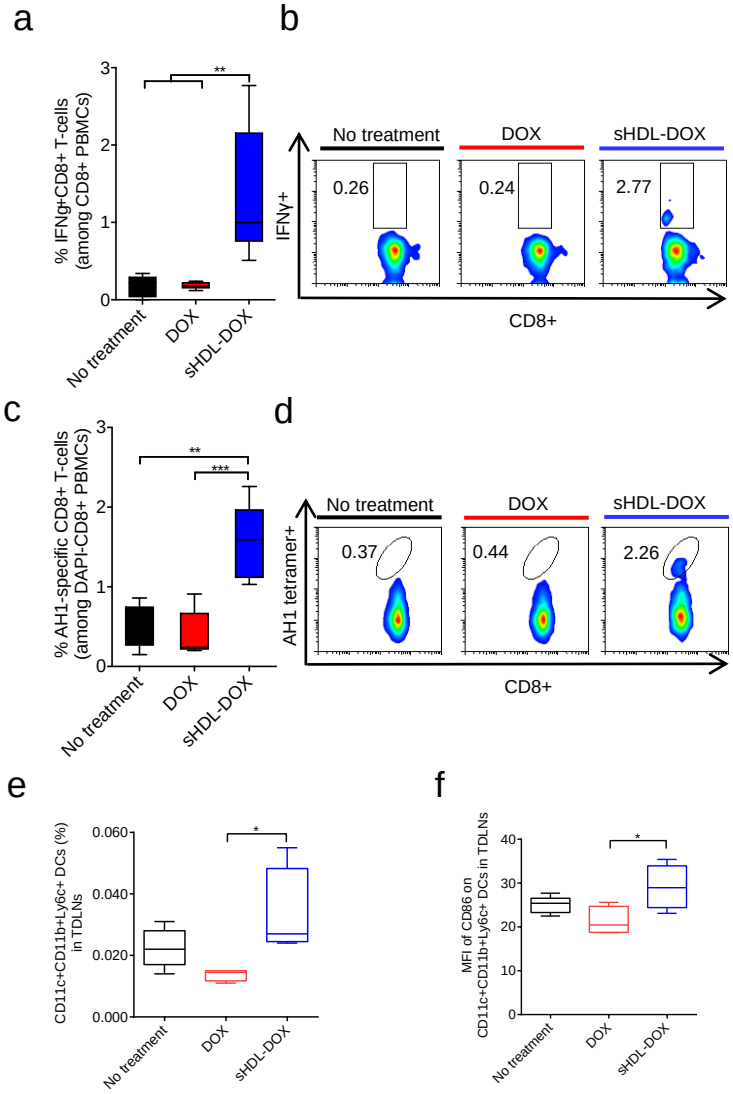

Figure 4.11. Antitumor efficacy and T cell immunity exerted by sHDL-DOX monotherapy**.** BALB/c mice were subcutaneously inoculated with 2×10^5 CT26 cells on day 0. On days 8, 11, and 14, tumor-bearing mice were treated with indicated formulations at 4 mg/kg DOX. **a-b**, The percent of tumor cell-reactive T cells (IFNγ+CD8+) among PBMCs on day 20 was measured by intracellular cytokine staining (ICS). Shown are **a** the percent of IFNγ+CD8+ among PBMCs on day 20, and **b** the representative scatter plots. **c**, the percent of CT26 tumor antigen peptide AH1-specific CD8+ T cells among PBMC on day 20, and **d** the representative scatter plots. **e-f,** Balb/c mice were inoculated with 2×10^5 CT26 cells on day 0. On days 8 and 11, tumor-bearing mice were treated with indicated formulations at 4mg/kg DOX. Shown are the percent of CD11c+CD11b+Lyc+ DCs and CD86 levels in the TDLNs (**e-f**). Data are represented as box plots (whiskers 5–95 percentile, n = 4-5) from a representative experiment from 2 independent experiments. ** $P < 0.01$, *** $P < 0.001$, **** $P < 0.0001$ analyzed by one-way ANOVA with Tukey's multiple comparisons post-test.

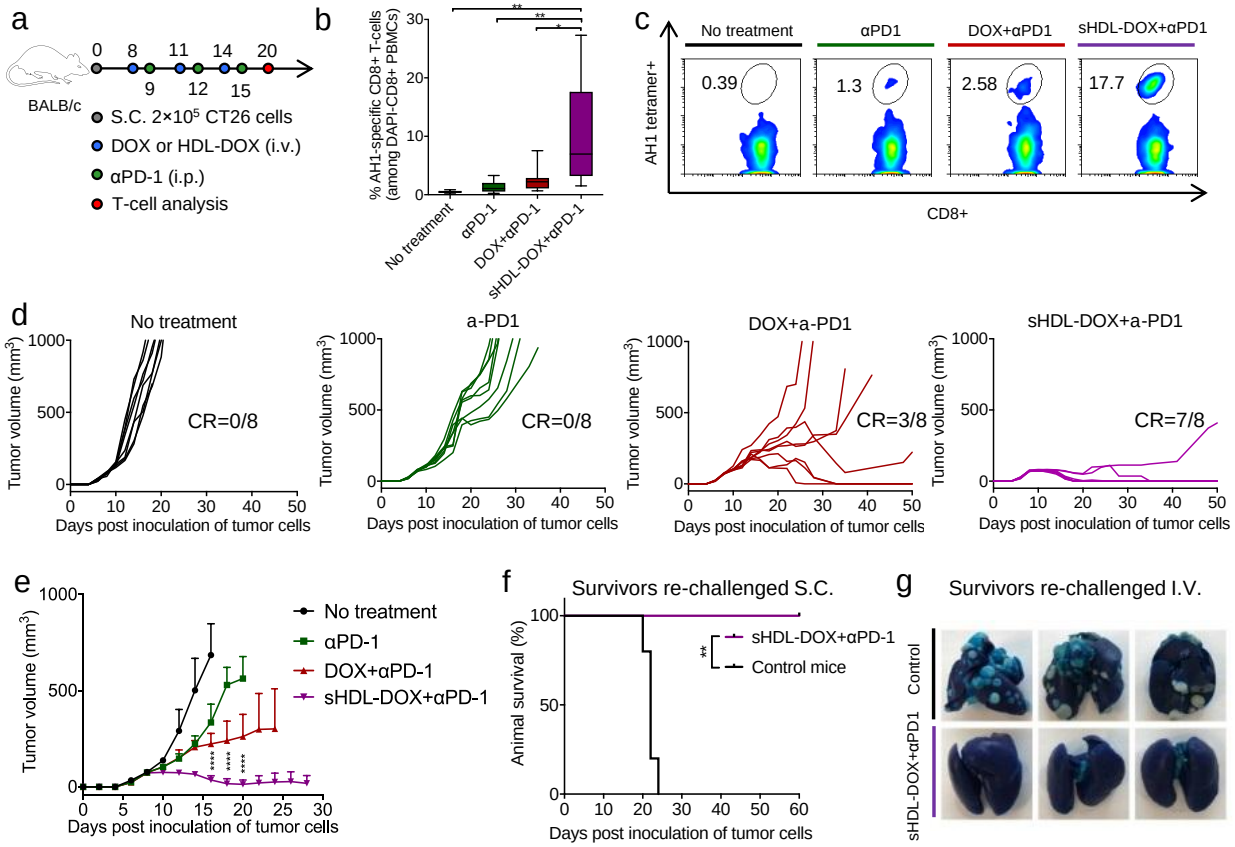

Figure 4.12. Potentiation of αPD-1 immunotherapy with sHDL-DOX for treatment of CT26 tumors**. a**, BALB/c mice were subcutaneously inoculated with 2×10^5 CT26 cells on day 0. On days 8, 11, and 14, tumor-bearing mice were treated with indicated formulations at 4 mg/kg DOX. αPD-1 was injected i.p. at 100 ug/dose on days 9, 12, and 15. **b**, The percent of CT26 tumor antigen AH1-specific CD8+ T cells among PBMC on day 20, and **c** the representative scatter plots. Data are represented as box plots (whiskers 5–95 percentile). n = 5 from a representative experiment from 2 independent experiments. **d**, Individual growth curves for mice treated with indicated formulations. CR = complete tumor regression. **e**, The average tumor growth curves for mice treated with indicated formulations. Data represent mean ± SD (n = 8) from a representative experiment from 2 independent experiments. **f-g,** On day 60, cured mice in **e** were re-challenged subcutaneously (**f**) or intravenously (**g**) with 2×10^5 CT26 cells. Shown are the animal survival (**f**) and lung metastasis (**g**) of CT26 cells on day 22 after re-challenge. Naïve mice were used as control and inoculated with the same number of tumor cells. * $P < 0.05$, ** $P < 0.01$, and **** $P < 0.0001$ analyzed by one-way ANOVA (**b**), or two-way ANOVA (**e**) with Tukey's multiple comparisons post-test, or log rank (Mantel-Cox) test (**f**).

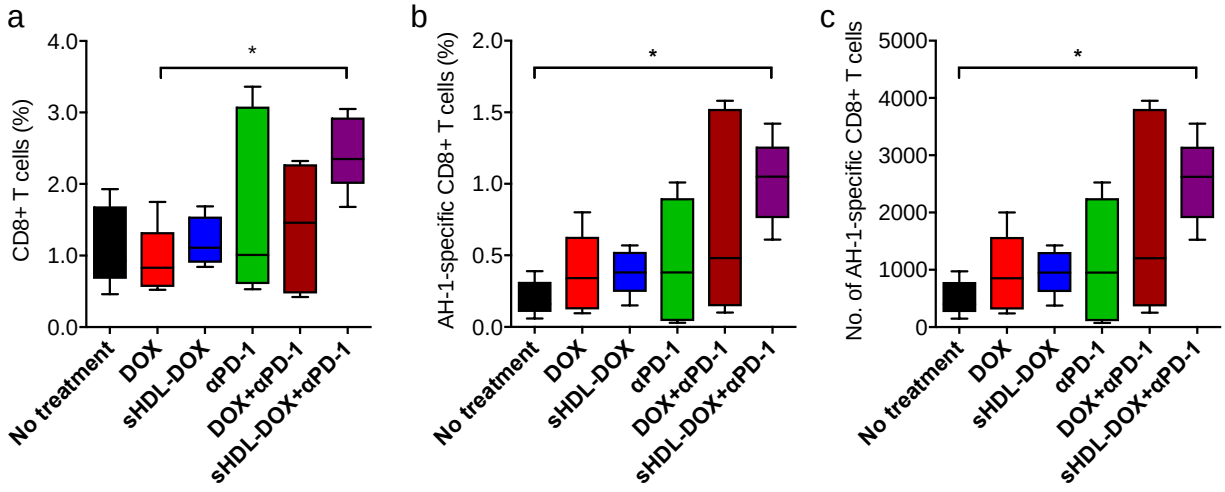

Figure 4.13. Antitumor immune responses in the tumor microenvironment**. a**, BALB/c mice were subcutaneously inoculated with 2×10^5 CT26 cells on day 0. On days 8, and 11, CT26 tumor-bearing mice were treated with indicated formulations at 4 mg/kg DOX. For the combination immunotherapy, αPD-1 was injected i.p. at 100 ug/dose on days 9 and 12. Shown are the percent of CD8+ T cells **(a)**, the percent of AH1-specific CD8+ T cells **(b)**, and the number of AH1-specific CD8+ T cells/250,000 cells **(c)** in tumors on day 15. * $P < 0.05$ analyzed by one-way ANOVA with Tukey's multiple comparisons post-test. Data are represented as box plots (whiskers 5–95 percentile). n = 5 from a representative experiment from 2 independent experiments.

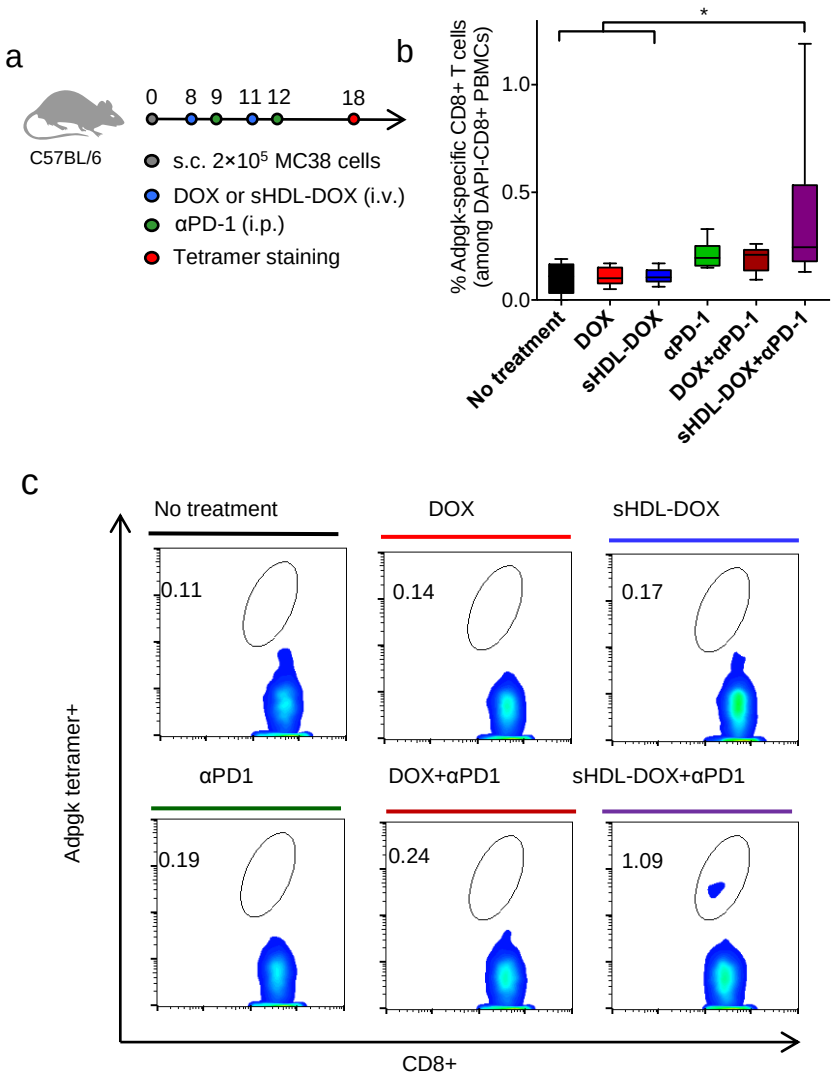

Figure 4.14. Chemo-immunotherapy for induction of neoantigen-specific T cell responses and elimination of MC38 tumors. **a**. C57BL/6 mice were inoculated subcutaneously with 2×10^5 MC38 cells on day 0. On days 8 and 11, tumor-bearing mice were treated with indicated DOX-containing formulations at 4 mg/kg DOX. For the combination immunotherapy, αPD-1 was injected i.p. at 100 μg/dose on days 9 and 12. On day 18, the percent of Adpgk-specific CD8+ T cells among PBMCs was measured. Data are represented as box plots (whiskers 5–95 percentile). n = 5 for no treatment and n = 8 for other groups, from a representative experiment from 2 independent experiments. **b-c**, The percent of Adpgk-specific CD8+ T cells among PBMCs (**b**) and the representative scatter plots (**c**). * $P < 0.05$, ** $P < 0.01$, and **** $P < 0.0001$ analyzed by one-way ANOVA (**b**).

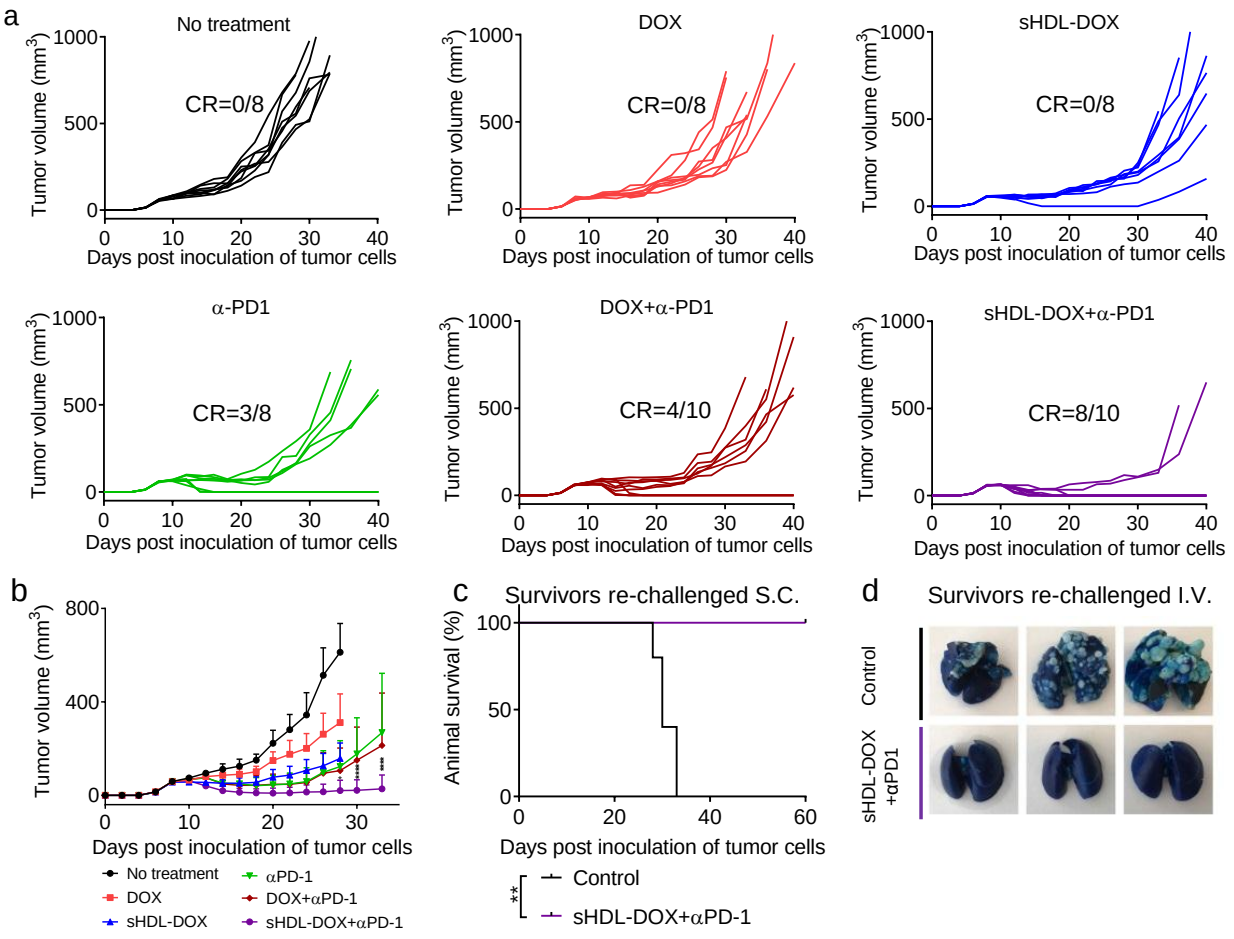

Figure 4.15. Chemo-immunotherapy for induction of neoantigen-specific T cell responses and elimination of MC38 tumors. **a**. C57BL/6 mice were inoculated subcutaneously with 2×10^5 MC38 cells on day 0. On days 8 and 11, tumor-bearing mice were treated with indicated DOX-containing formulations at 4 mg/kg DOX. For the combination immunotherapy, αPD-1 was injected i.p. at 100 μg/dose on days 9 and 12. **a**, Individual tumor growth curves of mice treated with indicated formulations. CR = complete tumor regression. **b**, The average tumor growth curves of mice treated with indicated formulations. Data represent mean ± SD. n = 8-10, from a representative experiment from 2 independent experiments. **c-d**, On day 60, cured mice were re-challenged s.c. (**c**) or i.v (**d**) with 2×10^5 MC38 cells. Shown are the survival (**c**) and lung metastasis of MC38 cells (**d**) on day 26 after re-challenge. Naïve mice were used as control and inoculated with the same number of tumor cells. * $P < 0.05$, ** $P < 0.01$, and **** $P < 0.0001$ analyzed by two-way ANOVA (**b**) with Tukey's multiple comparisons post-test, or log rank (Mantel-Cox) test (**c**).

4.7 References

1. Hodi FS, O'Day SJ, McDermott DF, et al. Improved survival with ipilimumab in patients with metastatic melanoma. *N Engl J Med.* Aug 19 2010;363(8):711-723.

2. Robert C, Schachter J, Long GV, et al. Pembrolizumab versus Ipilimumab in Advanced Melanoma. *N Engl J Med.* Jun 25 2015;372(26):2521-2532.

3. Garon EB, Rizvi NA, Hui R, et al. Pembrolizumab for the treatment of non-small-cell lung cancer. *N Engl J Med.* May 21 2015;372(21):2018-2028.

4. Rosenberg JE, Hoffman-Censits J, Powles T, et al. Atezolizumab in patients with locally advanced and metastatic urothelial carcinoma who have progressed following treatment with platinum-based chemotherapy: a single-arm, multicentre, phase 2 trial. *Lancet.* May 07 2016;387(10031):1909-1920.

5. Topalian SL, Hodi FS, Brahmer JR, et al. Safety, activity, and immune correlates of anti-PD-1 antibody in cancer. *N Engl J Med.* Jun 28 2012;366(26):2443-2454.

6. Mellman I, Coukos G, Dranoff G. Cancer immunotherapy comes of age. *Nature.* Dec 22 2011;480(7378):480-489.

7. Topalian SL, Hodi FS, Brahmer JR, et al. Safety, activity, and immune correlates of anti-PD-1 antibody in cancer. *N Engl J Med.* Jun 28 2012;366(26):2443-2454.

8. Cho HI, Barrios K, Lee YR, Linowski AK, Celis E. BiVax: a peptide/poly-IC subunit vaccine that mimics an acute infection elicits vast and effective anti-tumor CD8 T-cell responses. *Cancer Immunol Immunother.* Apr 2013;62(4):787-799.

9. Duraiswamy J, Kaluza KM, Freeman GJ, Coukos G. Dual blockade of PD-1 and CTLA-4 combined with tumor vaccine effectively restores T-cell rejection function in tumors. *Cancer Res.* Jun 15 2013;73(12):3591-3603.

10. Kuai R, Ochyl LJ, Bahjat KS, Schwendeman A, Moon JJ. Designer vaccine nanodiscs for personalized cancer immunotherapy. *Nat Mater.* Apr 2017;16(4):489-496.

11. Demaria S, Kawashima N, Yang AM, et al. Immune-mediated inhibition of metastases after treatment with local radiation and CTLA-4 blockade in a mouse model of breast cancer. *Clin Cancer Res.* Jan 15 2005;11(2 Pt 1):728-734.

12. Belcaid Z, Phallen JA, Zeng J, et al. Focal radiation therapy combined with 4-1BB activation and CTLA-4 blockade yields long-term survival and a protective antigen-specific memory response in a murine glioma model. *PLoS One.* 2014;9(7):e101764.

13. Twyman-Saint Victor C, Rech AJ, Maity A, et al. Radiation and dual checkpoint blockade activate non-redundant immune mechanisms in cancer. *Nature.* Apr 16 2015;520(7547):373-377.

14. Kang TH, Mao CP, Lee SY, et al. Chemotherapy acts as an adjuvant to convert the tumor microenvironment into a highly permissive state for vaccination-induced antitumor immunity. *Cancer Res.* Apr 15 2013;73(8):2493-2504.

15. Pfirschke C, Engblom C, Rickelt S, et al. Immunogenic Chemotherapy Sensitizes Tumors to Checkpoint Blockade Therapy. *Immunity.* Feb 16 2016;44(2):343-354.

16. Mathios D, Kim JE, Mangraviti A, et al. Anti-PD-1 antitumor immunity is enhanced by local and abrogated by systemic chemotherapy in GBM. *Sci Transl. Med.* Dec 21 2016;8(370):370ra180.

17. Apetoh L, Ghiringhelli F, Tesniere A, et al. Toll-like receptor 4-dependent contribution of the immune system to anticancer chemotherapy and radiotherapy. *Nat Med.* Sep 2007;13(9):1050-1059.

18. Obeid M, Tesniere A, Ghiringhelli F, et al. Calreticulin exposure dictates the immunogenicity of cancer cell death. *Nat Med.* Jan 2007;13(1):54-61.

19. Ghiringhelli F, Apetoh L, Tesniere A, et al. Activation of the NLRP3 inflammasome in dendritic cells induces IL-1beta-dependent adaptive immunity against tumors. *Nat Med.* Oct 2009;15(10):1170-1178.

20. Green DR, Ferguson T, Zitvogel L, Kroemer G. Immunogenic and tolerogenic cell death. *Nat Rev Immunol.* May 2009;9(5):353-363.

21. Kroemer G, Galluzzi L, Kepp O, Zitvogel L. Immunogenic cell death in cancer therapy. *Annu Rev Immunol.* 2013;31:51-72.

22. Ma Y, Mattarollo SR, Adjemian S, et al. CCL2/CCR2-dependent recruitment of functional antigen-presenting cells into tumors upon chemotherapy. *Cancer Res.* Jan 15 2014;74(2):436-445.

23. Krysko DV, Garg AD, Kaczmarek A, Krysko O, Agostinis P, Vandenabeele P. Immunogenic cell death and DAMPs in cancer therapy. *Nat Rev Cancer.* Dec 2012;12(12):860-875.

24. Sistigu A, Yamazaki T, Vacchelli E, et al. Cancer cell-autonomous contribution of type I interferon signaling to the efficacy of chemotherapy. *Nat Med.* Nov 2014;20(11):1301-1309.

25. Van der Sluis TC, Van Duikeren S, Huppelschoten S, et al. Vaccine-induced tumor necrosis factor-producing T cells synergize with cisplatin to promote tumor cell death. *Clin Cancer Res.* Feb 15 2015;21(4):781-794.

26. Rios-Doria J, Durham N, Wetzel L, et al. Doxil synergizes with cancer immunotherapies to enhance antitumor responses in syngeneic mouse models. *Neoplasia.* Aug 2015;17(8):661-670.

27. Safety and efficacy study of Pembrolizumab (MK-3475) in combination with chemotherapy as neoadjuvant treatment for participants with triple negative breast cancer (TNBC) (MK-3475-173/KEYNOTE 173). 2015; https://clinicaltrials.gov/ct2/show/NCT02622074.

28. Pembrolizumab and doxorubicin hydrochloride or anti-estrogen therapy in treating patients with triple negative or hormone receptor positive metastatic breast cancer. 2016; https://clinicaltrials.gov/ct2/show/NCT02648477.

29. A(B)VD followed by Nivolumab as frontline therapy for higher risk patients with classical Hodgkin lymphoma. 2017; https://clinicaltrials.gov/ct2/show/NCT03033914.

30. Study of Pembrolizumab (MK-3475) plus chemotherapy vs placebo plus chemotherapy as neoadjuvant therapy and pembrolizumab vs placebo as adjuvant therapy in participants with triple negative breast cancer (TNBC) (MK-3475-522/KEYNOTE-522). 2017; https://clinicaltrials.gov/ct2/show/NCT03036488.

31. Arola OJ, Saraste A, Pulkki K, Kallajoki M, Parvinen M, Voipio-Pulkki LM. Acute doxorubicin cardiotoxicity involves cardiomyocyte apoptosis. *Cancer Res.* Apr 01 2000;60(7):1789-1792.

32. Spain L, Diem S, Larkin J. Management of toxicities of immune checkpoint inhibitors. *Cancer Treat Rev.* Mar 2016;44:51-60.

33. Sistigu A, Yamazaki T, Vacchelli E, et al. Cancer cell-autonomous contribution of type I interferon signaling to the efficacy of chemotherapy. *Nat Med.* Nov 2014;20(11):1301-1309.

34. MacKay JA, Chen M, McDaniel JR, Liu W, Simnick AJ, Chilkoti A. Self-assembling chimeric polypeptide-doxorubicin conjugate nanoparticles that abolish tumours after a single injection. *Nat Mater.* Dec 2009;8(12):993-999.

35. Ogawara K, Un K, Tanaka K, Higaki K, Kimura T. In vivo anti-tumor effect of PEG liposomal doxorubicin (DOX) in DOX-resistant tumor-bearing mice: Involvement of cytotoxic effect on vascular endothelial cells. *J Control Release.* Jan 05 2009;133(1):4-10.

36. Etrych T, Subr V, Strohalm J, Sirova M, Rihova B, Ulbrich K. HPMA copolymer-doxorubicin conjugates: The effects of molecular weight and architecture on biodistribution and in vivo activity. *J Control Release.* Dec 28 2012;164(3):346-354.

37. Maksimenko A, Dosio F, Mougin J, et al. A unique squalenoylated and nonpegylated doxorubicin nanomedicine with systemic long-circulating properties and anticancer activity. *Proc Natl Acad Sci. U. S. A.* Jan 14 2014;111(2):E217-226.

38. Ye DX, Ma YY, Zhao W, et al. ZnO-Based Nanoplatforms for Labeling and Treatment of Mouse Tumors without Detectable Toxic Side Effects. *ACS Nano.* Apr 26 2016;10(4):4294-4300.

39. Kingwell BA, Chapman MJ, Kontush A, Miller NE. HDL-targeted therapies: progress, failures and future. *Nat Rev Drug Discov.* Jun 2014;13(6):445-464.

40. Li D, Gordon S, Schwendeman A, Remaley A. Apolipoprotein mimetic peptides for stimulating cholesterol efflux. In: Anantharamaiah GM, Goldberg D, eds. *Apolipoprotein mimetics in management of human disease.* 2015:29-42.

41. Kuai R, Li D, Chen YE, Moon JJ, Schwendeman A. High-Density Lipoproteins: Nature's Multifunctional Nanoparticles. *ACS nano.* Mar 22 2016;10(3):3015-3041.

42. Schumacher TN, Schreiber RD. Neoantigens in cancer immunotherapy. *Science.* Apr 3 2015;348(6230):69-74.

43. Van Rooij N, Van Buuren MM, Philips D, et al. Tumor exome analysis reveals neoantigen-specific T-cell reactivity in an ipilimumab-responsive melanoma. *J Clin Oncol.* Nov 10 2013;31(32):e439-442.

44. Rizvi NA, Hellmann MD, Snyder A, et al. Cancer immunology. Mutational landscape determines sensitivity to PD-1 blockade in non-small cell lung cancer. *Science.* Apr 03 2015;348(6230):124-128.

45. Le DT, Durham JN, Smith KN, et al. Mismatch-repair deficiency predicts response of solid tumors to PD-1 blockade. *Science.* Jun 08 2017.

46. Schwendeman A, Sviridov DO, Yuan W, et al. The effect of phospholipid composition of reconstituted HDL on its cholesterol efflux and anti-inflammatory properties. *J Lipid Res.* Sep 2015;56(9):1727-1737.

47. Yuan Y, Wen J, Tang J, et al. Synthetic high-density lipoproteins for delivery of 10-hydroxycamptothecin. *Int J Nanomedicine.* 2016;11:6229-6238.

48. Tang J, Kuai R, Yuan W, Drake L, Moon JJ, Schwendeman A. Effect of size and pegylation of liposomes and peptide-based synthetic lipoproteins on tumor targeting. *Nanomedicine.* Apr 18 2017.

49. Cui L, Lin Q, Jin CS, et al. A PEGylation-Free Biomimetic Porphyrin Nanoplatform for Personalized Cancer Theranostics. *ACS Nano.* 2015;9(4):4484-4495.

50. Kreiter S, Vormehr M, van de Roemer N, et al. Mutant MHC class II epitopes drive therapeutic immune responses to cancer. *Nature.* Apr 30 2015;520(7549):692-U269.

51. Subramanian C, Kuai R, Zhu Q, et al. Synthetic high-density lipoprotein nanoparticles: A novel therapeutic strategy for adrenocortical carcinomas. *Surgery.* Jan 2016;159(1):284-294.

52. Rensen PC, de Vrueh RL, Kuiper J, Bijsterbosch MK, Biessen EA, van Berkel TJ. Recombinant lipoproteins: lipoprotein-like lipid particles for drug targeting. *Adv Drug Del Rev.* Apr 25 2001;47(2-3):251-276.

53. Ma Y, Adjemian S, Mattarollo SR, et al. Anticancer chemotherapy-induced intratumoral recruitment and differentiation of antigen-presenting cells. *Immunity.* Apr 18 2013;38(4):729-741.

54. Zou W, Wolchok JD, Chen L. PD-L1 (B7-H1) and PD-1 pathway blockade for cancer therapy: Mechanisms, response biomarkers, and combinations. *Sci Transl Med.* Mar 2 2016;8(328):328rv324.

55. Gubin MM, Zhang X, Schuster H, et al. Checkpoint blockade cancer immunotherapy targets tumour-specific mutant antigens. *Nature.* Nov 27 2014;515(7528):577-581.

56. Yadav M, Jhunjhunwala S, Phung QT, et al. Predicting immunogenic tumour mutations by combining mass spectrometry and exome sequencing. *Nature.* Nov 27 2014;515(7528):572-576.

57. Kingwell BA, Chapman MJ, Kontush A, Miller NE. HDL-targeted therapies: progress, failures and future. *Nat Rev Drug Discov.* Jun 2014;13(6):445-464.

58. Barter PJ, Nicholls S, Rye KA, Anantharamaiah GM, Navab M, Fogelman AM. Antiinflammatory properties of HDL. *Circ Res.* Oct 15 2004;95(8):764-772.

59. Cooney MT, Dudina A, De Bacquer D, et al. HDL cholesterol protects against cardiovascular disease in both genders, at all ages and at all levels of risk. *Atherosclerosis.* Oct 2009;206(2):611-616.

60. Frias MA, Lang U, Gerber-Wicht C, James RW. Native and reconstituted HDL protect cardiomyocytes from doxorubicin-induced apoptosis. *Cardiovasc Res.* Jan 01 2010;85(1):118-126.

61. Lorusso D, Di Stefano A, Carone V, Fagotti A, Pisconti S, Scambia G. Pegylated liposomal doxorubicin-related palmar-plantar erythrodysesthesia ('hand-foot' syndrome). *Ann Oncol.* Jul 2007;18(7):1159-1164.

62. Ishida T, Ichihara M, Wang X, et al. Injection of PEGylated liposomes in rats elicits PEG-specific IgM, which is responsible for rapid elimination of a second dose of PEGylated liposomes. *J Control Release.* May 01 2006;112(1):15-25.

Chapter 5 Conclusion

5.1 Significance

Recent innovations in tumor exome sequencing have signaled the new era of personalized cancer immunotherapy with patient-specific neo-antigens. However, a general methodology of inducing strong T cell responses against these neoantigens is still lacking.

To educate the immune system to mount strong neoantigen-specific T cell responses, the neoantigens need to be efficiently delivered in lymphoid organs such as lymph nodes, where high concentrations of dendritic cells are available to present the neoantigens in the context of MHC class I or MHC class II that can be recognized by CD8+ T or CD4+ T cells bearing the complementary T cell receptors (TCR).[1] In addition, adjuvants also need to be internalized by dendritic cells in order to upregulate activation markers and induce secretion of cytokines required for T cell activation. Traditional soluble vaccines are composed of soluble antigen peptides and adjuvants. Due to the small size of antigens, they can be quickly absorbed into systemic circulation or bind to non-dendritic cells. The amount of antigens that can be delivered into dendritic cells is very small.[2] Similarly, the lymph nodes draining of soluble adjuvant can be also very poor and the adjuvant is not always codelivered in dendritic cells, so the overall T cell responses are very weak. Although water-in-oil emulsions have been used to improve the T cell responses, recent studies showed depot formation and persistent antigen release at the injection site can impair antigen-specific T cell responses through induction of IFN-γ-mediated and Fas ligand-dependent apoptosis. [3]

To efficiently enhance the lymph nodes draining and delivery of antigens and adjuvants into dendritic cells, our strategy is to use synthetic high density lipoprotein (sHDL) based nanodiscs. sHDL is composed of phospholipids and ApoA-1 mimetic peptides, which wrap around the phospholipid bilayer to form the nanodisc structure that is about 10 nm in diameter. Previously sHDL has been tested in Phase I and II clinical trials for the treatment of cardiovascular diseases.[4] The well-established cGMP manufacturing protocols, good biocompatibility and safety profiles of sHDL nanodiscs make them very attractive as delivery vehicles. In this study, we customized different tumor antigen peptides and then anchored them to lipid bilayer of nanodiscs by adding phospholipid tails to these peptides. In addition, a TLR9 agonist CpG was modified with cholestesrol, which has high binding affinity to sHDL and enables the efficient loading of CpG in nanodiscs.[5] We demonstrated that sHDL nanodiscs coupled with antigens and adjuvants can dramatically improve the lymph nodes draining and enhance antigen presentation on dendritic cells compared with free antigens and adjuvants. Strikingly, nanodiscs elicited up to 47-fold greater frequencies of neoantigen-specific CTLs than soluble vaccines and even 31-fold greater than perhaps the strongest adjuvant in clinical trials (i.e. CpG in Montanide). Moreover, multi-epitope vaccination generated broad-spectrum T-cell responses that potently inhibited tumor growth. Nanodiscs eliminated established MC-38 and B16F10 tumors when combined with anti-PD-1 and anti-CTLA-4 therapy. Such vaccine nanodiscs also showed potent therapeutic efficacy for the treatment of various mucosal tumors, including lung tumors, oral tumors and intravaginal tumors. These findings may suggest a general strategy for personalized nanomedicine and represent a powerful approach for cancer immunotherapy.

In addition to the use of nanodisc-based peptide vaccine for elicitation of antitumor immune responses, we also sought to develop alternative approaches. For example, we demonstrated that

by simply incorporating a hydrophobic anticancer drug withalongolide A-4,19,27-triacetate (WGA-TA) in sHDL nanodiscs, we could enhance the therapeutic outcome of WGA-TA and reduce the side effects due to the improved tumor targeted delivery of nanodiscs.[6] In addition, some chemotherapeutic drugs have been reported to not only kill tumor cells directly, but also induce antitumor T cell responses, prompting a number of clinical trials on combination chemoimmunotherapy.[7] However, it remains unclear how to achieve potent immune activation with traditional chemotherapeutics in a manner that is safe, effective, and compatible with immunotherapy. Here we show that high-density lipoprotein (HDL)-mimicking nanodiscs loaded with doxorubicin (DOX), a widely used chemotherapeutic agent, can potentiate immune checkpoint blockade in murine tumor models. Delivery of DOX via nanodiscs triggered immunogenic cell death of cancer cells and exerted antitumor efficacy without any overt off-target side effects. Importantly, "priming" tumors with DOX-carrying nanodiscs elicited robust antitumor CD8+ T cell responses while broadening their epitope recognition to tumor-associated antigens, neoantigens, as well as intact whole tumor cells. Combination chemoimmunotherapy with nanodiscs plus anti-PD-1 therapy induced complete regression of established CT26 and MC38 colon carcinoma tumors in 80-88% of animals and protected survivors against tumor recurrence. Our work provides a new, generalizable framework for utilizing nanoparticle-based chemotherapy to initiate antitumor immunity and sensitize tumors to immune checkpoint blockade.

5.2 Future Directions

As one of the crucial component of nanodisc-based peptide vaccines, adjuvants are critical for providing signals needed for T cell activation. In our study, we use CpG, which is a TLR9 agonist as the adjuvant. Although we saw promising results on mice, it remains to be seen how

well this adjuvant can work in humans, because the expression patterns of TLR9 receptors in mice and humans are different.[8] In the future, different adjuvants can be tested in parallel and those that are more suitable for human use can be included in the vaccine nanodisc platform in order to facilitate the clinical translation.

In addition, our synthetic high density lipoprotein (sHDL) nanodisc platform mimics the structure and function of endogenous HDL in vivo, so that they share many properties such as ultrasmall sizes and long circulation time in vivo. However, it should be noted that sHDL still has a shorter circulation time than endogenous HDL. Further research is needed to further optimize the structural peptide of sHDL in terms of the lengths and sequences, so that the sHDL has even longer circulation time in vivo, which can be useful for systemic delivery of therapeutic molecules.

5.3 References

1. Drake CG, Lipson EJ, Brahmer JR. Breathing new life into immunotherapy: review of melanoma, lung and kidney cancer. *Nat Rev Clin Oncol.* Jan 2014;11(1):24-37.

2. Melief CJM, van der Burg SH. Immunotherapy of established (pre) malignant disease by synthetic long peptide vaccines. *Nat Rev Cancer.* May 2008;8(5):351-360.

3. Hailemichael Y, Dai ZM, Jaffarzad N, et al. Persistent antigen at vaccination sites induces tumor-specific CD8(+) T cell sequestration, dysfunction and deletion. *Nat Med.* Apr 2013;19(4):465-472.

4. Kuai R, Li D, Chen YE, Moon JJ, Schwendeman A. High-Density Lipoproteins: Nature's Multifunctional Nanoparticles. *ACS nano.* Mar 22 2016;10(3):3015-3041.

5. Kuai R, Ochyl LJ, Bahjat KS, Schwendeman A, Moon JJ. Designer vaccine nanodiscs for personalized cancer immunotherapy. *Nat Mater.* Apr 2017;16(4):489-496.

6. Kuai R, Subramanian C, White PT, et al. Synthetic high-density lipoprotein nanodisks for targeted withalongolide delivery to adrenocortical carcinoma. *Int J Nanomed.* 2017;12:6581-6594.

7. Krysko DV, Garg AD, Kaczmarek A, Krysko O, Agostinis P, Vandenabeele P. Immunogenic cell death and DAMPs in cancer therapy. *Nat Rev Cancer.* Dec 2012;12(12):860-875.

8. Klinman DM. Immunotherapeutic uses of CpG oligodeoxynucleotides. *Nat Rev Immunol.* Apr 2004;4(4):248-257.